Simulating quantum matter through lattice field theories

by

Lauren Elizabeth Hayward Sierens

A thesis
presented to the University of Waterloo
in fulfillment of the
thesis requirement for the degree of
Doctor of Philosophy
in
Physics

Waterloo, Ontario, Canada, 2017

Examination Committee Members

The following members served on the examination committee for this thesis. The decision of the examination committee is by majority vote.

Role	**Name**	**Title**
Supervisor	Roger Melko	Associate Professor, Department of Physics & Astronomy, University of Waterloo Associate Faculty, Perimeter Institute for Theoretical Physics
Committee member	David Hawthorn	Associate Professor, Department of Physics & Astronomy, University of Waterloo
Internal examiner	Robert Myers	Adjunct Professor, Department of Physics & Astronomy, University of Waterloo Faculty Chair, Perimeter Institute for Theoretical Physics
Internal-external examiner	Pierre-Nicholas Roy	Professor, Department of Chemistry, University of Waterloo
External examiner	Sylvain Capponi	Professeur, Laboratoire de Physique Théorique, Institut de Recherche sur les Systèmes Atomiques et Moléculaires Complexes, Université de Toulouse, Centre National de la Recherche Scientifique

Declaration

Abstract

Quantum many-body systems are comprised of complex networks of microscopic interactions that work together to produce novel collective phases and phenomena. For strongly-interacting systems, the connection between the underlying atomic-scale behaviour and the resulting emergent observable phenomena is exponentially (and, in practice, infinitely) complicated such that it becomes impossible to fully understand the connection between the physics at the microscopic and macroscopic levels. The most promising theoretical approaches to addressing this infinite complexity utilize microscopic coarse-graining along with powerful computational simulations and strategies. In this thesis, we apply numerical methods to effective lattice models and field theories with the goal of shedding light onto universal critical behaviour and exotic low-temperature phases in condensed matter physics.

We start by exploring universal features of critical non-interacting systems, for which several analytical strategies are readily available for calculating certain observables. We study the behaviour of the system's entanglement for various entangling geometries, and utilize numerical techniques in order to isolate new universal features of Gaussian fixed points, which provide insight into the underlying critical theory's renormalization group flow. We then proceed to examine computational strategies and, in particular, Monte Carlo simulations for studying more general interacting models. We focus on the application of such strategies to the field of high-temperature superconductivity, for which we develop a coarse-grained model, simulate macroscopic observables and compare our results with those of recent experiments. We conclude that lattice field theories together with innovative computational methods offer new perspectives on both universality and emergent phenomena in quantum matter.

Acknowledgements

I feel so fortunate to have been able to pursue a PhD in Physics, and I will now take the opportunity to express my sentimental side and to acknowledge the long list of people who made this journey both possible and enjoyable.

I would like to start by thanking my advisor, Roger Melko. Roger, I am confident that I will never be able to fully express my gratitude for all of the help, advice and guidance that you have given to me over the past four and a half years, but I will make an attempt to do so here. Thank you for treating me as a colleague from the first time that you met me as opposed to the inexpert graduate student that I truly was. Thank you for respecting my ideas, for taking my concerns seriously and for finding time to patiently answer my questions no matter how busy you were. Thank you for trusting and supporting my work and for finding me exciting research projects and collaboration opportunities. Without such a positive graduate school experience, I would not be so confident in my decision to pursue a more teaching-focussed career.

I was fortunate to study as a resident graduate student at both the University of Waterloo and the Perimeter Institute for Theoretical Physics, and as a visiting graduate student at the Kavli Institute for Theoretical Physics at the University of California, Santa Barbara. Thank you to the staff and faculty of these institutions for providing welcoming, collaborative research environments and for supplying me with endless amounts of tea. Thank you to the administrative staff, in particular Anja Drygala, Debbie Guenther and Judy McDonnell, for being the glue that holds these institutions together. Thank you to SHARCNET for access to several decades of high-performance computing resources, which were used for all of my research projects. Thank you to the Perimeter Institute for allowing me to participate in many scientific outreach events, and especially for the opportunity to meet Justin Trudeau!

Throughout my graduate studies, I learned from and collaborated on projects with many brilliant physicists, including faculty members and postdoctoral fellows both within and outside of Waterloo. Many of these physicists also served as members of my advisory committee, my qualification examination committee and/or my thesis examination committee. To this end, I thank Agata Branczyk, Pablo Bueno, Anton Burkov, Sylvain Capponi, Anushya Chandran, Denis Dalidovich, Michel Gingras, David Hawthorn, Chris Herdman, Steven Kivelson, Max Metlitski, Robert Myers, Pierre-Nicholas Roy, Subir Sachdev, Rajiv Singh, Guifre Vidal, Xiao-Gang Wen and William Witczak-Krempa.

My fellow graduate students and friends have made my research more successful and my life much more fun. Thank you to Andrew Achkar, Leilee Chojnacki, Caleb Cook, Johannes Helmes, Étienne Lantagne-Hurtubise, Laimei Nie and Tiffany Vlaar for your collaboration on research projects. Thank you to Andrzej Banburski, Matt Beach, Grigory Bednik, Alexandre Day, Jim Garrison, Markus Hauru, Qi Hu, Behnam Javanparast, David Pomaranski, Trevor Rempel, Sharmistha Sahoo, Giacomo Torlai, Dan Wohns and Gang Xu for insightful discussions and fun adventures. Thank you to Stephen Inglis for spending many hours teaching me about Monte Carlo simulations and for answering my many research questions at the start of my PhD. Thank you to Ann Kallin for being my travel buddy to conferences and summer schools during the first two years of my PhD and for introducing me to many other graduate students and researchers who have now become my friends and collaborators. Thank you to Pedro Ponte for encouraging me to uphold the highest academic and dietary standards, and for introducing me to creative new English slang. Thank you to Linqing Chen, my first friend in Waterloo, for offering me constant encouragement and for always seeing me as the better person that I strive to be. Thank you to Nosiphiwo Zwane for heart-to-heart conversations about work, life, family, politics and television shows, and for teaching me to speak Swahili (or at least to understand some of the lyrics to The Lion King songs). Thank you to Bohdan Kulchytskyy, who is one of my closest research collaborators and also one of my closest friends, for scrutinizing my work and criticizing it when necessary (I didn't always like it, but I needed it), for encouraging me to take more risks, and for betting against me in games of pool so that I could make some extra money. Thank you to Paulina Corona Ugalde, my closest confidant, for listening to my rants, frustrations and insecurities without judgement, for motivating me to fight for what is right instead of settling for what is easy, and for exploring Ontario with me; your friendship has changed my life for the better.

Being away from my parents, siblings, nieces and nephews in Manitoba has been one of the greatest challenges of completing my graduate studies, and I want to thank all of my family for their love and encouragement from afar. In particular, thank you to my mom, Cindy Hayward, for being a strong, successful and modest woman of science and for raising me to believe that women can do any job that men can do. Thank you to my dad, John Hayward, for being my biggest fan; although my confidence in myself has wavered many times, I know that yours in me never has. Thank you to my little brother, Timothy Hayward, for viewing me as a role model and for being one of mine. Thank you to my uncle, Peter Williams, for sparking my interest in physics. Thank you to my new family-in-law, Chris and Brigitte Sierens; Scott, Liane, Tyson, Tessa, Sarah and Cole Sierens; Brittany and Justin Perreaux; and Joshua Sierens; spending time with all of you in Somerset has been one of the best ways to relax and relieve the stresses of graduate school.

Finally, thank you to my husband and best friend, Todd Sierens, without whom I believe that I would not have been able to complete my PhD. Thank you for your constant love, patience and encouragement, and for your endless supply of random facts. Thank you for supporting and prioritizing my dreams and for keeping me sane by putting my worries into perspective. Thank you for understanding me to my core and for challenging me to become the best possible version of myself.

Dedication

For Todd and for our family, both present and future.

Table of Contents

List of Figures

List of Algorithms

List of Tables

Chapter 1

Introduction

Observable macroscopic behaviours of many low-energy quantum systems are governed by the interactions and dynamics of underlying microscopic degrees of freedom that live on a crystal lattice. One of the fundamental challenges within the field of condensed matter physics is to understand how interactions at the lattice length scale are connected to a material's thermodynamic properties and emergent phases. Within strongly-interacting quantum systems, the physics at these microscopic scales leads to large collections of coupled, analytically-unsolvable equations such that computational methods and numerical approximation schemes become essential tools for advancing studies of quantum many-body systems.

Advancements in computer technology and algorithms have been instrumental in pushing the boundaries of research within condensed matter and materials physics for decades. In the 1940s, Monte Carlo simulations performed on one of the first electronic vacuum tube computers played a pivotal role in developing an understanding of neutron diffusion in materials. Transistors subsequently began to replace vacuum tubes in computers, and since then the power of computational technology has increased exponentially with time. The need for more efficient computational methods within condensed matter physics became apparent in the 1980s when the experimental discovery of materials such as high-temperature superconductors began to reveal exotic emergent phenomena that result from strong correlations. Since effective non-interacting models and perturbative techniques cannot describe such phenomena within strongly-interacting systems, the past few decades have seen a rapid growth in research within the field of computational condensed matter physics, resulting in algorithmic developments such as quantum Monte Carlo methods, the density matrix renormalization group, tensor networks and machine learning. Modern investigations into complex phenomena such as quantum entanglement and universality have demonstrated that the advantages and applications of numerical methods are not limited to interacting systems. As we will see, within both non-interacting and interacting models, computational methods and technologies have unveiled otherwise-unattainable insights into emergent behaviour within quantum matter.

In order to appreciate the value of advanced computational techniques within condensed matter physics, let us first consider the limits of more naive brute-force approaches to extracting thermodynamic observables. A general system's microscopic features are encoded within a model that is characterized by a Hamiltonian H. After defining H, all information needed to calculate macroscopic observables is then contained within the partition function

$$\mathcal{Z} = \mathrm{Tr}\left[e^{-H/T}\right], \tag{1.1}$$

where T is the temperature and we have elected to employ units where the Boltzmann constant is equal to one. The trace in this equation is over all underlying degrees of freedom that parametrize the Hamiltonian. For most practical models H, performing this trace (either analytically or numerically) is an exponentially difficult and, in practice, impossible task. Analytical techniques for calculating $\mathcal{Z}$ only exist for special simplified models, and calculating $\mathcal{Z}$ exactly through numerical techniques involves summing over the elements of an exponentially large Hilbert space. Such numerical schemes thus limit calculations to systems with less than one hundred constituent particles, while physical materials comprise on the order of 10^{23} interacting particles. As a result, more sophisticated computational methods are necessary in order to extract predictions for macroscopic observables in the thermodynamic limit.

We will see that many phases of classical and quantum matter are well-described by a classical $O(N)$ model (also known as a nonlinear sigma model), in which the microscopic variables $\mathbf{n}_i$ are N-dimensional unit vectors with components $n_{i\alpha}$ (for $\alpha = 1, 2, \ldots, N$). Interactions between neighbouring degrees of freedom are described by the Hamiltonian

$$H_{O(N)} = -J \sum_{\langle ij \rangle} \mathbf{n}_i \cdot \mathbf{n}_j, \tag{1.2}$$

where J is an interaction energy and the notation $\langle ij \rangle$ indicates that the corresponding sum is over all nearest-neighbouring pairs of sites on the lattice. We note that the name for this model is based upon the Hamiltonian's invariance under global $O(N)$ rotations of the variables $\mathbf{n}_i$. The $O(N)$ model goes by several other names for certain values of N. For example, the $O(1)$ model is referred to as the Ising model, the $O(2)$ case is known as the XY model, and the $O(3)$ model is called the Heisenberg model. The partition function corresponding to this model can be expressed as

$$\mathcal{Z}_{O(N)} = \prod_i \int \mathcal{D}\mathbf{n}_i \; \delta\big(\mathbf{n}_i^2 - 1\big)\, e^{-H_{O(N)}/T}, \tag{1.3}$$

where $\prod_i \int \mathcal{D}\mathbf{n}_i$ is a functional integral and the Dirac delta function is used to enforce that $\mathbf{n}_i$ has unit magnitude on every lattice site i.

This thesis utilizes numerical methods in order to extract universal quantities and thermodynamic observables from models that are closely related to the $O(N)$ model of Equations (1.2) and (1.3). The remainder of this chapter focusses on deriving other classical and quantum lattice field theories related to the $O(N)$ model and discusses techniques for studying phase transitions and critical behaviour on general finite size systems.

Chapter 2 examines the simplest, non-interacting limit of such field theories, for which one can take advantage of several analytical and numerical simplifications in order to quantify observables and correlations within the system. Although many features of such non-interacting systems are already well-established, we find that a wealth of previously unexplored universal features exist at criticality.

In Chapter 3, we discuss Monte Carlo methods for studying $O(N)$ models as well as other closely related interacting models with specific broken symmetries. We see that such methods are capable of extracting thermodynamic observables as well as quantities that characterize the system's critical behaviour.

Chapter 4 examines applications of $O(N)$-like models to the field of high-temperature superconductivity and its so-called pseudogap regime. We find that certain classes of such models yield observable quantities that agree well with recent experimental measurements for a wide range of temperatures. This agreement validates the fundamental symmetry constraints that define the Hamiltonian model, and such constraints can provide deep insight into the underlying physical mechanisms that lead to the unique macroscopic features observed in the superconducting and pseudogap regimes.

We summarize our findings in Chapter 5 and discuss open questions and unexplored applications of $O(N)$-like lattice models and their corresponding field theories.

1.1 Lattice field theories

In the vicinity of a critical point, it can be useful to study new coarse-grained theories that average over constraints and structures at the (microscopic) lattice length scale [1, 2, 3]. For the $O(N)$ field theory of Equations (1.2) and (1.3), for example, the degrees of freedom $\mathbf{n}_i$ are constrained to only angular fluctuations, but one can also consider related coarse-grained fields $\boldsymbol{\phi}(\mathbf{x})$ that do not impose such hard constraints. One can imagine that the fields $\boldsymbol{\phi}(\mathbf{x})$ within such theories are defined in terms of the underlying degrees of freedom $n_{i\alpha}$ such that [3]

$$\phi_\alpha(\mathbf{x}) \sim \sum_{i \in \mathcal{N}(x)} n_{i\alpha}, \tag{1.4}$$

where $\mathcal{N}(x)$ is some spatial neighbourhood of the coordinate $\mathbf{x}$. We note that such fields are defined continuously such that $\mathbf{x}$ is not restricted to the lattice sites i. However, in the chapters that follow, we elect to consider values of the field ϕ_α restricted to another lattice (which is, in general, different from the original lattice for the variables $n_{i\alpha}$) in order to take advantage of certain numerical methods. The fields $\boldsymbol{\phi}(\mathbf{x})$ introduced through the coarse-graining procedure of Equation (1.4) are no longer constrained to have unit magnitude, but the field theory must incorporate some kind of an effective potential such that it is not energetically favourable for the magnitude of $\boldsymbol{\phi}(\mathbf{x})$ to be large so as to respect the underlying microscopic constraints [1, 3].

1.1.1 Classical field theories

Through Hubbard-Stratonovich transformation, one can show that a near-critical $O(N)$ model can be described in terms of a classical action $S_\mathrm{c}[\boldsymbol{\phi}]$ that includes an expansion in powers of ϕ_α^2 up to order $(\phi_\alpha^2)^2$ such that

$$\mathcal{Z}_\mathrm{c} = \int \mathcal{D}\boldsymbol{\phi}(\mathbf{x})\, e^{-S_\mathrm{c}[\boldsymbol{\phi}]}, \tag{1.5}$$

with

$$S_\mathrm{c}[\boldsymbol{\phi}] = \int \mathrm{d}^d\mathbf{x} \left\{ \frac{1}{2} \sum_\alpha \left[(\nabla \phi_\alpha)^2 + r\phi_\alpha^2 \right] + \frac{u}{4!} \left(\sum_\alpha \phi_\alpha^2 \right)^2 \right\}, \tag{1.6}$$

where r and u are couplings that incorporate the microscopic degrees of freedom. When $u > 0$, this field theory describes a phase transition from a low-temperature phase with

$\langle \phi_\alpha \rangle \neq 0$ to a high-temperature, disordered phase with $\langle \phi_\alpha \rangle = 0$. For the classical $O(N)$ model, the coupling r is proportional to $T - T_c$ in the original Hamiltonian, such that $r = 0$ at the critical point [3].

If we now consider this theory at a discrete set of sites $\{\mathbf{x}\}$ and on a lattice with spacing a, we arrive at a classical lattice field theory given by

$$S_{\mathrm{c}}[\boldsymbol{\phi}] = \frac{a^{d-2}}{2} \sum_{\langle \mathbf{x}\mathbf{x}' \rangle} \sum_{\alpha} \left(\phi_{\mathbf{x},\alpha} - \phi_{\mathbf{x}',\alpha}\right)^2 + a^d \sum_{\mathbf{x}} \left[\frac{r}{2} \sum_{\alpha} \phi_{\mathbf{x},\alpha}^2 + \frac{u}{4!} \left(\sum_{\alpha} \phi_{\mathbf{x},\alpha}^2 \right)^2 \right], \tag{1.7}$$

where the gradient terms in the continuum theory have been approximated by simple finite differences.

1.1.2 Quantum field theories

The classical $O(N)$ model of Equation (1.2) (with $N \geq 2$) can be mapped to a quantum rotor (QR) model, for which the Hamiltonian is given by [3]

$$H_{\mathrm{QR}} = -J \left[\sum_{\langle ij \rangle} \hat{\mathbf{n}}_i \cdot \hat{\mathbf{n}}_j - \frac{g}{2} \sum_i \hat{\mathbf{L}}_i^2 \right], \tag{1.8}$$

where $\hat{\mathbf{L}}_i$ represents the angular momentum on site i. $\hat{\mathbf{n}}_i$ and $\hat{\mathbf{L}}_i$ are both quantum mechanical operators, and $\hat{\mathbf{n}}_i$ is still constrained such that $\hat{\mathbf{n}}_i^2 = 1$. Specifically, through Suzuki-Trotter expansion, one can express the quantum partition function $\mathcal{Z}_{\mathrm{q}}$ corresponding to the quantum rotor model of Equation (1.8) as [3]

$$\begin{aligned} \mathcal{Z}_{\mathrm{q}} &= \mathrm{Tr}\left[e^{-H_{\mathrm{QR}}/T}\right] \\ &= \int \mathcal{D}\mathbf{n}(\mathbf{x},\tau)\, \delta\big(\mathbf{n}^2(\mathbf{x},\tau) - 1\big)\, e^{-S_{\mathrm{q}}[\mathbf{n}]}, \end{aligned} \tag{1.9}$$

with

$$S_{\mathrm{q}}[\mathbf{n}] \sim \int \mathrm{d}^d\mathbf{x} \int_0^{1/T} \mathrm{d}\tau \sum_{\alpha} \Big[\left(\partial_\tau n_\alpha\right)^2 + \left(\nabla n_\alpha\right)^2 \Big], \tag{1.10}$$

which resembles a continuum version of the classical $O(N)$ model of Equation (1.2), but with interactions along the d spatial dimensions as well as along an additional dimension

τ (which is an imaginary time). For this reason, we say that a quantum rotor model in d spatial dimensions can be mapped to a classical $O(N)$ model in $d+1$ dimensions. Following a similar coarse-graining procedure to the one used to arrive at the classical field theory of Equation (1.6), one can express this model as [3]

$$\mathcal{Z}_{\mathrm{q}} = \int \mathcal{D}\boldsymbol{\phi}(\mathbf{x},\tau)\, e^{-S_{\mathrm{q}}[\boldsymbol{\phi}]}, \tag{1.11}$$

with

$$S_{\mathrm{q}}[\boldsymbol{\phi}] = \int \mathrm{d}^d\mathbf{x} \int_0^{1/T} \mathrm{d}\tau \left\{ \frac{1}{2} \sum_\alpha \left[(\partial_\tau \phi_\alpha)^2 + (\nabla \phi_\alpha)^2 + r\phi_\alpha^2 \right] + \frac{u}{4!} \left(\sum_\alpha \phi_\alpha^2 \right)^2 \right\}, \tag{1.12}$$

which corresponds to the quantum Hamiltonian

$$H_{\mathrm{q}} = \int \mathrm{d}^d\mathbf{x} \left\{ \frac{1}{2} \sum_\alpha \left[\pi_\alpha^2 + (\nabla \phi_\alpha)^2 + r\phi_\alpha^2 \right] + \frac{u}{4!} \left(\sum_\alpha \phi_\alpha^2 \right)^2 \right\}, \tag{1.13}$$

where π_α is the canonical momentum conjugate to ϕ_α such that

$$\begin{gathered} [\phi_\alpha(\mathbf{x}), \phi_\beta(\mathbf{x}')] = [\pi_\alpha(\mathbf{x}), \pi_\beta(\mathbf{x}')] = 0, \\ [\phi_\alpha(\mathbf{x}), \pi_\beta(\mathbf{x}')] = i\delta_{\alpha\beta}\, \delta^d(\mathbf{x} - \mathbf{x}'). \end{gathered} \tag{1.14}$$

Considering this theory on a lattice with spacing a as in Equation (1.7) then gives a quantum lattice field theory described by

$$H_{\mathrm{q}} = \frac{a^{d-2}}{2} \sum_{\langle \mathbf{x}\mathbf{x}' \rangle} \sum_\alpha (\phi_{\mathbf{x},\alpha} - \phi_{\mathbf{x}',\alpha})^2 + a^d \sum_{\mathbf{x}} \left[\frac{1}{2} \sum_\alpha \left(\pi_{\mathbf{x},\alpha}^2 + r\phi_{\mathbf{x},\alpha}^2 \right) + \frac{u}{4!} \left(\sum_\alpha \phi_{\mathbf{x},\alpha}^2 \right)^2 \right], \tag{1.15}$$

where the commutation relations for the lattice fields are given by

$$\begin{gathered} [\phi_{\mathbf{x},\alpha}, \phi_{\mathbf{x}',\beta}] = [\pi_{\mathbf{x},\alpha}, \pi_{\mathbf{x}',\beta}] = 0, \\ [\phi_{\mathbf{x},\alpha}, \pi_{\mathbf{x}',\beta}] = i\delta_{\alpha\beta}\, \delta_{\mathbf{x}\mathbf{x}'}. \end{gathered} \tag{1.16}$$

1.2 Correlation functions

Correlation functions provide a useful way of measuring statistical correlations between degrees of freedom (such as $\mathbf{n}_i$ or $\boldsymbol{\phi}(\mathbf{x})$) at different spatial locations $\mathbf{x}$ and $\mathbf{x}'$. For translationally invariant systems in d spatial dimensions, two-point correlation functions $G(\mathbf{x}, \mathbf{x}')$ are expected to scale with distance such that [4, 5, 3]

$$G(\mathbf{x}, \mathbf{x}') = G(r) \sim \begin{cases} \dfrac{1}{r^{(d-1)/2}} e^{-r/\xi} & \text{(for } r \gg \xi\text{)} \\ \dfrac{1}{r^{d-2+\eta}} & \text{(for } \xi \to \infty\text{),} \end{cases} \tag{1.17}$$

where $r = |\mathbf{x} - \mathbf{x}'|$ is the separation between the lattices sites $\mathbf{x}$ and $\mathbf{x}'$ and ξ is called the *correlation length*, which measures the length scale over which fields on the lattice are correlated. The quantity η is called the anomalous dimension, and it is discussed in more detail in Section 1.3.

The case where the correlation length diverges ($\xi \to \infty$) corresponds to a critical point. In such critical theories, the two-point correlators are expected to decay according to a power law, in contrast to the exponential decay expected for non-critical systems. Note, however, that away from a critical point, an exponential scaling is only predicted for $r \gg \xi$. In practice, many non-critical gapped systems experience a power-law decay of correlation functions on smaller length scales before crossing over to an exponential decay for length scales beyond the correlation length. As a result, on finite lattices with length scale $L < \xi$, the correlations for systems away from the thermodynamic critical point may resemble those of critical systems. Finite size scaling procedures are required to locate the critical point in such situations, as discussed in Section 1.4.

1.3 Critical exponents

Within the vicinity of a second-order phase transition, the behaviour of several observable quantities can be parametrized in terms of the reduced temperature

$$t = \frac{T - T_c}{T_c}. \tag{1.18}$$

We study systems for which it is possible to define a local order parameter m. This order parameter is zero in the high-temperature, disordered phase ($T > T_c$). For $T < T_c$, the order depends on the distance to the critical point according to

$$m \sim (-t)^\beta \qquad (\text{for } T < T_c), \tag{1.19}$$

where β is referred to as the critical exponent for m.

One can quantify the strength of fluctuations in the order parameter by measuring the (zero-field) magnetic susceptibility per spin, χ. This quantity diverges at the critical point with a critical exponent γ such that

$$\begin{aligned} \chi &= \left.\frac{\partial m}{\partial B}\right|_{B=0} \\ &= \frac{N}{T}\left(\left\langle m^2\right\rangle - \left\langle m\right\rangle^2\right) \\ &\sim |t|^{-\gamma}. \end{aligned} \tag{1.20}$$

Similarly, the specific heat per spin, c, measures a system's energy fluctuations and diverges as $t \to 0$ according to a critical exponent α such that

$$\begin{aligned} c &= -\frac{T}{N}\frac{\partial^2 F}{\partial T^2} = \frac{1}{N}\frac{\partial \langle E\rangle}{\partial T} \\ &= \frac{\left\langle E^2\right\rangle - \left\langle E\right\rangle^2}{NT^2} \\ &\sim |t|^{-\alpha}, \end{aligned} \tag{1.21}$$

where $F = -T \log \mathcal{Z}$ is the free energy.

Recall from Section 1.2 that one can define the characteristic length scale of correlations within a system in terms of the correlation length ξ. Similarly to χ and c, this correlation length diverges when the system becomes critical such that

$$\xi \sim |t|^{-\nu}, \tag{1.22}$$

where ν is the critical exponent corresponding to ξ.

In the vicinity of the phase transition, all of the above observables $\mathcal{O}_x$ are expected to decay to zero or diverge with a characteristic form given by

$$\begin{aligned} \mathcal{O}_x &\sim |t|^x \\ &\sim \xi^{-x/\nu}, \end{aligned} \tag{1.23}$$

where x is the critical exponent x governing the behaviour of $\mathcal{O}_x$.

As seen in Section 1.2, there is another critical exponent known as the anomalous dimension η, which governs the power-law scaling of correlation functions exactly at the critical point such that

$$G(r, t = 0) \sim \frac{1}{r^{d-2+\eta}}. \tag{1.24}$$

The values of the critical exponents in general depend upon the the dimension of the system and upon the symmetries of the Hamiltonian and its order parameter. However, the critical exponents have been shown to satisfy several universal scaling relations for any field theory, such as [5]

$$\begin{gathered} \alpha + 2\beta + \gamma = 2, \\ \alpha = 2 - d\nu, \\ \gamma = \nu(2 - \eta). \end{gathered} \tag{1.25}$$

1.4 Finite size scaling

On a finite system with length scale L, correlations can never exceed L and one cannot directly measure the thermodynamic correlation length ξ if $L < \xi$. We then expect Equation (1.23), which governs the behaviour of $\mathcal{O}_x$ in the vicinity of a phase transition, to be modified for the case of observables $\mathcal{O}_{x,L}$ on finite lattices such that [5, 6]

$$\begin{aligned} \mathcal{O}_{x,L} &\sim \big[\min(L, \xi)\big]^{-x/\nu} \\ &\sim \begin{cases} \xi^{-x/\nu} & \text{(for } L \gg \xi) \\ L^{-x/\nu} & \text{(for } L \ll \xi). \end{cases} \end{aligned} \tag{1.26}$$

One can alternatively express this expected behaviour as [5, 6]

$$\mathcal{O}_{x,L} = \xi^{-x/\nu} \, f_x\!\left(\frac{L}{\xi}\right), \tag{1.27}$$

where the function $f_x(z)$ must obey

$$f_x(z) \sim \begin{cases} \text{constant} & \text{(for } z \gg 1) \\ z^{-x/\nu} & \text{(for } z \ll 1). \end{cases} \tag{1.28}$$

Since the thermodynamic correlation length ξ is usually not straightforwardly accessible on a finite lattice, it is useful to use Equation (1.22) to reexpress $\mathcal{O}_{x,L}$ in terms of L and $|t|$ as

$$\begin{aligned}\mathcal{O}_{x,L} &= L^{-x/\nu}\left(\frac{\xi}{L}\right)^{-x/\nu} f_x\left(\frac{L}{\xi}\right)\\ &= L^{-x/\nu}\left(L\,|t|^{\nu}\right)^{x/\nu} f_x(L\,|t|^{\nu})\\ &\equiv L^{-x/\nu}\widetilde{f}_x\big(L^{1/\nu}|t|\big)\,,\end{aligned}\tag{1.29}$$

where $\widetilde{f}_x(z) \equiv z^x f_x(z^\nu)$. We therefore expect that, in the vicinity of a phase transition, plots of $L^{x/\nu}\mathcal{O}_{x,L}$ versus $L^{1/\nu}|t|$ for various system sizes L should all collapse onto the same curve.

1.5 Entanglement scaling

Entanglement is a uniquely quantum feature whereby the states describing two regions of space are inextricably linked. The correlations corresponding to quantum entanglement can be used to accomplish classically impossible tasks within the realms of quantum communication and quantum computation.

For a general quantum system on a lattice, a given region of space A is entangled with its surroundings, with the length scale of these quantum correlations extending from the lattice length scale up to the system's correlation length ξ. At a critical point where $\xi \to \infty$, one thus expects to find entanglement at all length scales. At such a critical point, the behaviour of the ground-state entanglement between two complementary regions A and $\overline{A}$ of a physical system in general depends upon the size and geometrical features of the boundary ∂A that separates these regions [7, 8, 9]. An arbitrary choice for such a boundary in two spatial dimensions is illustrated in Fig. 1.1. We will see that, by introducing a means of quantifying entanglement for various boundaries ∂A and by exploiting the scale-invariance that characterizes criticality, one can extract various universal numbers that describe the underlying fixed point.

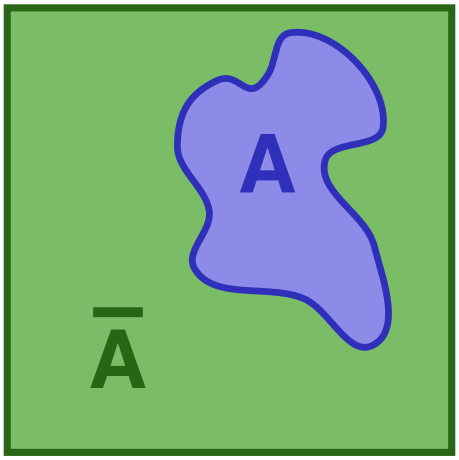

Figure 1.1: Possible division of a system into complementary regions A and $\overline{A}$ in two spatial dimensions. We consider methods for determining properties of the entanglement between A and $\overline{A}$ for the case where the system is critical.

1.5.1 Entanglement entropy

Entanglement in general multipartite thermal systems is difficult to quantify, but for bipartite entanglement in a ground state, one can utilize the entanglement entropy, which is defined in terms of the reduced density matrix $\rho_A = \mathrm{Tr}_{\overline{A}}\left(\rho_{A\overline{A}}\right)$ as

$$S_1(A) = -\,\mathrm{Tr}\left(\rho_A \log \rho_A\right). \tag{1.30}$$

In addition, for such systems one can study the more general Rényi entanglement entropies [10, 11], which are given by

$$S_\alpha(A) = \frac{1}{1-\alpha} \log\left(\mathrm{Tr}\, \rho_A^\alpha\right), \tag{1.31}$$

where α is called the Rényi index. Taking the limit $\alpha \to 1$ in Equation (1.31) recovers the (von Neumann) entanglement entropy of Equation (1.30). Since the overall density matrix $\rho_{A\overline{A}}$ is assumed to correspond to a pure ground state, we have $S_\alpha(A) = S_\alpha(\overline{A})$ for all possible bipartitions.

The entanglement entropies $S_\alpha(A)$ can exhibit interesting behaviour as the size and geometrical features of the boundary of region A are varied. In $d > 1$, both gapped and critical systems obey a dominant *area law*, whereby the entanglement entropies are proportional to the size of the boundary $|\partial A|$ [7, 8, 9]. The coefficient of such a term is non-universal, but, for certain boundary geometries, the entanglement entropy of a critical theory can include additional subleading corrections containing universal quantities. These universal quantities can give insight into the underlying theories that describe the fixed point of the critical theory's renormalization group (RG) flow.

In order to make predictions about the scaling of entanglement entropy in the vicinity of a critical point, we make two fundamental assumptions. First, we assume that the scale invariance associated with critical points means that one must sum contributions to S_α from all length scales r_n along the RG flow. We take r_n to be the renormalized microscopic length scale after n RG steps, such that r_n is given in terms of the lattice spacing a and the spatial RG scaling factor b as

$$r_n = b^n a. \tag{1.32}$$

Our second assumption is motivated by the aforementioned area law and asserts that the behaviour of the ground-state entanglement entropy S_α is dominated by contributions local to the boundary. The entanglement contributions resulting from these two assumptions are illustrated in Figure 1.2. Taken together, our assumptions imply that we expect to find an area law at every length scale.

As a result of our first assumption, the entanglement entropy $S_\alpha(A)$ is given as a sum over contributions $S_\alpha(A, r_n)$ from each length scale r_n as

$$S_\alpha(A) = \sum_n S_\alpha(A, r_n), \tag{1.33}$$

where n is a non-negative integer that labels the RG steps. Taking the limit where this sum can be converted to an integral and utilizing Equation (1.32) then gives

$$S_\alpha(A) = \int_{r_{\min}}^{r_{\max}} \mathrm{d}(\log r)\, S_\alpha(A, r), \tag{1.34}$$

where we have absorbed a factor of $\log b$ into the function $S_\alpha(A, r)$. The minimum contributing length scale $r_{\min} = r_{\mathrm{UV}} = a$ is the lattice spacing (the UV cutoff) and $r_{\max} = \min(L_A, \xi)$. Here, L_A is the characteristic length of the boundary and ξ is the correlation length, which diverges for critical theories such that we take $\xi \to \infty$ and thus $r_{\max} = L_A$. In addition, in the following examples we consider geometries where $L_A \propto L$ such that $r_{\max} \sim L$, where L is the size of the system (the IR regulator). We ignore for

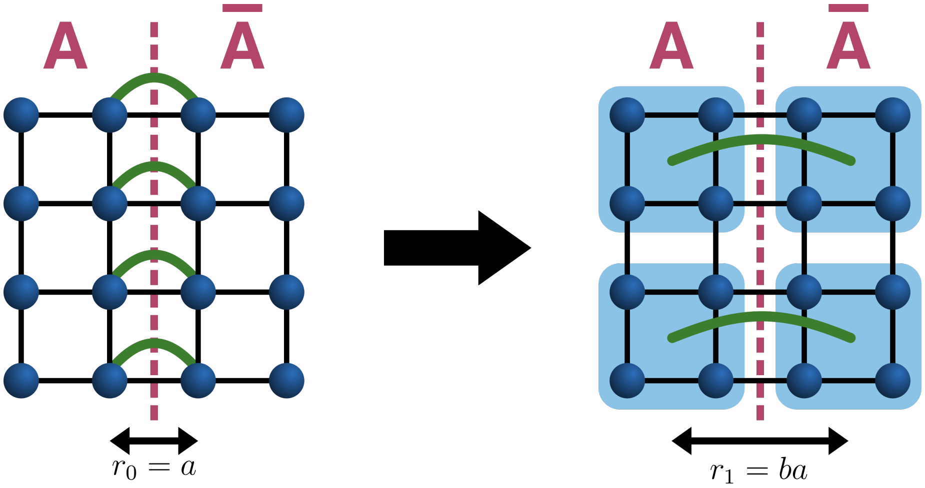

Figure 1.2: Illustration of the contributions to the entanglement entropy from the (left) zeroth and (right) first renormalization group steps. The dashed line corresponds to the entanglement boundary and the green curves represent the entanglement contributions at the characteristic length scale r_n.

now the effects of the system boundaries on the entanglement scaling forms, although we will examine the effects of such boundaries within Chapter 2.

From our second assumption, at a given length scale r we expect the contribution $S_\alpha(A, r)$ to the entanglement entropy to be given by an integral of some local geometric quantity $g_\alpha(A, r)$ over the boundary ∂A such that [12, 13]

$$S_\alpha(A, r) = \int_{\partial A} \mathrm{d}\Sigma_{d-1}\, g_\alpha(A, r), \tag{1.35}$$

where $g_\alpha(A, r)$ has a functional form that depends on the local curvature of ∂A. The quantity $\mathrm{d}\Sigma_{d-1}$ is a dimensionless differential surface element parametrizing the $(d-1)$-dimensional boundary ∂A at length scale r, which can be written as

$$\mathrm{d}\Sigma_{d-1} = \frac{\mathrm{d}s_{d-1}}{r^{d-1}}, \tag{1.36}$$

where $\mathrm{d}s_{d-1}$ is a differential surface element with units of length to the power of $(d-1)$.

Overall, we thus expect that the entanglement entropy for a critical theory is given by

$$S_\alpha(A) = \int_a^{L_A} \mathrm{d}(\log r) \left[\int_{\partial A} \mathrm{d}\Sigma_{d-1}\, g_\alpha(A, r)\right]. \tag{1.37}$$

1.5.2 Flat boundaries

The simplest case to consider is the one where the boundary of region A is a flat $(d-1)$-dimensional hyperplane extending across the entire system of length L. For example, such a boundary is a straight line in $2+1$ dimensions and a plane in $3+1$ dimensions. In such a case, the local geometric quantity $g_\alpha(A, r) = g_{\alpha,\text{flat}}(r)$ is a constant across the boundary for all RG length scales r such that $g_{\alpha,\text{flat}}(r) = c_{\alpha,0}$. From Equation (1.35), the contribution to the entanglement entropy at length scale r is then given by

$$\begin{aligned} S_{\alpha,\text{flat}}(r) &= \int_{\partial A} \frac{\mathrm{d}s_{d-1}}{r^{d-1}}\, c_{\alpha,0} \\ &= \frac{c_{\alpha,0}}{r^{d-1}} \int_{\partial A} \mathrm{d}s_{d-1} \\ &= c_{\alpha,0} \left(\frac{L}{r}\right)^{d-1}, \end{aligned} \tag{1.38}$$

where, although not explicitly written, the constant $c_{\alpha,0}$ can also in general depend upon the dimensionality d.

Integrating as in Equation (1.34), the entanglement entropy is thus given by

$$\begin{aligned} S_{\alpha,\text{flat}} &= c_{\alpha,0} \int_a^L \frac{\mathrm{d}r}{r} \left(\frac{L}{r}\right)^{d-1} \\ &= c_{\alpha,0} L^{d-1} \int_a^L \mathrm{d}r \frac{1}{r^d} \\ &= \begin{cases} c_{\alpha,0} \log\left(\dfrac{L}{a}\right) & \text{(for } d = 1\text{)}, \\ \dfrac{c_{\alpha,0}}{d-1}\left[\left(\dfrac{L}{a}\right)^{d-1} - 1\right] & \text{(for } d > 1\text{)}. \end{cases} \end{aligned} \tag{1.39}$$

For $d > 1$, we see that we arrive at the above-mentioned area law, which has a non-universal

(UV-cutoff-dependent) coefficient $c_{\alpha,0}/[a^{d-1}(d-1)]$. In these cases, there is also a universal subleading constant given by $-c_{\alpha,0}/(d-1)$.

For a one-dimensional critical theory, in place of the area law we predict a logarithmic scaling with a universal coefficient, which is in fact well-established in the literature [14, 15, 16, 17, 18, 19]. We explicitly study this one-dimensional logarithmic scaling for the case of free bosonic systems in Section 2.5.1.

1.5.3 Hyperspherical boundaries

Let us now consider the case where region A has a smooth hyperspherical boundary in $(d+1)$-dimensional space-time. Although hyperspherical boundaries cannot be realized exactly on hypercubic lattices, such boundaries have been studied analytically and numerically in the continuum limit [20, 21, 22, 23, 24]. In Section 2.4.2, we show numerically that the universal coefficient associated with spherical boundary is in fact of similar form (as a function of α) to the coefficient corresponding to a sharp corner in $d = 3$.

For hyperspherical boundaries, we expect the integrand $g_\alpha(A, r) = g_{\alpha,\text{sphere}}(r)$ to have corrections that depend upon the curvature $\kappa = 1/R$ of region A, where R is the radius of the hypersphere. In general, $g_{\alpha,\text{sphere}}(r)$ can be some Taylor series expansion in powers of κ. However, this expansion is constrained by the fact that we must have $S_\alpha(A) = S_\alpha(\overline{A})$. If region A has curvature $1/R$, then the same boundary in region $\overline{A}$ has curvature $-1/R$. We therefore find that we are limited to an expansion in even powers of the curvature such that [25, 13]

$$g_{\alpha,\text{sphere}}(r) = c_{\alpha,0} + c_{\alpha,1}\left(\frac{r}{L}\right)^2 + c_{\alpha,2}\left(\frac{r}{L}\right)^4 + \dots, \tag{1.40}$$

where we have assumed that $R \sim L$ and thus that the (dimensionless) curvature at length scale r is given by $r/R \sim r/L$.

The contribution to the entanglement entropy at RG length scale r is thus given by

$$\begin{aligned} S_{\alpha,\text{sphere}}(r) &= \int_{\partial A} \frac{\mathrm{d}s_{d-1}}{r^{d-1}} \left[c_{\alpha,0} + c_{\alpha,1}\left(\frac{r}{L}\right)^2 + c_{\alpha,2}\left(\frac{r}{L}\right)^4 + \dots\right] \\ &= \left[\frac{c_{\alpha,0}}{r^{d-1}} + \frac{c_{\alpha,1}}{L^2 r^{d-3}} + \frac{c_{\alpha,2}}{L^4 r^{d-5}} + \dots\right] \times L^{d-1}. \end{aligned} \tag{1.41}$$

Even spatial dimensions

When d is even, Equation (1.41) can be written as

$$S_{\alpha,\text{sphere}}(r) = \left[\frac{c_{\alpha,0}}{r^{d-1}} + \frac{c_{\alpha,1}}{L^2 r^{d-3}} + \ldots + \frac{c_{\alpha,\frac{d}{2}-1}}{L^{d-2} r} + \frac{c_{\alpha,\frac{d}{2}} r}{L^d} + \frac{c_{\alpha,\frac{d}{2}+1} r^3}{L^{d+2}} + \ldots\right] \times L^{d-1}, \quad (1.42)$$

and the total entanglement entropy is then given by [26, 25]

$$\begin{aligned} S_{\alpha,\text{sphere}} &= \int_a^L \mathrm{d}r \left[c_{\alpha,0} \frac{L^{d-1}}{r^d} + c_{\alpha,1} \frac{L^{d-3}}{r^{d-2}} + \ldots + c_{\alpha,\frac{d}{2}-1} \frac{L}{r^2} + c_{\alpha,\frac{d}{2}} \frac{1}{L} + c_{\alpha,\frac{d}{2}+1} \frac{r^2}{L^3} + \ldots\right] \\ &= \left[-\frac{c_{\alpha,0} L^{d-1}}{(d-1) r^{d-1}} - \frac{c_{\alpha,1} L^{d-3}}{(d-3) r^{d-3}} - \ldots - \frac{c_{\alpha,\frac{d}{2}-1} L}{r} + \frac{c_{\alpha,\frac{d}{2}}\, r}{L} + \frac{c_{\alpha,\frac{d}{2}+1} r^3}{3L^3} + \ldots\right]\Bigg|_{r=a}^{r=L} \\ &= \frac{c_{\alpha,0}}{d-1} \left(\frac{L}{a}\right)^{d-1} + \frac{c_{\alpha,1}}{d-3} \left(\frac{L}{a}\right)^{d-3} + \ldots + c_{\alpha,\frac{d}{2}-1} \frac{L}{a} - c_{\alpha,\frac{d}{2}} \frac{a}{L} - c_{\alpha,\frac{d}{2}+1} \left(\frac{a}{L}\right)^3 - \ldots \\ &\qquad - \frac{c_{\alpha,0}}{d-1} - \frac{c_{\alpha,1}}{d-3} - \ldots - c_{\alpha,\frac{d}{2}-1} + c_{\alpha,\frac{d}{2}} + \frac{c_{\alpha,\frac{d}{2}+1}}{3} + \ldots. \end{aligned} \quad (1.43)$$

We see that the entanglement entropy in this case consists of terms proportional to odd powers of L/a or a/L as well a universal constant (the sum of the terms in the last line). Note that there is no correction term proportional to $\log\left(\frac{L}{a}\right)$.

Odd spatial dimensions

Following a similar procedure, when d is odd one can write

$$S_{\alpha,\text{sphere}}(r) = \left[\frac{c_{\alpha,0}}{r^{d-1}} + \frac{c_{\alpha,1}}{L^2 r^{d-3}} + \ldots + \frac{c_{\alpha,\frac{d-3}{2}}}{L^{d-3} r^2} + \frac{c_{\alpha,\frac{d-1}{2}}}{L^{d-1}} + \frac{c_{\alpha,\frac{d+1}{2}} r^2}{L^{d+1}} + \ldots\right] \times L^{d-1}. \quad (1.44)$$

Upon integrating over r, the entanglement entropy is given by [26, 25]

$$
\begin{aligned}
S_{\alpha,\text{sphere}} &= \int_a^L \mathrm{d}r \left[c_{\alpha,0} \frac{L^{d-1}}{r^d} + c_{\alpha,1} \frac{L^{d-3}}{r^{d-2}} + \ldots + c_{\alpha,\frac{d-3}{2}} \frac{L^2}{r^3} + c_{\alpha,\frac{d-1}{2}} \frac{1}{r} + c_{\alpha,\frac{d+1}{2}} \frac{r}{L^2} + \ldots \right] \\
&= \left[\frac{-c_{\alpha,0} L^{d-1}}{(d-1) r^{d-1}} - \frac{c_{\alpha,1} L^{d-3}}{(d-3) r^{d-3}} - \ldots - \frac{c_{\alpha,\frac{d-3}{2}} L^2}{2r^2} + c_{\alpha,\frac{d-1}{2}} \log r + \frac{c_{\alpha,\frac{d+1}{2}} r^2}{2L^2} + \ldots \right] \Bigg|_{r=a}^{r=L} \\
&= \frac{c_{\alpha,0}}{d-1} \left(\frac{L}{a} \right)^{d-1} + \frac{c_{\alpha,1}}{d-3} \left(\frac{L}{a} \right)^{d-3} + \ldots + \frac{c_{\alpha,\frac{d-3}{2}}}{2} \left(\frac{L}{a} \right)^2 + c_{\alpha,\frac{d-1}{2}} \log \left(\frac{L}{a} \right) \\
&\quad - \frac{c_{\alpha,\frac{d+1}{2}}}{2} \left(\frac{a}{L} \right)^2 - \ldots - \frac{c_{\alpha,0}}{d-1} - \frac{c_{\alpha,1}}{d-3} - \ldots - \frac{c_{\alpha,\frac{d-3}{2}}}{2} + \frac{c_{\alpha,\frac{d+1}{2}}}{2} + \ldots .
\end{aligned}
\tag{1.45}
$$

The entanglement entropy here consists of terms proportional to even powers of L/a or a/L as well as a term proportional to $\log(L/a) = \log L - \log a$. The logarithmic term $\log L$ has a universal coefficient and, in $d = 3$, this term is the leading correction to the area law. We note that the constant contirbution here is non-universal since it includes the term proportional to $\log a$.

1.5.4 Boundaries with sharp vertices and wedges

In addition to flat and hyperspherical entanglement boundaries, we consider situations where region A has one or more sharp corners. In particular, we consider regions in d spatial dimensions that are formed from the intersection of d linearly independent hyperplanes. For example, in Fig. 1.3 we show examples of such regions in $d = 2$ and $d = 3$. In two spatial dimensions, we consider entanglement geometries with vertices having opening angles θ, as illustrated in Fig. 1.3a. In three spatial dimensions, we similarly consider trihedral vertices formed from three planes intersecting at various angles, as shown in Fig 1.3b.

In considering the entanglement entropy $S_{\alpha,\text{sharp}}$ from such regions, we expect to find area law contributions from the flat hyperplanes as well as additional subleading corrections due to the places where the hyperplanes meet. Let us denote by $S_{\alpha,p}$ the contribution to $S_{\alpha,\text{sharp}}$ due to the location where p hyperplanes meet (where $p = 1, 2, \ldots, d$). Then $S_{\alpha,1}$ is the area law contribution and we have

$$
S_{\alpha,\text{sharp}} = \sum_{p=1}^{d} S_{\alpha,p}. \tag{1.46}
$$

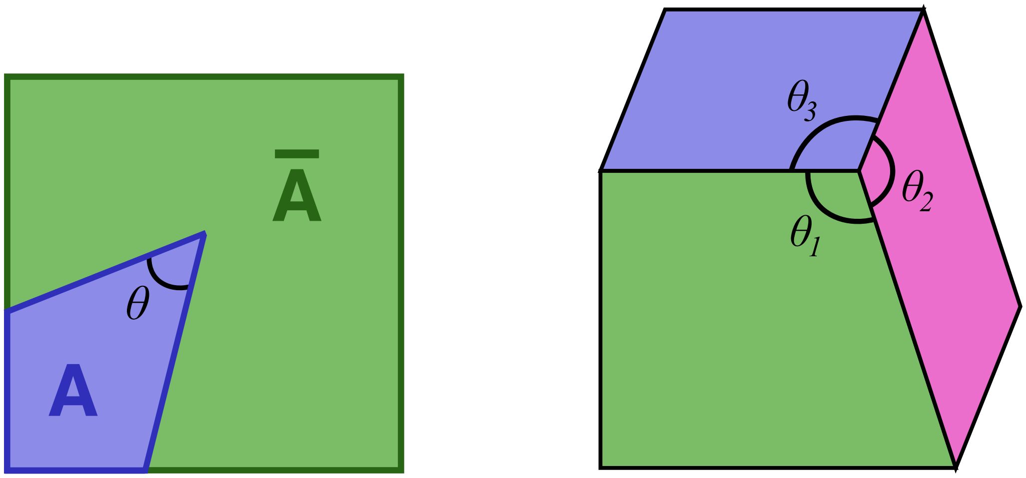

(a) (b)

Figure 1.3: Examples of entanglement boundaries with sharp corners. In (a), we consider a boundary in $d = 2$ with an opening angle θ. In (b), we show a region A in $d = 3$ formed from three planes that meet at a point with trihedral angle $(\theta_1, \theta_2, \theta_3)$.

Since the boundary ∂A_p corresponding to the meeting of p hyperplanes is a flat $(d-p)$-dimensional surface, it follows from Equation (1.35) that the contribution $S_{\alpha,p}(r)$ at length scale r is given by [13]

$$\begin{aligned} S_{\alpha,p}(r) &= \int_{\partial A_p} \frac{\mathrm{d}s_{d-p}}{r^{d-p}}\, c_{\alpha,p-1} \\ &= c_{\alpha,p-1} \left(\frac{L}{r}\right)^{d-p}, \end{aligned} \tag{1.47}$$

where $c_{\alpha,p-1}$ is a constant that can in general depend upon the angles that parametrize the intersection of the p hyperplanes. Integrating this expression according to Equation (1.34), we find that

$$\begin{aligned} S_{\alpha,p} &= c_{\alpha,p-1} L^{d-p} \int_a^L \frac{\mathrm{d}r}{r^{d-p+1}} \\ &= \begin{cases} \dfrac{c_{\alpha,p-1}}{d-p}\left[\left(\dfrac{L}{a}\right)^{d-p} - 1\right] & \text{(for } p = 1, 2, \ldots d-1\text{)}, \\ c_{\alpha,d-1} \log\left(\dfrac{L}{a}\right) & \text{(for } p = d\text{)}. \end{cases} \end{aligned} \tag{1.48}$$

Note that for $p = 1$, we recover the area law as in Equation (1.39).

In Chapter 2, we examine sharp entanglement boundaries in $d \leq 3$. As a result, we focus on the contributions to $S_{\alpha,\text{sharp}}$ from a vertex (the intersection of d hyperplanes when $d > 1$) and from a linear wedge (the intersection of $d-1$ hyperplanes when $d > 2$). From the above expression, these contributions are given by

$$S_{\alpha,\text{vertex}} \equiv S_{\alpha,d} = v_\alpha \log\left(\frac{L}{a}\right) \qquad \text{(for } d > 1\text{)} \tag{1.49}$$

and

$$S_{\alpha,\text{wedge}} \equiv S_{\alpha,d-1} = w_\alpha \left(\frac{L}{a} - 1\right) \qquad \text{(for } d > 2\text{)}, \tag{1.50}$$

where we have introduced the notation $v_\alpha \equiv c_{\alpha,d-1}$ and $w_\alpha \equiv c_{\alpha,d-2}$. We thus expect vertices to contribute a logarithmic term with a universal coefficient to the entanglement entropy $S_{\alpha,\text{sharp}}$, while we expect wedges to contribute a linear term with a non-universal coefficient.

Chapter 2

Universal numbers in non-interacting theories

This chapter includes results from References [27], [28], [29] and [30], as well as original results not published elsewhere.

In this chapter, we consider the simplest, non-interacting limit of the quantum lattice field theory introduced in Section 1.1.2. Techniques are readily available for computing quantities such as correlations functions and Rényi entanglement entropies for such non-interacting Gaussian field theories on finite lattices. By using these techniques along with finite size scaling analysis, one can extract predictions for these quantities in the thermodynamic limit. While many critical features such as the critical exponents are well known in these theories, many of the universal numbers introduced through entanglement scaling arguments in Section 1.5 remain unexplored. Such universal quantities can provide deeper insight into the underlying critical theories characterizing Gaussian fixed points, and can set the stage for future calculations of such universal quantities in interacting theories.

The non-interacting limit of the field theory in Equation (1.15) corresponds to the case where the coefficient u of the $(\phi^2_{\mathbf{x},\alpha})^2$ term is zero such that the theory becomes Gaussian. We consider the additional simplification where $N = 1$ such that the field $\phi(\mathbf{x}, \tau) \equiv \phi_{\mathbf{x}} = \phi_{x_1,x_2,\ldots,x_d}$ is a scalar field, which corresponds to a non-interacting (free) bosonic degree of freedom. The lattice Hamiltonian in such a limit can be written as

$$H = \frac{1}{2}\sum_{\mathbf{x}} \left(\pi_{\mathbf{x}}^2 + m^2\phi_{\mathbf{x}}^2\right) + \frac{1}{2}\sum_{\langle \mathbf{x}\mathbf{x}'\rangle} \left(\phi_{\mathbf{x}} - \phi_{\mathbf{x}'}\right)^2, \tag{2.1}$$

where we have elected to work in units where the lattice spacing a is equal to one, and we have replaced the coefficient r with m^2 in order to emphasize its connection to the boson's mass. This Hamiltonian corresponds to a gapless critical theory when the boson becomes massless such that $m = 0$. We study this model on hypercubic lattices in d spatial dimensions, with linear lengths $L_1, L_2, \ldots, L_d$ along each respective lattice direction.

When the lattice Hamiltonian in Equation (2.1) has translationally-invariant boundary conditions, the corresponding Fourier-space Hamiltonian is diagonal. We thus consider the discrete decomposition of each real-space field $\phi_{\mathbf{x}}$ and $\pi_{\mathbf{x}}$ into N Fourier-space modes such that

$$\begin{aligned} \phi_{\mathbf{x}} &= \frac{1}{\sqrt{N}}\sum_{\mathbf{k}} \phi_{\mathbf{k}} e^{i\mathbf{k}\cdot\mathbf{x}}, \\ \pi_{\mathbf{x}} &= \frac{1}{\sqrt{N}}\sum_{\mathbf{k}} \pi_{\mathbf{k}} e^{i\mathbf{k}\cdot\mathbf{x}}, \end{aligned} \tag{2.2}$$

and, correspondingly,

$$\begin{aligned} \phi_{\mathbf{k}} &= \frac{1}{\sqrt{N}}\sum_{\mathbf{x}} \phi_{\mathbf{x}} e^{-i\mathbf{k}\cdot\mathbf{x}}, \\ \pi_{\mathbf{k}} &= \frac{1}{\sqrt{N}}\sum_{\mathbf{x}} \pi_{\mathbf{x}} e^{-i\mathbf{k}\cdot\mathbf{x}}. \end{aligned} \tag{2.3}$$

Using these relations along with the commutation relations in Equation (1.16), the corresponding commutation relations for the Fourier-space fields $\phi_{\mathbf{k}}$ and momenta $\pi_{\mathbf{k}'}$ are given by

$$\begin{gathered} [\phi_{\mathbf{k}}, \phi_{\mathbf{k}'}] = [\pi_{\mathbf{k}}, \pi_{\mathbf{k}'}] = 0, \\ [\phi_{\mathbf{k}}, \pi_{-\mathbf{k}'}] = i\delta_{\mathbf{k}\mathbf{k}'}, \end{gathered} \tag{2.4}$$

and the lattice Hamiltonian can then be written in diagonal form as

$$\begin{aligned} H &= \frac{1}{2}\sum_{\mathbf{k}} \Big[\pi_{\mathbf{k}}\pi_{-\mathbf{k}} + \left[(2-2\cos k_1) + (2-2\cos k_2) + \ldots + (2-2\cos k_d) + m^2\right]\phi_{\mathbf{k}}\phi_{-\mathbf{k}}\Big], \\ &= \frac{1}{2}\sum_{\mathbf{k}} \left[\pi_{\mathbf{k}}\pi_{-\mathbf{k}} + \omega_{\mathbf{k}}^2\phi_{\mathbf{k}}\phi_{-\mathbf{k}}\right], \end{aligned} \tag{2.5}$$

where we have defined

$$\begin{aligned}\omega_{\mathbf{k}}^2 &= (2-2\cos k_1)+(2-2\cos k_2)+\ldots+(2-2\cos k_d)+m^2\\ &= 4\sin^2\left(\frac{k_1}{2}\right)+4\sin^2\left(\frac{k_2}{2}\right)+\ldots+4\sin^2\left(\frac{k_d}{2}\right)+m^2.\end{aligned} \tag{2.6}$$

2.1 Correlation functions

We now discuss methods for calculating two-point correlation functions $\langle\phi_{\mathbf{x}}\phi_{\mathbf{x}'}\rangle$ and $\langle\pi_{\mathbf{x}}\pi_{\mathbf{x}'}\rangle$ for non-interacting field theories. Since we will see that the Fourier-space lattice Hamiltonian of Equation (2.5) can be reexpressed as a model corresponding to N independent harmonic oscillators, we start by reviewing the relevant theory for quantum oscillators in the language of creation and annihilation operators. After establishing techniques for calculating two-point correlations functions for free bosonic fields, we perform explicit calculations of such correlators and compare with the expected scaling forms introduced in Section 1.2.

2.1.1 Harmonic oscillator

The Hamiltonian corresponding to a quantum harmonic oscillator can be written in the language of second quantization as

$$H_{\text{osc}} = \omega\left(a_{\text{osc}}^\dagger a_{\text{osc}} + \frac{1}{2}\right), \tag{2.7}$$

where ω is the (positive) oscillator frequency, $a_{\text{osc}}^\dagger$ is known as a creation operator and a_{osc} is an annihilation operator. These operators satisfy the commutation relation

$$\left[a_{\text{osc}}, a_{\text{osc}}^\dagger\right] = 1. \tag{2.8}$$

The eigenstates of H_{osc} are orthonormal Fock states $|n\rangle$, which can be constructed by acting with the creation operator on the vacuum state $|0\rangle$ such that

$$|n\rangle = \frac{1}{\sqrt{n!}}\left(a_{\text{osc}}^\dagger\right)^n|0\rangle. \tag{2.9}$$

The creation and annihilation operators act on the state $|n\rangle$ such that

$$\begin{aligned} a_{\text{osc}}^{\dagger}|n\rangle &= \sqrt{n+1}\,|n+1\rangle\,, \\ a_{\text{osc}}|n\rangle &= \sqrt{n}\,|n-1\rangle\,, \\ a_{\text{osc}}^{\dagger}a_{\text{osc}}|n\rangle &= n\,|n\rangle\,, \end{aligned} \tag{2.10}$$

where we note that a special case of the second equation is that $a_{\text{osc}}|0\rangle = 0$ such that the annihilation operator destroys the vacuum state. The operator $a_{\text{osc}}^{\dagger}a_{\text{osc}}$ is referred to as the number operator since it acts on $|n\rangle$ to yield a non-negative integer n known as the boson occupation number. The expectation value of this number operator is given by

$$\left\langle a_{\text{osc}}^{\dagger}a_{\text{osc}}\right\rangle = \langle n|\,a_{\text{osc}}^{\dagger}a_{\text{osc}}\,|n\rangle = n. \tag{2.11}$$

The eigenenergies of H_{osc} are given by $\omega\left(n+\frac{1}{2}\right)$, so that the ground state corresponds to $n=0$.

2.1.2 Translationally invariant free bosonic fields

Consider again the diagonal free scalar Hamiltonian in Fourier space, as given in Equation (2.5). Let us define creation and annihilation operators corresponding to each of the N Fourier modes such that

$$\begin{aligned} a_{-\mathbf{k}}^{\dagger} &= \frac{1}{\sqrt{2\omega_{\mathbf{k}}}}\left(\omega_{\mathbf{k}}\phi_{\mathbf{k}} - i\pi_{\mathbf{k}}\right), \\ a_{\mathbf{k}} &= \frac{1}{\sqrt{2\omega_{\mathbf{k}}}}\left(\omega_{\mathbf{k}}\phi_{\mathbf{k}} + i\pi_{\mathbf{k}}\right), \end{aligned} \tag{2.12}$$

and, inversely,

$$\begin{aligned} \phi_{\mathbf{k}} &= \frac{1}{\sqrt{2\omega_{\mathbf{k}}}}\left(a_{-\mathbf{k}}^{\dagger} + a_{\mathbf{k}}\right), \\ \pi_{\mathbf{k}} &= i\sqrt{\frac{\omega_{\mathbf{k}}}{2}}\left(a_{-\mathbf{k}}^{\dagger} - a_{\mathbf{k}}\right). \end{aligned} \tag{2.13}$$

Using Equation (2.4), we see that these creation and annihilation operators commute according to

$$\begin{aligned} \left[a_{\mathbf{k}}, a_{\mathbf{k}'}\right] &= \left[a_{\mathbf{k}}^{\dagger}, a_{\mathbf{k}'}^{\dagger}\right] = 0, \\ \left[a_{\mathbf{k}}, a_{\mathbf{k}'}^{\dagger}\right] &= \delta_{\mathbf{k}\mathbf{k}'}, \end{aligned} \tag{2.14}$$

which is in agreement with Equation (2.8). The free scalar Hamiltonian can be expressed in terms of these new operators as

$$H = \sum_{\mathbf{k}} \omega_{\mathbf{k}} \left(a_{\mathbf{k}}^{\dagger} a_{\mathbf{k}} + \frac{1}{2} \right). \tag{2.15}$$

Comparing with Section 2.1.1, we thus see that the free scalar Hamiltonian can be expressed in Fourier space as a sum over N independent harmonic oscillators. The orthonormal eigenstates $|n\rangle$ of H are labelled by the boson occupation numbers $n_{\mathbf{k}}$ for each Fourier mode $\mathbf{k}$ such that

$$|n\rangle = \prod_{\mathbf{k}} \left[\frac{1}{\sqrt{n_{\mathbf{k}}!}} \left(a_{\mathbf{k}}^{\dagger} \right)^{n_{\mathbf{k}}} \right] |0\rangle = \bigotimes_{\mathbf{k}} |n_{\mathbf{k}}\rangle, \tag{2.16}$$

and the creation and annihilation operators act on $|n\rangle$ analogously to Equation (2.10) such that

$$\begin{aligned} a_{\mathbf{k}} |n\rangle &= \sqrt{n_{\mathbf{k}}} \, |n_{\mathbf{k}} - 1\rangle \otimes \left[\bigotimes_{\mathbf{k}' \neq \mathbf{k}} |n_{\mathbf{k}'}\rangle \right], \\ a_{\mathbf{k}}^{\dagger} |n\rangle &= \sqrt{n_{\mathbf{k}} + 1} \, |n_{\mathbf{k}} + 1\rangle \otimes \left[\bigotimes_{\mathbf{k}' \neq \mathbf{k}} |n_{\mathbf{k}'}\rangle \right], \\ a_{\mathbf{k}}^{\dagger} a_{\mathbf{k}} |n\rangle &= n_{\mathbf{k}} |n\rangle . \end{aligned} \tag{2.17}$$

From here, one can then calculate the expectation values in the $|n\rangle$ basis as

$$\begin{aligned} \left\langle a_{\mathbf{k}}^{\dagger} a_{\mathbf{k}'}^{\dagger} \right\rangle &= \left\langle a_{\mathbf{k}} a_{\mathbf{k}'} \right\rangle = 0, \\ \left\langle a_{\mathbf{k}}^{\dagger} a_{\mathbf{k}'} \right\rangle &= n_{\mathbf{k}} \delta_{\mathbf{k}\mathbf{k}'}. \end{aligned} \tag{2.18}$$

Using these expectation values along with the expressions for $\phi_{\mathbf{k}}$ and $\pi_{\mathbf{k}}$ from Equation (2.13), the two-point correlators for the Fourier-space fields are given by

$$\begin{aligned} \langle \phi_{\mathbf{k}} \phi_{-\mathbf{k}'} \rangle &= \frac{1}{2\sqrt{\omega_{\mathbf{k}} \omega_{-\mathbf{k}}}} \left(1 + n_{\mathbf{k}} + n_{-\mathbf{k}} \right) \delta_{\mathbf{k}\mathbf{k}'}, \\ \langle \pi_{\mathbf{k}} \pi_{-\mathbf{k}'} \rangle &= \frac{\sqrt{\omega_{\mathbf{k}} \omega_{-\mathbf{k}}}}{2} \left(1 + n_{\mathbf{k}} + n_{-\mathbf{k}} \right) \delta_{\mathbf{k}\mathbf{k}'}. \end{aligned} \tag{2.19}$$

For all that follows, we are interested in properties corresponding to the system's ground state. In this case, there are no bosonic excitations and we can set $n_{\mathbf{k}} = 0$ for all $\mathbf{k}$. The ground state two-point correlators thus given by

$$\begin{aligned}\langle \phi_{\mathbf{k}}\phi_{-\mathbf{k}'}\rangle_0 &= \frac{1}{2\omega_{\mathbf{k}}}\delta_{\mathbf{k}\mathbf{k}'},\\ \langle \pi_{\mathbf{k}}\pi_{-\mathbf{k}'}\rangle_0 &= \frac{\omega_{\mathbf{k}}}{2}\delta_{\mathbf{k}\mathbf{k}'},\end{aligned} \tag{2.20}$$

where we have also used the fact that $\omega_{\mathbf{k}} = \omega_{-\mathbf{k}}$ (see Equation (2.6)). If we now perform an inverse Fourier transform, we find that the real-space ground-state correlators are given by

$$\begin{aligned}\langle \phi_{\mathbf{x}}\phi_{\mathbf{x}'}\rangle_0 &= \frac{1}{2N}\sum_{\mathbf{k}}\frac{e^{i\mathbf{k}\cdot(\mathbf{x}-\mathbf{x}')}}{\omega_{\mathbf{k}}},\\ \langle \pi_{\mathbf{x}}\pi_{\mathbf{x}'}\rangle_0 &= \frac{1}{2N}\sum_{\mathbf{k}}\omega_{\mathbf{k}}e^{i\mathbf{k}\cdot(\mathbf{x}-\mathbf{x}')}.\end{aligned} \tag{2.21}$$

When performing numerical calculations, we consider lattices with finite lengths $L_1, L_2, \ldots, L_d$ along each dimension. As a result, we must take into account possible effects at the lattice edges and carefully choose boundary conditions. Here, we consider cases where the boundary conditions impose some sort of translational invariance (which was assumed in deriving Equation (2.21)).

A lattice system is periodic along a given real-space lattice direction x_i if the fields $\phi_{\mathbf{x}}$ and momenta $\pi_{\mathbf{x}}$ satisfy the periodic boundary conditions (PBC)

$$\begin{aligned}\phi_{\mathbf{x}} &= \phi_{\mathbf{x}+L_i\hat{\mathbf{x}}_{\mathbf{i}}},\\ \pi_{\mathbf{x}} &= \pi_{\mathbf{x}+L_i\hat{\mathbf{x}}_{\mathbf{i}}},\end{aligned} \tag{2.22}$$

for every lattice site $\mathbf{x}$. Similarly, a lattice system has antiperiodic boundary conditions (APBC) along x_i when

$$\begin{aligned}\phi_{\mathbf{x}} &= -\phi_{\mathbf{x}+L_i\hat{\mathbf{x}}_{\mathbf{i}}},\\ \pi_{\mathbf{x}} &= -\pi_{\mathbf{x}+L_i\hat{\mathbf{x}}_{\mathbf{i}}}.\end{aligned} \tag{2.23}$$

Using the Fourier series expansion in Equation (2.2), these conditions then imply that

$$\sum_{\mathbf{k}}\phi_{\mathbf{k}}e^{i\mathbf{k}\cdot\mathbf{x}} = \pm\sum_{\mathbf{k}}\phi_{\mathbf{k}}e^{i\mathbf{k}\cdot\mathbf{x}}e^{ik_iL_i}, \tag{2.24}$$

and similarly for $\pi_{\mathbf{x}}$, where the plus sign corresponds to PBC and the negative sign to APBC. In order to have this expression satisfied for every lattice site $\mathbf{x}$, we must have

$e^{ik_iL_i} = \pm 1$. The values for k_i are thus quantized such that $k_i = 2n_i\pi/L_i$ (for PBC) or $k_i = (2n_i + 1)\pi/L_i$ (for APBC), where n_i can be any integer. However, since $e^{i\mathbf{k}\cdot\mathbf{x}}$ is invariant when $k_i \to k_i + 2n_i\pi$, we restrict sums over k_i to the first Brillouin zone such that $-\pi \leq k_i < \pi$ or, equivalently, $0 \leq k_i < 2\pi$. As a result, we restrict the integers n_i to the range $n_i = 0, 1, \ldots, L_i - 1$. The Fourier modes are thus quantized such that

$$k_i = \begin{cases} \dfrac{2n_i\pi}{L_i} & \text{(PBC)} \\ \dfrac{(2n_i+1)\pi}{L_i} & \text{(APBC)} \end{cases} \qquad \text{with } n_i = 0, 1, \ldots, L_i - 1. \tag{2.25}$$

When the lattice system has either PBC or APBC along each lattice direction, the ground-state two-point correlators in Equations (2.21) then simplify to give [31]

$$\begin{aligned} \langle \phi_{\mathbf{x}} \phi_{\mathbf{x}'} \rangle_0 &= \frac{1}{2L_1L_2 \cdots L_d} \sum_{\mathbf{k}} \frac{\cos\left[k_1\left(x_1 - x_1'\right)\right] \cos\left[k_2\left(x_2 - x_2'\right)\right] \cdots \cos\left[k_d\left(x_d - x_d'\right)\right]}{\omega_{\mathbf{k}}}, \\ \langle \pi_{\mathbf{x}} \pi_{\mathbf{x}'} \rangle_0 &= \frac{1}{2L_1L_2 \cdots L_d} \sum_{\mathbf{k}} \omega_{\mathbf{k}} \cos\left[k_1\left(x_1 - x_1'\right)\right] \cos\left[k_2\left(x_2 - x_2'\right)\right] \cdots \cos\left[k_d\left(x_d - x_d'\right)\right], \end{aligned} \tag{2.26}$$

where we have made use of the fact that $\sum_{k_i} e^{ik_i\left(x_i - x_i'\right)}/\omega_{\mathbf{k}} = \sum_{k_i} \cos\left[k_i\left(x_i - x_i'\right)\right]/\omega_{\mathbf{k}}$ since the contribution at k_i from $\sin\left[k_i\left(x_i - x_i'\right)\right]/\omega_{\mathbf{k}}$ is cancelled by the corresponding contribution at $2\pi - k_i$.

In cases where the lattice has PBC in all directions and the bosonic fields are massless ($m = 0$), there exists a value of $\mathbf{k}$ known as a "zero mode" in the above sums such that $k_1 = k_2 = \ldots = k_d = 0$ and thus $\omega_{\mathbf{k}} = 0$. The correlator $\langle \phi_{\mathbf{x}} \phi_{\mathbf{x}'} \rangle_0$ diverges for such boundary conditions. In order to avoid this divergence, we consider systems with either a finite mass or with non-periodic boundary conditions in at least one lattice direction.

2.1.3 Quadratic Hamiltonians

In the previous section, we derived the ground-state two-point correlation functions corresponding to non-interacting scalar fields on lattices with translationally-invariant boundary conditions (specifically, PBC or APBC along each lattice direction). However, we will encounter situations in the following sections where we wish to study non-interacting scalar fields on lattice without translational invariance. In particular, when we use the numerical linked cluster expansion in Section 2.4.1, we will consider systems where the fields ϕ and π are restricted to be zero outside of the lattice.

Here, we find that we can use another strategy [32, 33] to calculate such correlation functions for more general Hamiltonians that are quadratic (Gaussian) in the fields $\phi_{\mathbf{x}}$ and $\pi_{\mathbf{x}}$ such that

$$H_{\text{quad}} = \frac{1}{2}\sum_{\mathbf{x}} \pi_{\mathbf{x}}^2 + \frac{1}{2}\sum_{\mathbf{x},\mathbf{x}'} \phi_{\mathbf{x}} K_{\mathbf{x}\mathbf{x}'} \phi_{\mathbf{x}'}, \tag{2.27}$$

where K is a positive-definite matrix so that it can be diagonalized by an orthogonal matrix Q. We can thus write $K = QDQ^T$, where D is a diagonal matrix made up of the (real, positive) eigenvalues of K and $QQ^T = Q^TQ = \mathbb{I}$. The above Hamiltonian can be written in terms of Q and D as

$$H_{\text{quad}} = \frac{1}{2}\sum_{\mathbf{x},\mathbf{q},\mathbf{x}'} \left(\pi_{\mathbf{x}} Q_{\mathbf{x}\mathbf{q}} Q^T_{\mathbf{q}\mathbf{x}'} \pi_{\mathbf{x}'} + \phi_{\mathbf{x}} Q_{\mathbf{x}\mathbf{q}} D_{\mathbf{q}\mathbf{q}} Q^T_{\mathbf{q}\mathbf{x}'} \phi_{\mathbf{x}'}\right). \tag{2.28}$$

Let us now introduce new fields $\widetilde{\phi}_{\mathbf{q}} = \sum_{\mathbf{x}} Q^T_{\mathbf{q}\mathbf{x}} \phi_{\mathbf{x}} = \sum_{\mathbf{x}} Q_{\mathbf{x}\mathbf{q}} \phi_{\mathbf{x}}$ and $\widetilde{\pi}_{\mathbf{q}} = \sum_{\mathbf{x}} Q_{\mathbf{x}\mathbf{q}} \pi_{\mathbf{x}}$. These fields preserve the commutation relations in Equation (1.16) and diagonalize H_{quad} such that

$$H_{\text{quad}} = \frac{1}{2}\sum_{\mathbf{q}} \left(\widetilde{\pi}_{\mathbf{q}}^2 + D_{\mathbf{q}\mathbf{q}} \widetilde{\phi}_{\mathbf{q}}^2\right). \tag{2.29}$$

One can now use a procedure very similar to that used in Section 2.1.2 to find the correlation functions. Specifically, if we introduce creation operators and annihilation operators defined by

$$\begin{aligned} a^\dagger_{\mathbf{q}} &= \frac{1}{\sqrt{2} D_{\mathbf{q}}^{1/4}} \left(D_{\mathbf{q}\mathbf{q}}^{1/2}\, \widetilde{\phi}_{\mathbf{q}} - i\, \widetilde{\pi}_{\mathbf{q}}\right), \\ a_{\mathbf{q}} &= \frac{1}{\sqrt{2} D_{\mathbf{q}}^{1/4}} \left(D_{\mathbf{q}\mathbf{q}}^{1/2}\, \widetilde{\phi}_{\mathbf{q}} + i\, \widetilde{\pi}_{\mathbf{q}}\right), \end{aligned} \tag{2.30}$$

then we can write H_{quad} as a sum of independent harmonic oscillators as in Equation (2.15), but with ω replaced by $D^{1/2}$. By analogy with Equation (2.20), the ground-state two-point correlation functions for the new fields $\widetilde{\phi}_{\mathbf{q}}$ and $\widetilde{\pi}_{\mathbf{q}}$ can be expressed as

$$\begin{aligned}\langle \phi_{\mathbf{q}} \phi_{\mathbf{q}'} \rangle_0 &= \frac{1}{2D_{\mathbf{qq}}^{1/2}} \delta_{\mathbf{qq}'}, \\ \langle \pi_{\mathbf{q}} \pi_{\mathbf{q}'} \rangle_0 &= \frac{D_{\mathbf{qq}}^{1/2}}{2} \delta_{\mathbf{qq}'},\end{aligned} \tag{2.31}$$

and the corresponding correlation functions for the original fields on the real-space lattice are given by

$$\begin{aligned}\langle \phi_{\mathbf{x}} \phi_{\mathbf{x}'} \rangle_0 &= \frac{1}{2} \sum_{\mathbf{q}} Q_{\mathbf{xq}} D_{\mathbf{qq}}^{-1/2} Q_{\mathbf{qx}'}^T = \frac{1}{2} \left(K^{-1/2}\right)_{\mathbf{xx}'}, \\ \langle \pi_{\mathbf{x}} \pi_{\mathbf{x}'} \rangle_0 &= \frac{1}{2} \left(K^{1/2}\right)_{\mathbf{xx}'}.\end{aligned} \tag{2.32}$$

2.1.4 Scaling of correlation functions

Armed with the tools for calculating two-point correlation functions in Gaussian theories from the previous sections, we now perform explicit calculations of the two-point correlations functions for the free bosonic field theory of Equation (2.1). From Section 1.2, away from criticality we expect such correlators to experience an exponential decay as a function of the separation $r = |\mathbf{x} - \mathbf{x}'|$ for $r \gg \xi$. As the system becomes critical such that $\xi \to \infty$ (which corresponds to the boson becoming massless in this case), we expect to instead observe correlation functions that decay with r according to a power law.

In Figure 2.1, we plot the two-point correlation function $\langle \phi_{\mathbf{x}} \phi_{\mathbf{x}'} \rangle_0$ for the case of a free boson on a lattice in three spatial dimensions ($d = 3$) with PBC along all lattice directions. We fix the separation to be $r = L/4$ and consider the correlation function as a function of the lattice size L. As a result of having PBC along all directions, we cannot set $m = 0$ due to the resulting divergences discussed in Section 2.1.2. While the free boson is only critical when the boson is precisely massless, we observe a clear crossover to critical power-law scaling behaviour for the finite lattice sizes studied as we take the limit $m \to 0$.

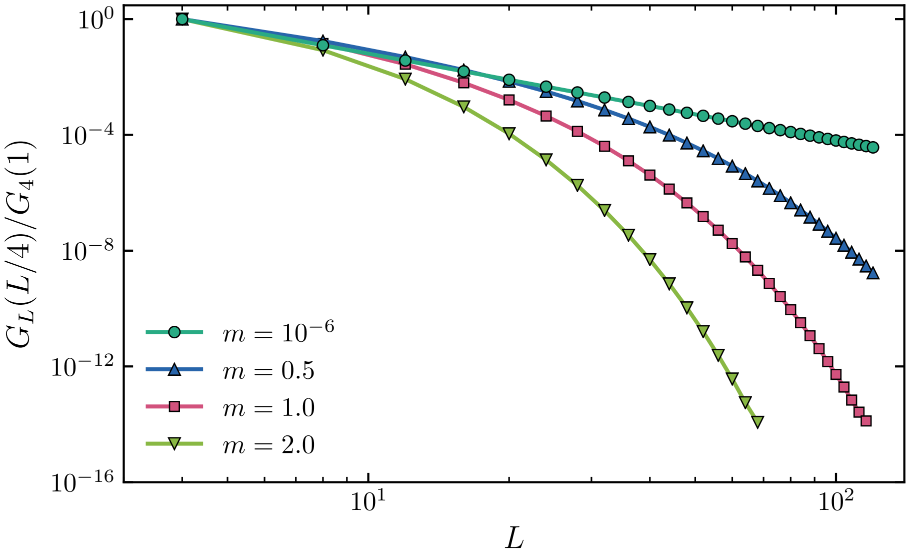

Figure 2.1: The correlation function $G_L(x) \equiv \left\langle \phi_{(0,0,0)}\phi_{(x,0,0)} \right\rangle_0 (L)$ as a function of the lattice length scale L for non-interacting scalar fields in $d = 3$ and for $x = L/4$, where the lattice has PBC in all lattice directions. Note the logarithmic scale on both axes. The y-axis is normalized so that all of the curves coincide at $L = 4$. We observe a crossover to power-law scaling as $m \to 0$ (which corresponds to the system becoming critical).

2.2 Entanglement entropy

We now turn to calculations of the entanglement entropy and the more general Rényi entropies of Equations (1.30) and (1.31), with the ultimate goal of using such entropies to extract universal quantities from certain entanglement boundaries as discussed in Section 1.5. As first introduced by Peschel in 2003, any reduced density matrix ρ_A for a non-interacting Gaussian theory can be calculated from knowledge of the ground-state two-point correlation functions $\langle \phi_{\mathbf{x}} \phi_{\mathbf{x}'} \rangle_0$ and $\langle \pi_{\mathbf{x}} \pi_{\mathbf{x}'} \rangle_0$ [34]. In fact, such a calculation only requires knowledge of the correlation functions for pairs of sites $(\mathbf{x}, \mathbf{x}')$ that are both in region A, such that relatively few correlators are required to determine ρ_A for cases of lattice systems where region A is small. After determining the density matrix, one can then use its eigenvalues to determine the desired Rényi entropies for any Rényi index α [32].

In this section, we establish certain properties about density matrices in non-interacting theories, and then develop the general algorithm discussed above for calculating the Rényi entropies corresponding to any entanglement boundary. We also present a more efficient algorithm that is applicable to cases where the entanglement region A possesses some type of translational symmetry.

2.2.1 Reduced density matrix and modular Hamiltonian

For non-interacting bosonic field theories, the ground-state density matrix $\rho_{A\overline{A}} = |0\rangle\langle 0|$ is some Gaussian function of the fields $\phi_{\mathbf{x}}$ and momenta $\pi_{\mathbf{x}}$ (where $|0\rangle$ represents the system's ground state). As a result, all correlators $\langle\mathcal{O}\rangle = \mathrm{Tr}\left(\rho_{A\overline{A}}\mathcal{O}\right)$ satisfy Wick's theorem, where the operator $\mathcal{O}$ can be any product of field and momentum variables.

Let us consider now an operator $\mathcal{O}_A$ that is a product of fields $\phi_{\mathbf{x}}$ and momenta $\pi_{\mathbf{x}}$, with all sites $\mathbf{x}$ in the product constrained to region A. Then since $\rho_{A\overline{A}} = \rho_A \otimes \rho_{\overline{A}}$, we can say that $\langle\mathcal{O}_A\rangle = \mathrm{Tr}\left(\rho_{A\overline{A}}\mathcal{O}_A\right) = \mathrm{Tr}\left(\rho_A\mathcal{O}_A\right)$. Since $\langle\mathcal{O}_A\rangle$ must satisfy Wick's theorem, it then follows that the reduced density matrix ρ_A must also be a Gaussian function.

The reduced density matrix can thus, in general, be expressed as [34, 32]

$$\rho_A = \mathcal{K}\exp\left[-\sum_{\mathbf{x},\mathbf{x}'\in A}\pi_{\mathbf{x}}M_{\mathbf{x}\mathbf{x}'}\pi_{\mathbf{x}'} + \phi_{\mathbf{x}}N_{\mathbf{x}\mathbf{x}'}\phi_{\mathbf{x}'}\right], \tag{2.33}$$

or, after diagonalizing,

$$\rho_A = \mathcal{K}\exp\left[-\sum_{\ell}\epsilon_\ell a_\ell^\dagger a_\ell\right], \tag{2.34}$$

where ϵ_ℓ is the eigenenergy of mode ℓ and $\mathcal{K}$ is a normalization constant. As in Sections 2.1.2 and 2.1.3, the creation operators $a_\ell^\dagger$ and annihilation operators a_ℓ are linear combinations of the fields $\phi_{\mathbf{x}}$ and the canonical momenta $\pi_{\mathbf{x}}$.

We can think of this reduced density matrix for region A as describing a mixed quantum state at finite temperature. Considering units where this temperature and the Boltzmann constant are equal to one, we can then express ρ_A as

$$\rho_A = \mathcal{K}e^{-H_A}, \tag{2.35}$$

where H_A is called the *modular Hamiltonian*, which acts only on sites in A. For a free theory, we know from Equations (2.33) and (2.34) that H_A is quadratic and given by

$$\begin{aligned} H_A &= \sum_{\mathbf{x},\mathbf{x}'\in A} \pi_{\mathbf{x}} M_{\mathbf{x}\mathbf{x}'} \pi_{\mathbf{x}'} + \phi_{\mathbf{x}} N_{\mathbf{x}\mathbf{x}'} \phi_{\mathbf{x}'} \\ &= \sum_{\ell} \epsilon_\ell a_\ell^\dagger a_\ell, \end{aligned} \tag{2.36}$$

where $a_\ell^\dagger a_\ell$ is again a bosonic number operator, whose eigenvalues n_ℓ can be thought of in the language of second quantization as the number of quasi-particles in state ℓ with energy ϵ_ℓ. For bosons, there is no restriction on the occupation number n_ℓ from the Pauli exclusion principle, and n_ℓ can be equal to any non-negative integer. The overall state of subsystem A can be written in terms of these occupation numbers as

$$|n\rangle_A = \bigotimes_\ell |n_\ell\rangle_A \,. \tag{2.37}$$

Recall that the global system is in its pure ground state so that we set $n_{\mathbf{k}} = 0$ for all $\mathbf{k}$ in Section 2.1.2. Here, however, the modular Hamiltonian is not the physical lattice Hamiltonian. ρ_A corresponds to a mixed state (as one would have at finite temperature) and we have, in general, $n_\ell \neq 0$ for all modes ℓ.

Let us now consider how to use Equation (2.36) along with the constraint that $\operatorname{Tr}\rho_A = 1$ in order solve for the normalization constant $\mathcal{K}$ in Equation (2.35) (which will prove to be useful in Sections 2.2.2 and 2.2.3 when calculating the entanglement entropy). First, note that the elements of ρ_A are given by

$$(\rho_A)_{nn'} = \langle n| \mathcal{K} e^{-\sum_\ell \epsilon_\ell a_\ell^\dagger a_\ell} |n'\rangle = \mathcal{K}\left(\prod_\ell e^{-\epsilon_\ell n_\ell}\right)\delta_{nn'}, \tag{2.38}$$

so that the probability of being in state $|n\rangle$ is given by $\mathcal{K}\left(\prod_\ell e^{-\epsilon_\ell n_\ell}\right)$.

The density matrix can then be written as

$$\rho_A = \sum_n \rho_{nn} |n\rangle\langle n| = \mathcal{K} \bigotimes_\ell \left(\sum_{n_\ell} e^{-\epsilon_\ell n_\ell} |n_\ell\rangle\langle n_\ell|\right). \tag{2.39}$$

The trace of ρ_A is then

$$\begin{aligned}\operatorname{Tr}\rho_A &= \mathcal{K}\prod_\ell\left(\sum_{n_\ell} e^{-\epsilon_\ell n_\ell}\right)\\ &= \mathcal{K}\prod_\ell\left(1+e^{-\epsilon_\ell}+e^{-2\epsilon_\ell}+\ldots\right)\\ &= \mathcal{K}\prod_\ell\left(\frac{1}{1-e^{-\epsilon_\ell}}\right),\end{aligned} \tag{2.40}$$

where we have used the geometric series $\sum_{n=0}^{\infty} r^n = 1/(1-r)$ for $r \neq 1$.

Since we must have $\operatorname{Tr}\rho_A = 1$, we thus find that the normalization constant is

$$\mathcal{K} = \prod_\ell\left(1-e^{-\epsilon_\ell}\right). \tag{2.41}$$

We also note that one can express n_ℓ in terms of the eigenvalues ϵ_ℓ as

$$\begin{aligned}n_\ell = \left\langle a_\ell^\dagger a_\ell\right\rangle = \operatorname{Tr}\left(\rho_A a_\ell^\dagger a_\ell\right)\\ &= \mathcal{K}\prod_{m\neq\ell}\left(\sum_{n_m} e^{-\epsilon_m n_m}\right)\times\sum_{n_\ell} n_\ell e^{-\epsilon_\ell n_\ell}\\ &= \mathcal{K}\prod_{m\neq\ell}\left(\frac{1}{1-e^{-\epsilon_m}}\right)\times\left(0+e^{-\epsilon_\ell}+2e^{-2\epsilon_\ell}+\ldots\right)\\ &= \mathcal{K}\left(\frac{1}{\mathcal{K}}\left(1-e^{-\epsilon_\ell}\right)\right)\times\frac{e^{-\epsilon_\ell}}{\left(1-e^{-\epsilon_\ell}\right)^2}\\ &= \frac{1}{e^{\epsilon_\ell}-1},\end{aligned} \tag{2.42}$$

where we have differentiated the geometric sum $\sum_{n=0}^{\infty} e^{-n\epsilon} = 1/(1-e^{-\epsilon})$ with respect to ϵ to get $\sum_{n=0}^{\infty} n e^{-n\epsilon} = e^{-\epsilon}/(1-e^{-\epsilon})^2$. Equation (2.42) corresponds to the Bose-Einstein distribution.

2.2.2 Entanglement entropy from the modular Hamiltonian

We now express the von Neumann and Rényi entanglement entropies of Equations (1.30) and (1.31) in terms of the eigenenergies ϵ_ℓ in Equation (2.36). First, the von Neumann entropy is

$$\begin{aligned}
S_1(A) &= -\operatorname{Tr}\left[\rho_A \log\left(\mathcal{K} e^{-\sum_\ell \epsilon_\ell a_\ell^\dagger a_\ell}\right)\right] \\
&= -\log \mathcal{K} \operatorname{Tr}\rho_A + \operatorname{Tr}\left(\rho_A \sum_\ell \epsilon_\ell a_\ell^\dagger a_\ell\right) \\
&= -\log \mathcal{K} + \sum_\ell \epsilon_\ell \left\langle a_\ell^\dagger a_\ell \right\rangle \\
&= \sum_\ell \left[-\log\left(1 - e^{-\epsilon_\ell}\right) + \frac{\epsilon_\ell}{e^{\epsilon_\ell} - 1}\right].
\end{aligned} \tag{2.43}$$

Similarly, the Rényi entropies are given by

$$\begin{aligned}
S_\alpha(A) &= \frac{1}{1-\alpha} \log\left[\mathcal{K}^\alpha \operatorname{Tr} e^{-\alpha \sum_\ell \epsilon_\ell a_\ell^\dagger a_\ell}\right] \\
&= \frac{1}{1-\alpha}\left[\alpha \log \mathcal{K} + \log \prod_\ell \left(\sum_{n_\ell} e^{-\alpha \epsilon_\ell n_\ell}\right)\right] \\
&= \frac{1}{1-\alpha} \sum_\ell \left[\alpha \log\left(1 - e^{-\epsilon_\ell}\right) - \log\left(1 - e^{-\alpha\epsilon_\ell}\right)\right].
\end{aligned} \tag{2.44}$$

2.2.3 Entanglement entropy from correlation functions

We now show how to determine the entanglement entropies corresponding to a region A simply from knowledge of the ground-state correlation functions $\langle \phi_{\mathbf{x}} \phi_{\mathbf{x}'} \rangle_0$ and $\langle \pi_{\mathbf{x}} \pi_{\mathbf{x}'} \rangle_0$. We start by introducing matrices X_A and P_A with elements given by

$$\begin{aligned}
(X_A)_{\mathbf{x}\mathbf{x}'} &= \langle \phi_{\mathbf{x}} \phi_{\mathbf{x}'} \rangle_0 , \\
(P_A)_{\mathbf{x}\mathbf{x}'} &= \langle \pi_{\mathbf{x}} \pi_{\mathbf{x}'} \rangle_0 .
\end{aligned} \tag{2.45}$$

As discussed earlier, the field operators $\phi_{\mathbf{x}}$ and momentum operators $\pi_{\mathbf{x}}$ are linear combinations of the creation operators a_ℓ and annihilation operators $a_\ell^\dagger$ that were first introduced in Equation (2.34). In general, one can write this linear combination in terms of matrices β and γ such that

$$\begin{aligned}
\phi_{\mathbf{x}} &= \beta_{\mathbf{x}\ell}^* a_\ell^\dagger + \beta_{\mathbf{x}\ell} a_\ell, \\
\pi_{\mathbf{x}} &= -i\gamma_{\mathbf{x}\ell}^* a_\ell^\dagger + i\gamma_{\mathbf{x}\ell} a_\ell,
\end{aligned} \tag{2.46}$$

where the spatial indices $\mathbf{x}$ must be in region A since the creation and annihilation operators are only defined within this region.

In particular, it turns out that if β and γ are both real matrices and $\beta = -\frac{1}{2}\left(\gamma^T\right)^{-1}$, then the creation and annihilation operators satisfy the commutation relations in Equation (2.14) and the fields and momenta satisfy the commutation relations in Equation (1.16). Using these commutation relations along with Equations (2.45) and (2.46), one can show that [32]

$$\beta\frac{1}{4}\left(2n+1\right)^2\beta^{-1} = X_A P_A, \tag{2.47}$$

where n is the diagonal matrix of occupation numbers as defined in Equation (2.42). From Equation (2.47), we see that eigenvalues of $X_A P_A$ are given by $\frac{1}{4}\left(2n_\ell+1\right)^2$. If we define the matrix $C_A = \sqrt{X_A P_A}$, then we see that its eigenvalues ν_ℓ must be given by

$$\nu_\ell = \frac{2n_\ell + 1}{2}. \tag{2.48}$$

Then, using Equation (2.42), we find that the eigenvalues ν_ℓ of C_A are given in terms of the eigenvalues ϵ_ℓ of the modular Hamiltonian as

$$\nu_\ell = \frac{1}{2}\left(\frac{e^{\epsilon_\ell}+1}{e^{\epsilon_\ell}-1}\right) = \frac{1}{2}\coth\left(\frac{\epsilon_\ell}{2}\right), \tag{2.49}$$

and, inversely,

$$\epsilon_\ell = 2\,\mathrm{arccoth}\left(2\nu_\ell\right) = \log\left(\frac{\nu_\ell + \frac{1}{2}}{\nu_\ell - \frac{1}{2}}\right). \tag{2.50}$$

From here, one can use Equations (2.43) and (2.44) to express the entanglement entropies as

$$\begin{aligned} S_1(A) &= \sum_\ell \left[\left(\nu_\ell + \frac{1}{2}\right)\log\left(\nu_\ell + \frac{1}{2}\right) - \left(\nu_\ell - \frac{1}{2}\right)\log\left(\nu_\ell - \frac{1}{2}\right)\right], \\ S_\alpha(A) &= \frac{1}{\alpha - 1}\sum_\ell \log\left[\left(\nu_\ell + \frac{1}{2}\right)^\alpha - \left(\nu_\ell - \frac{1}{2}\right)^\alpha\right]. \end{aligned} \tag{2.51}$$

A summary of the algorithm for calculating von Neumann and Rényi entanglement entropies from two-point correlation functions is given in Algorithm 2.1.

Algorithm 2.1: Method for calculating von Neumann and Rényi entanglement entropies from the ground-state two-point correlation functions in Gaussian theories [34, 32].

```
define the boson mass m and the lattice lengths $L_1, L_2, \ldots, L_d$;
select boundary conditions (PBC, APBC, OBC, ...);
define region A;

calculate the ground-state correlators $\langle \phi_{\mathbf{x}} \phi_{\mathbf{x}'} \rangle_0$ and $\langle \pi_{\mathbf{x}} \pi_{\mathbf{x}'} \rangle_0$ for all
  pairs of sites $\{\mathbf{x}, \mathbf{x}'\}$ in region A using Equation (2.26) or (2.32);
use these correlators to form the matrices $X_A$ and $P_A$;

diagonalize the matrix $X_A P_A$ in order to calculate $C_A = \sqrt{X_A P_A}$;

use the eigenvalues $\nu_\ell$ of $C_A$ to calculate the von Neumann and Rényi
  entanglement entropies from Equation (2.51);
```

2.2.4 Entanglement entropy in the presence of translational symmetry

In cases where the entangled region A possesses translational symmetry in at least one lattice direction, one can use a more efficient algorithm to compute the Rényi entanglement entropies [35, 36, 37]. Examples of such regions include hypercylinders, which are studied in more detail in Section 2.5. These cylindrical geometries possess translational symmetry along $d-1$ lattice directions (provided that the lattice imposes PBC or APBC along these $d-1$ directions).

Let us consider a more general situation in d spatial dimensions where region A possesses translational invariance along lattice direction x_d. The lattice must thus have either PBC or APBC along this direction. One can then consider the decomposition of the fields $\phi_{\mathbf{x}}$ and $\pi_{\mathbf{x}}$ along this lattice direction such that

$$\begin{aligned} \phi_{\mathbf{x}} &= \frac{1}{\sqrt{L_d}} \sum_{k_d} e^{i k_d x_d} \; \phi_{\mathbf{x}_{d-1}}(k_d), \\ \pi_{\mathbf{x}} &= \frac{1}{\sqrt{L_d}} \sum_{k_d} e^{i k_d x_d} \; \pi_{\mathbf{x}_{d-1}}(k_d), \end{aligned} \tag{2.52}$$

where the values of k_d are quantized as in Equation (2.25) and $\mathbf{x}_{d-1} = (x_1, x_2, \ldots, x_{d-1})$

represents the remaining $d-1$ spatial coordinates.

The Hamiltonian for non-interacting scalar fields in d spatial dimensions can then be written as a sum over L_d decoupled Hamiltonians in $d-1$ spatial dimensions as

$$H = \sum_{k_d} H_{d-1}(k_d), \tag{2.53}$$

where the lower-dimensional Hamiltonians $H_{d-1}(k_d)$ are given by

$$\begin{aligned} H_{d-1}(k_d) = \frac{1}{2} \sum_{\mathbf{x}_{d-1}} \Big[\pi_{\mathbf{x}_{d-1}}(k_d)\, \pi_{\mathbf{x}_{d-1}}(-k_d) + \big(m^2 + \sin^2(k_d/2)\big)\, \phi_{\mathbf{x}_{d-1}}(k_d)\, \phi_{\mathbf{x}_{d-1}}(-k_d) \Big] \\ + \frac{1}{2} \sum_{\langle \mathbf{x}_{d-1} \mathbf{x'}_{d-1} \rangle} \Big(\phi_{\mathbf{x}_{d-1}}(k_d) - \phi_{\mathbf{x'}_{d-1}}(k_d) \Big) \Big(\phi_{\mathbf{x}_{d-1}}(-k_d) - \phi_{\mathbf{x'}_{d-1}}(-k_d) \Big). \end{aligned} \tag{2.54}$$

By comparing with the free scalar lattice Hamiltonians of Equation (2.1), we see each Hamiltonian $H_{d-1}(k_d)$ corresponds to non-interacting scalar fields in $d-1$ spatial dimensions, but with an effective mass m_{eff} given by $m_{\text{eff}}^2 = m^2 + \sin^2(k_d/2)$.

These lower-dimensional Hamiltonians are completely independent of each other, and region A is translationally invariant such that it does not depend on the spatial coordinate x_d. As a result, the Rényi entanglement entropies $S_\alpha(A)$ are given by a sum over L_d different k_d-dependent Rényi entropies $S_\alpha(A_{d-1}, k_d)$, where A_{d-1} is the projection of region A into $(d-1)$-dimensional space. Each entropy $S_\alpha(A_{d-1}, k_d)$ is calculated from the corresponding k_d-dependent Hamiltonian $H_{d-1}(k_d)$. A summary of the procedure used to calculate the entanglement entropy in the presence of such spatial translational symmetry is given in Algorithm 2.2.

This algorithm is significantly more efficient than Algorithm 2.1 due to the reduced size of the matrices that must be diagonalized. Specifically, in Algorithm 2.1 one must diagonalize a matrix of size $N_A \times N_A$, while in Algorithm 2.2 one must diagonalize L_d independent matrices of size $N_{A_{d-1}} \times N_{A_{d-1}}$, where $N_{A_{d-1}} = N_A / L_d$.

In the presence of translational symmetry along more than one lattice direction, this algorithm can be modified for further efficiency. One can decompose the fields $\phi_{\mathbf{x}}$ and $\pi_{\mathbf{x}}$ into Fourier modes along all lattice directions that possess such symmetries and follow steps analogous to those above in order to take advantage of all symmetries.

Algorithm 2.2: Method for calculating the von Neumann and Rényi entanglement entropies from the ground-state two-point correlation functions in non-interacting scalar theories for the case where the lattice and region A possess translational invariance along lattice direction x_d [35, 36, 37]. Region A is thus independent of the spatial coordinate x_d and the lattice has either PBC or APBC along lattice direction x_d. Region A is thus fully specified by region A_{d-1} in $d-1$ spatial dimensions.

```
define the boson mass m and the lattice lengths $L_1, L_2, \ldots, L_d$;
select boundary conditions along each lattice direction, with either
  PBC or APBC along lattice direction $x_d$;
quantize the values of $k_d$ as in Equation (2.25);
define region $A_{d-1}$ and the corresponding region $A$;
initialize $S_\alpha(A) = 0$ for each desired value of $\alpha$;
for each value of $k_d$ do
    calculate $S_\alpha(A_{d-1}, k_d)$ for non-interacting scalar fields with mass
      $\sqrt{m^2 + \sin^2(k_d/2)}$ in $d-1$ spatial dimensions using Algorithm 2.1;
    increment $S_\alpha(A) = S_\alpha(A) + S_\alpha(A_{d-1}, k_d)$;
end
```

2.3 Infrared entanglement entropy scaling

In Section 1.5, we saw that the entanglement entropy for critical systems is expected to scale with a leading area law with geometry-dependent subleading corrections. These terms in general depend upon the ratio L_A/a, where L_A is the characteristic length scale of the boundary and a is the lattice spacing (the UV regulator). However, on a finite system of size L, there can also be corrections that depend upon the ratios L/a and L/L_A, where L acts as the infrared (IR) regulator. Such corrections are expected to become less important on larger lattices such that we expect the IR-dependent terms to be of order $\mathcal{O}(L_A/L)$ and $\mathcal{O}(a/L)$, which can in principle be important when attempting to reliably extract subleading universal terms in the entanglement entropy.

Here, we attempt to gain insight into the functional form of the IR-dependent scaling terms. We consider the case where region A is a fixed size so that all contributions that depend on L_A/a are constant and we can isolate the contributions to the entanglement entropy from the infrared regulator. In particular, we consider the case where region A is a single site, for which the entanglement is expect to scale such that

$$S_{\alpha,\text{single}} = d_\alpha + \mathcal{O}\left(\frac{a}{L}\right), \tag{2.55}$$

where d_α is a constant.

In Figure 2.2, we plot $S_{1,\text{single}}$ as a function of the inverse IR regulator for the case of non-interacting bosonic fields. We observe that, as the boson becomes massless so that the system becomes critical, the entanglement entropy appears to scale linearly as a function of a/L in the limit $L \to \infty$. More generally, in higher dimensions, one can show analytically and numerically that this IR correction for the single-site entanglement entropy is of order $\mathcal{O}(a^{d-1}/L^{d-1})$ [28].

2.4 Entanglement entropy for sharp vertices and wedges

Recall from Section 1.5.4 that in the presence of a sharp corner (corresponding to the meeting point of d independent hyperplanes), we expect the entanglement entropy to contain a logarithmic term subleading to the area law. The coefficients of such terms are universal in the sense that they do not depend upon the system's underlying lattice scale a, and

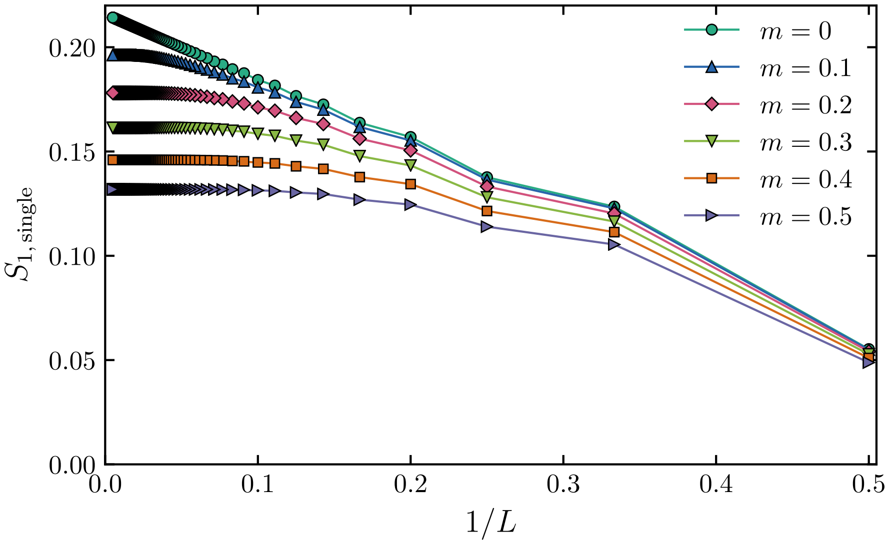

Figure 2.2: The entanglement entropy corresponding to a single site for free bosonic fields in two spatial dimensions. As the system becomes critical, we observe that the leading IR-dependent scaling term appears to be proportional to $1/L$. Note that we have set the lattice spacing equal to one.

such universal numbers can give insight into the fundamental critical theories governing the corresponding RG flows.

In three spatial dimensions on a lattice of length scale L, such a sharp corner is formed from the intersection of three linearly-independent planes that meet at a point with trihedral angle $(\theta_1, \theta_2, \theta_3)$ as in Figure 1.3b. From Equations (1.46) and (1.48), the Rényi entanglement entropies are then expected to scale such that

$$S_{\alpha,\mathrm{sharp}} = a_\alpha \left(\frac{L}{a}\right)^2 + w_\alpha \frac{L}{a} + v_\alpha \log\left(\frac{L}{a}\right) + \ldots \qquad \text{(for } d = 3\text{)}, \tag{2.56}$$

where a_α is the α-dependent coefficient of the dominant area law, w_α parametrizes the contribution to the entanglement entropy from the wedges, and v_α is the coefficient of the trihedral vertex. We note that the length scale L_A of region A is taken to be proportional to L. The coefficients w_α and v_α also depend upon the three angles θ_1, θ_2 and θ_3 that characterize the trihedral vertex.

We restrict our studies to the α-dependence of the entanglement entropy for the case where region A is formed from the intersection of three mutually perpendicular planes with trihedral angle $(\pi/2, \pi/2, \pi/2)$. However, it would be interesting to extend future studies to examine the vertex contribution to the entanglement entropy for more general trihedral angles. Such angular dependence has been studied in two spatial dimensions for both free boson and free fermion systems [28].

We note immediately that, since the logarithmic vertex term is subleading to both the area-law and wedge terms as a function of L, it can be difficult to extract such a coefficient numerically through fits to Equation (2.56). As a means of addressing this difficulty, in the next section we introduce a scheme known as the numerical linked cluster expansion, which is capable of isolating contributions to the entanglement entropy from specific geometric features. We utilize this expansion to study the vertex coefficient v_α for non-interacting bosonic fields in three spatial dimensions. We then comment on the non-universal wedge coefficient w_α and confirm the associated linear contribution to the entanglement entropy that was predicted in Section 1.5.4.

2.4.1 Numerical linked cluster expansion

The numerical linked cluster expansion [38, 39, 40, 41] (NLCE) is a powerful method that combines measurements of a property on various finite-sized lattice clusters to approach the thermodynamic limit $L \to \infty$. At a given length scale (order), this numerical expansion uses sums and differences of finite clusters to systematically cancel off lower-order finite-size and boundary effects. As a result, at a given order this procedure is capable of accessing larger-range correlations than direct calculations on finite toroidal (periodic or antiperiodic) systems of the same size. This feature becomes especially advantageous when studying behaviour at a critical point where the correlation length diverges.

For our present purposes, the NLCE offers the additional advantage that it can sum clusters in such a way as to isolate the logarithmic vertex contribution to the Rényi entopies from the leading area law and edge contributions in Equation (2.56) as well as the subleading IR corrections discussed in Section 2.3. We discuss here general properties of the NLCE as well as the techniques necessary to isolate the two- and three-dimensional vertex contribution at each cluster order. Such isolation techniques have been used successfully to study the vertex coefficient v_α for both interacting and non-interacting $(2+1)$-dimensional critical systems [42, 43, 44, 31, 28]. We extend these techniques to three dimensions in order to examine the vertex coefficient for $(3+1)$-dimensional critical free scalar theories [30].

In a translationally invariant system, the NLCE method calculates an extensive property $\mathcal{P}_{\text{ext}}$ of a lattice system $\mathcal{L}$ by summing contributions from individual clusters according to

$$\mathcal{P}_{\text{ext}}\left(\mathcal{L}\right)/N = \sum_{c} e(c) \times W(c), \tag{2.57}$$

where N characterizes the size of $\mathcal{L}$ and $e(c)$ is the embedding factor of the cluster c, which corresponds to the number of distinct reflections/rotations of c on the lattice. $W(c)$ is a weight, which is defined recursively such that

$$W(c) = \mathcal{P}_{\text{ext}}(c) - \sum_{s \in c} W(s), \tag{2.58}$$

where the sum is over all subclusters s contained in c in a graph-theoretic sense. In general, the sums in Equations (2.57) and (2.58) are over all possible subcluster geometries embeddable on the chosen lattice. However, as first discussed in Reference [42] for calculations in two spatial dimensions, these sums still converge when the geometries are restricted to rectangular clusters. Since the goal of the NLCE is to include contributions from representative clusters of maximal size, and since the number of possible clusters grows rapidly with order, it is useful to restrict the types of clusters considered in such a way. In two spatial dimensions, clusters and subclusters used within the NLCE can thus be restricted to be $u_x \times u_y$ rectangles. Similarly, in three spatial dimensions we perform calculations on regular $u_x \times u_y \times u_z$ cuboids (three-dimensional rectangles) with 6 faces, 8 vertices and 12 edges each, where u_x, u_y and u_z are integer lengths measured in units of the lattice spacing. We define the length scale (order) of a given cluster to be the maximum of these linear dimensions such that $L = \max\{u_x, u_y\}$ in $d = 2$ and $L = \max\{u_x, u_y, u_z\}$ in $d = 3$. Each cluster imposes Dirichlet open boundary conditions, with the field ϕ constrained to be zero for all lattice sites outside of the cluster.

In our calculations, we define the intensive property $\mathcal{P}$ to be the isolated vertex contribution S_{vertex} to the Rényi entanglement entropy S_α. In two (respectively, three) spatial dimensions, we imagine a single vertex arising from a quadrant (octant) of the solid geometry, and embed each rectangular (cuboidal) cluster in all possible ways around this vertex. For a given rectangular cluster c, there are N_r possible locations r for this vertex within the cluster, where $N_r = (u_x - 1)(u_y - 1)$ when $d = 2$ and $N_r = (u_x - 1)(u_y - 1)(u_z - 1)$ when $d = 3$. The overall extensive property $N_r\,\mathcal{P}(c)$ is obtained by summing over all of these possible locations such that

$$N_r\,\mathcal{P}(c) = \sum_{r} \mathcal{P}_r(c). \tag{2.59}$$

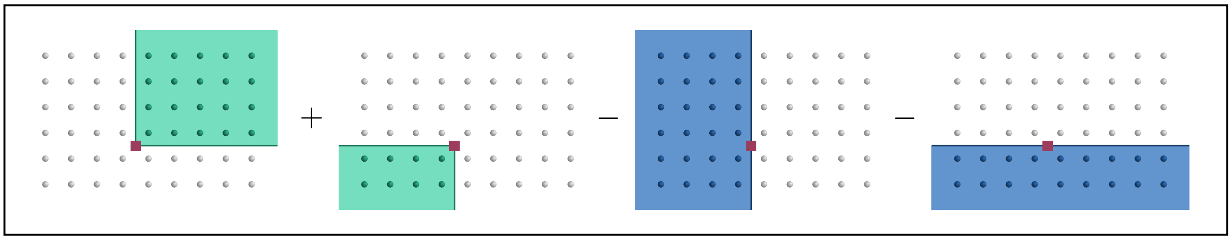

Figure 2.3: The isolation procedure used in $d = 2$ for the 9×6 cluster c for a given vertex location r (labelled by ■). We add the values of $S_\alpha(A)$ corresponding to the first two (quadrant) bipartitions, subtract the values for the last two (half-plane) bipartitions and divide the resulting sum by two in order to obtain the entanglement property $\mathcal{P}_r(c)$ corresponding to a single vertex with opening angle $\theta = \pi/2$.

In order to isolate the subleading logarithmic vertex contribution to the Rényi entropies, we perform a cluster-by-cluster subtraction procedure. For each vertex location r within the cluster c, we combine the values of $S_\alpha(A)$ corresponding to various bipartitions $\{A, \overline{A}\}$ of the cluster. The combinations of Rényi entropies are selected so as to intrinsically cancel the leading area-law and edge contributions such that $\mathcal{P}_r(c)$ (and, in turn, $\mathcal{P}(c)$) corresponds to the vertex contribution to the entropy. In $d = 2$, a combination of 4 different cluster bipartitions is used so as to cancel the dominant area-law contribution, as illustrated in Figure 2.3. In $d = 3$, a total of 13 bipartitions are used in order to cancel both the leading area-law and 90-degree edge contributions, as illustrated in Figure 2.4. The correlation function method described in Algorithm 2.1 acts as the so-called "cluster solver" since it is used to calculate all needed Rényi entropies in the above sums for each cluster.

2.4.2 Vertices in three spatial dimensions

We now use the methods outlined in previous sections to calculate the trihedral corner coefficient corresponding to the Rényi entropies in three spatial dimensions. Using the NLCE procedure described in Section 2.4.1, we isolate the corner contribution $\mathcal{P}_\alpha(\ell)$ to the Rényi entropy S_α by performing calculations on clusters up to order ℓ (the maximum linear dimension of a given cluster). From Equation (2.56), we expect for a single vertex that

$$\mathcal{P}_\alpha = v_\alpha \log \ell + d_\alpha + \dots, \tag{2.60}$$

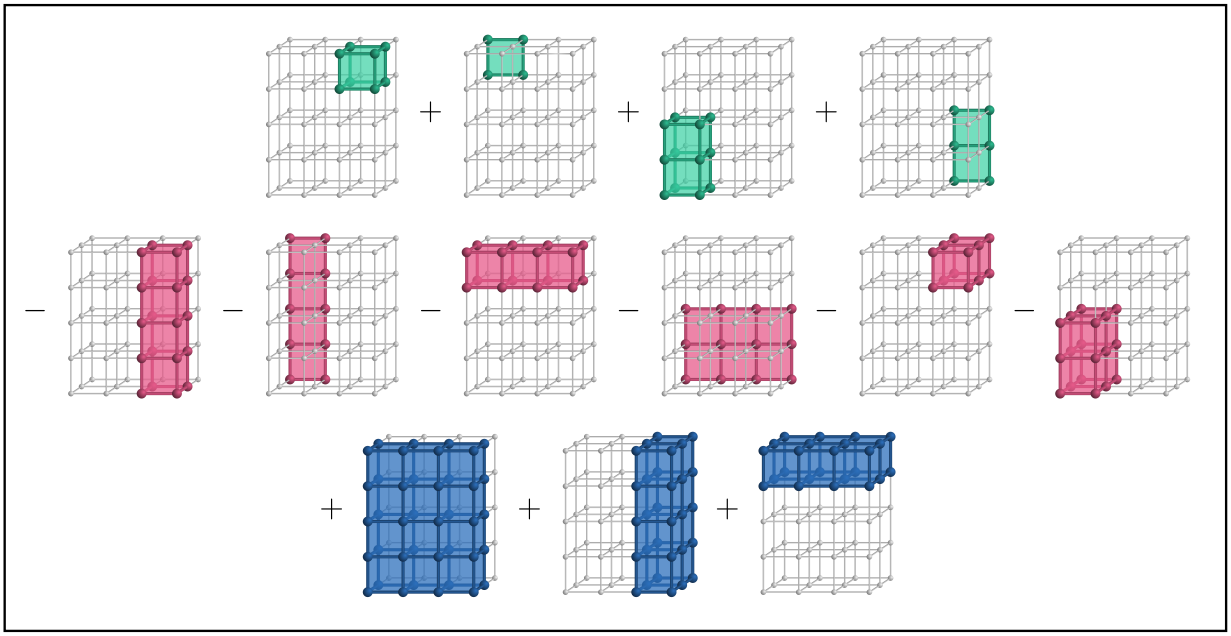

Figure 2.4: The subtraction procedure used in $d = 3$ to calculate $\mathcal{P}_r(c)$ for the $3 \times 4 \times 5$ cluster c for a given vertex location r (not labelled). We add the values of $S_\alpha(A)$ corresponding to the four octants in the top row, subtract the values for the six quadrants in the middle row, and add the values for the three half-planes in the bottom row. We divide the resulting sum by four in order to obtain $\mathcal{P}_r(c)$. This figure is taken from Reference [30].

where d_α is a subleading constant and the ellipsis indicates additional (unknown) subleading terms that should vanish as $\ell \to \infty$. ℓ is measured in units of the lattice spacing.

We examine the behavior of $\mathcal{P}_\alpha(\ell)$ as a function of ℓ with the goal of studying the vertex coefficient v_α. We first investigate what happens if we perform fits of $\mathcal{P}_\alpha$ to the two-parameter function $v_\alpha \log \ell + d_\alpha$ (ignoring, for the moment, additional subleading terms). In Figure 2.5, we illustrate such fits for $\alpha = 1$ and $\alpha = 5$. We perform fits over various ranges of the cluster order ℓ and find that for $\alpha = 1$, the extracted value of v_1 is quite stable when this range of ℓ values is varied, indicating that the unknown subleading terms in Equation (2.60) are already negligible for the cluster sizes used in our calculations. However, for $\alpha > 1$, the value of v_α increases significantly as higher orders ℓ are included in the fit and it is important to consider the effects of subleading terms. Such subleading finite-size corrections for $\alpha > 1$ have been studied numerically in lower dimensions [31], but the form of such corrections as a function of α is only known for $d = 1$ [45]. In Figure 2.6, we show the results for v_α/v_1 versus α as extracted from these various fits.

In order to approximate v_α in the thermodynamic limit $\ell \to \infty$, we study the behavior of $v_\alpha(\overline{\ell})$ versus $\overline{\ell}$, as illustrated in the insets of Figure 2.5. Here $\overline{\ell}$ is a characteristic length scale corresponding to the orders ℓ used to extract v_α from the two-parameter fits described above. We choose to define $\overline{\ell}$ as the average order such that, for instance, $\overline{\ell} = 19$ for the case where orders $\ell = 18$ to 20 are used in the initial fit of $\mathcal{P}_\alpha$ to $v_\alpha \log \ell + d_\alpha$. We could, however, use other definitions of $\overline{\ell}$ such as the minimum or maximum cluster order. We then extract the behavior of v_α for $\overline{\ell} \to \infty$ by fitting $v_\alpha(\overline{\ell})$ to the three-parameter function $v_\alpha^\infty + p_\alpha/(\overline{\ell} + q_\alpha)$. Here v_α^∞, p_α and q_α are (fitted) constants, where v_α^∞ corresponds to v_α in the thermodynamic limit and q_α reflects the ambiguity in the definition of $\overline{\ell}$ as described above. This $\overline{\ell} \to \infty$ extrapolation procedure is used for all $\alpha > 1$. For $\alpha = 1$, $v_\alpha(\overline{\ell})$ is well-converged as a function of $\overline{\ell}$ and we estimate v_α simply from the initial two-parameter fit using the highest orders available.

Recall from Section 1.5.3 that a logarithmic term is also expected in the entanglement entropy for the case where the boundary is hyperspherical in general odd spatial dimensions. In fact, for a general smooth entanglement boundary with length scale L, it has been shown that the entanglement entropy in three spatial dimensions includes a logarithmic correction to the area law such that [20, 21, 22]

$$S_{\alpha,\mathrm{smooth}} = a_\alpha \left(\frac{L}{a}\right)^2 + u_{\alpha,\mathrm{smooth}} \log\left(\frac{L}{a}\right) + \ldots \qquad \text{(for } d = 3\text{)}, \tag{2.61}$$

where the universal coefficient u_α depends upon the structure of the entangling surface as well as upon the Rényi index α.

For the case of non-interacting scalar fields, the coefficient u_α corresponding to a sphere in $3+1$ dimensions has been shown (through numerical [23] and analytical [24] studies) to depend on α according to

$$u_{\alpha,\mathrm{sphere}} = -\frac{(1+\alpha)(1+\alpha^2)}{360\alpha^3}. \tag{2.62}$$

For general smooth entangling geometries, the curvature of the boundary changes the coefficient of this logarithmic term. However, for free scalar fields, all smooth boundaries

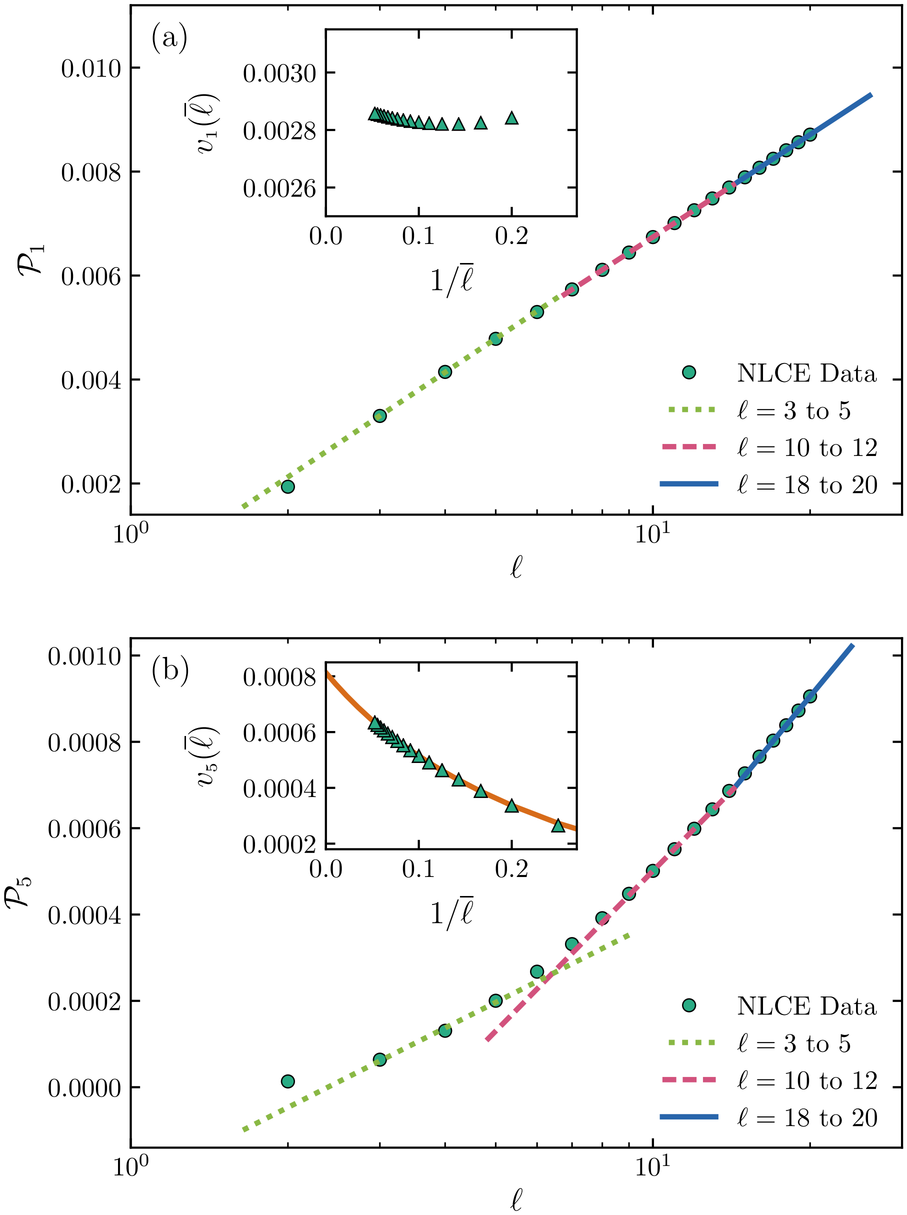

Figure 2.5: Fits of the corner contribution $\mathcal{P}_\alpha$ to the equation $v_\alpha \log \ell + d_\alpha$ for Rényi indices (a) $\alpha = 1$ and (b) $\alpha = 5$. The insets illustrates how the coefficients v_α extracted from these fits depend on the range of values of ℓ. For $\alpha > 1$, we perform a second fit to extrapolate to the thermodynamic limit, as explained in the main text.

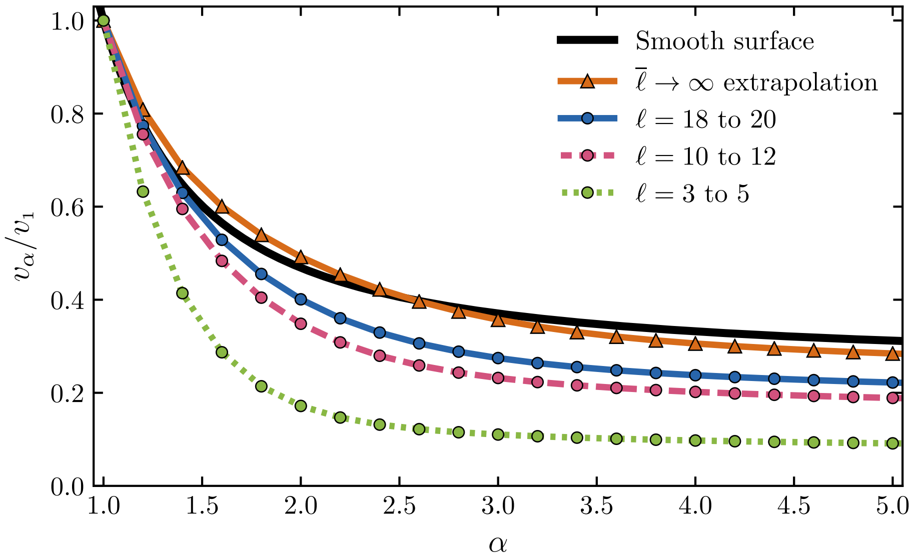

Figure 2.6: The normalized logarithmic corner coefficient v_α/v_1 as a function of the Rényi index α. These results are based on the fitting procedure illustrated in Figure 2.5. For smooth surfaces, this ratio of logarithmic coefficients is known to behave as in Equation (2.63).

yield the same functional dependence on α such that [21, 22, 46]

$$\frac{u_{\alpha,\text{smooth}}}{u_{1,\text{smooth}}} = \frac{(1+\alpha)(1+\alpha^2)}{4\alpha^3}. \tag{2.63}$$

Figure 2.6 shows that as higher orders are used in our fits, the results for the normalized corner coefficient v_α/v_1 as a function of α approaches the functional behavior of Equation (2.63). Extrapolating to the infinite-size limit as described above provide relatively good agreement with this functional form, although we are not able to quantify the agreement due to unknown finite-size errors within the NLCE procedure. We note that we do not necessarily expect our data for the sharp vertex coefficient to converge to Equation (2.63) in the thermodynamic limit since this equation has only been proven valid for locally smooth entangling geometries.

In addition to considering the ratio v_α/v_1, we also consider the unnormalized coefficients v_α. Reference [47] previously suggested that this logarithmic corner coefficient may be related to the logarithmic coefficient $u_{\alpha,\text{sphere}}$ for spherical surfaces in three spatial dimensions according to $v_\alpha \approx u_{\alpha,\text{sphere}}/8$. Considering our results for $\alpha = 1$ (where the unknown finite-size effect are least significant), we find that

$$v_1 \approx 0.00286 = -2.06 \times \left(\frac{u_{1,\text{sphere}}}{8}\right), \tag{2.64}$$

such that our results differ both in magnitude and in sign from the predictions of Reference [47].

2.4.3 Wedges in three spatial dimensions

We now present numerical calculations of the contribution to the Rényi entropy from a boundary with a 90-degree wedge. As discussed in Section 1.5.4 and Equation (2.56), we expect this contribution to be of the form $S_{\alpha,\text{wedge}} = w_\alpha\, f(\ell)$ with $f(\ell) = \ell$, where ℓ is the length of the edge measured in units of the lattice length scale a. Here, we investigate the validity of this prediction for linear scaling behaviour. We compare fits of our numerical results with this linear functional dependence and also with $f(\ell) = \ell \log \ell$, which is a functional dependence that results from other scaling arguments (for example, from deriving the cuboid scaling from the sharp limit of a smoothed cube [30]).

In these calculations, we forego the NLCE and instead study directly the behavior of the full entanglement entropy $S_\alpha(A)$ for various regions A. We use Algorithm 2.2 to calculate $S_\alpha(A)$ for cases where the full system is an $\ell \times \ell \times \ell$ cubic lattice (*i.e.* $L_x = L_y = L_z \equiv \ell$) and subregion A comprises an $\ell/2 \times \ell/2 \times \ell$ quadrant of the system (with ℓ even). We expect the entropies to scale as in Eq. (2.56), but without the logarithmic term (since the entangling surface ∂A does not contain any corners) such that

$$S_{\alpha,\text{quadrant}}(\ell) = 2a_\alpha \ell^2 + 4\, S_{\alpha,\text{wedge}} + d_\alpha + \ldots, \tag{2.65}$$

where $2\ell^2$ is the area of ∂A, and $S_{\alpha,\text{wedge}}$ appears with a factor of 4 since the boundary ∂A has 4 distinct edges. We perform calculations for various combinations of PBC and APBC along each lattice direction of the full system.

To compare the functional forms $f(\ell) = \ell$ and $f(\ell) = \ell \log \ell$ for $S_{\alpha,\text{wedge}}$, we perform least-squares fits of our numerical data for $S_{\alpha,\text{quadrant}}(\ell)$ to the three-parameter function $2a_\alpha \ell^2 + w_\alpha f(\ell) + d_\alpha$. We quantify the goodness of the fit by calculating the error

$$\Delta_\alpha = \sum_{i=1}^{n_\ell} \left(S_{\alpha,\text{quadrant}}(\ell_i) - \left[2a_\alpha \ell_i^2 + w_\alpha f(\ell_i) + d_\alpha\right]\right)^2, \tag{2.66}$$

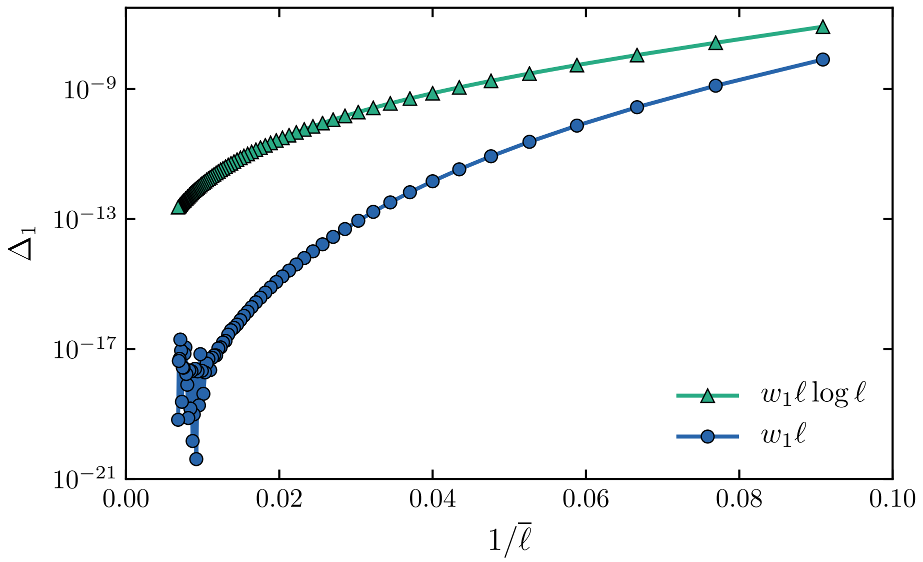

Figure 2.7: The fitting errors Δ_1 that result from fitting free boson data for $S_{1,\text{quadrant}}(\ell)$ to the form $a_1\ell^2 + w_1 f(\ell) + d_1$ for $f(\ell) = \ell \log \ell$ and $f(\ell) = \ell$. Note the logarithmic scale on the y-axis. We use $n_\ell = 4$ consecutive even values of ℓ for each fit, and define $\overline{\ell}$ to be the average of these 4 values. Note that the noise at high $\overline{\ell}$ is due to numerical issues of floating-point precision.

where n_ℓ is the number of values of ℓ used in the fit.

Recall that in Section 2.4.2, we found that the unknown subleading corrections to the entropies were least significant for the von Neumann entropy ($\alpha = 1$). We thus initially focus on our data for $S_{1,\text{quadrant}}$. We perform fits over several ranges of the lattice length scale ℓ, with $n_\ell = 4$. In Figure 2.7, we illustrate results for the error Δ_1 as a function of the average length $\overline{\ell}$ used in the fit. This plot imposes PBC along the x and y lattice directions and APBC along z, and we find similar results for other combinations of boundary conditions. We conclude that, indeed, the linear function $f(\ell) = \ell$ provides a superior characterization of the wedge contribution to the entropy since for large ℓ, the corresponding errors Δ_1 are several orders of magnitude lower than those corresponding to $f(\ell) = \ell \log \ell$.

We also carry out this comparison for higher Rényi entropies up to $\alpha = 5$. We consistently find that Δ_α is significantly lower for the fits with $f(\ell) = \ell$ for all of these other values of α. As discussed above, such fits for $\alpha \neq 1$ are more prone to effects from unknown finite-size corrections, but such corrections should vanish in the thermodynamic limit.

Unlike the logarithmic coefficient coming from the trihedral corner, the wedge coefficient w_α is non-universal since it depends upon the lattice spacing a. One expects this dependence on the microscopic lattice structure to cancel out in the ratio w_α/w_1 such that this ratio is universal. However, the limited resolution of length scales on a lattice (amounting to errors in each length scale on the order of the lattice spacing) means that the area law term in Equation (2.56) can "pollute" the edge contribution and generate order one errors in the coefficient w_α. As a result, the above lattice calculations do not produce reliable estimates for the universal ratios w_α/w_1. Additional numerical methods are required in order to circumvent these issues, and such calculations are an avenue for future work.

2.5 Entanglement entropy for cylinders

In this section, we extract universal quantities from the Rényi entanglement entropies for cases where the lattice system is divided into two hypercylinders with PBC or APBC along each lattice direction, as illustrated in Figure 2.8 for $d = 1$, 2 and 3. We consider lattices with lengths $L_i = L_{x_i}$ along each lattice direction x_i, where $1 \leq i \leq d$ and we use the convention $x_1 \equiv x$, $x_2 \equiv y$ and $x_3 \equiv z$. This hypercylindrical geometry is translationally invariant along all but one lattice direction, which we choose to be the x direction in all that follows. We define the variables $b_i = L_x/L_i$ to correspond to the aspect ratios of the lattice.

From Section 1.5.2 and, in particular, Equation (1.39) , we expect the Rényi entanglement entropies corresponding to a flat entanglement boundary to scale with a dominant area law in $d > 1$ (or a dominant logarithmic term when $d = 1$) along with a subleading universal constant. Although this constant does not depend upon the UV cutoff a, it can in general depend upon the Rényi index α, upon the aspect ratios b_i of the lattice and upon the ratio $u \equiv L_A/L_x$. We thus expect to find that [27]

$$S_{\alpha,\text{cylinder}} = \begin{cases} a_\alpha \log\left(\dfrac{L}{a}\right) + \chi_\alpha(u) + \ldots & \text{(for } d = 1\text{)}, \\ a_\alpha \dfrac{L_2 \times L_3 \times \cdots \times L_d}{a^{d-1}} + \chi_\alpha(b_2, b_3, \ldots, b_d, u) + \ldots & \text{(for } d > 1\text{)}, \end{cases} \tag{2.67}$$

where a_α is a non-universal coefficient and χ_α is the universal constant described above. The ellipsis corresponds to additional (unknown) subleading terms that vanish in the thermodynamic limit $a/L_i \to \infty$. Recall that this equation was derived without considering

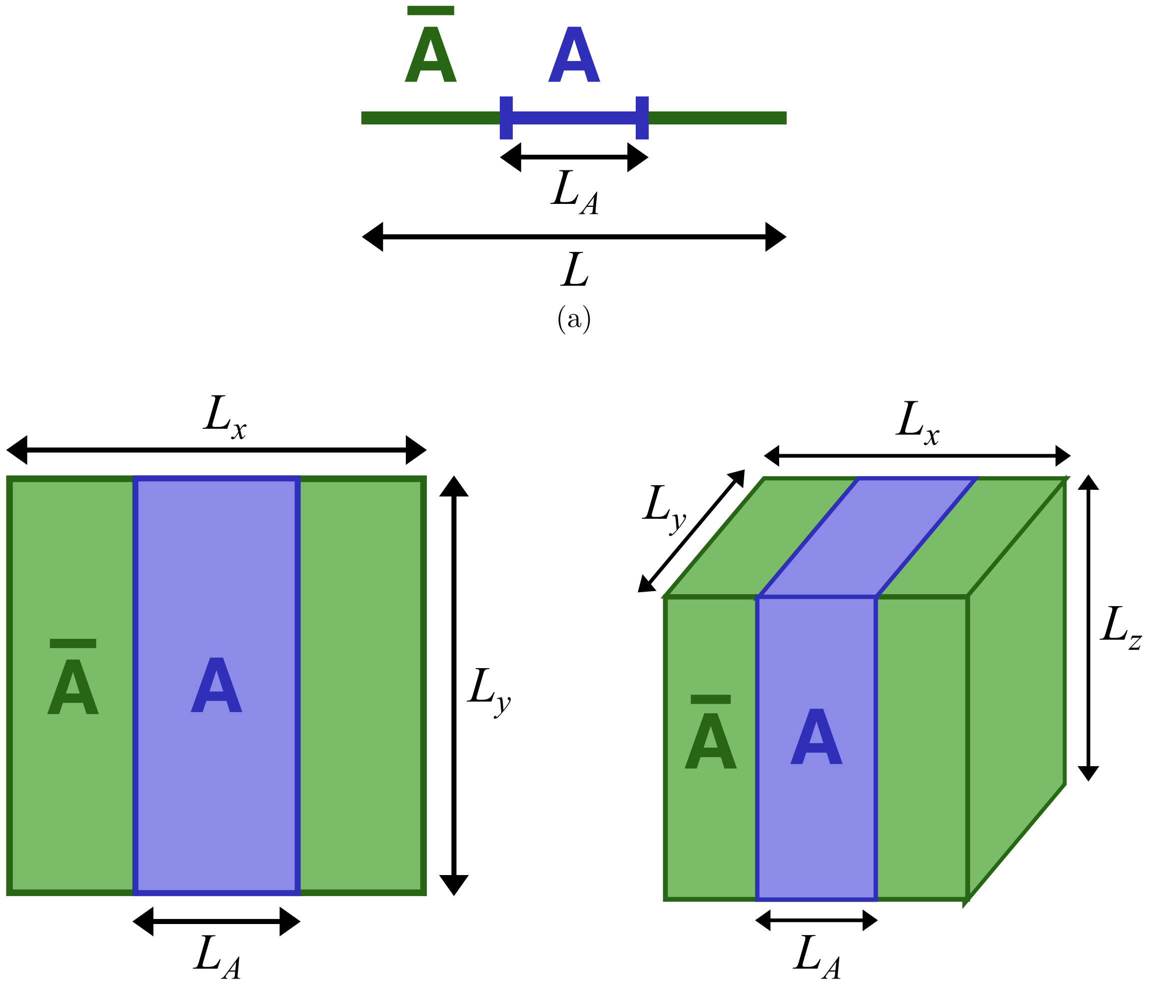

(a)

(b)

(c)

Figure 2.8: The entanglement boundaries used to study universal subleading corrections to the area law due to cylindrical boundaries in (a) $d = 1$, (b) $d = 2$ and (c) $d = 3$. We consider situations where the system has either PBC or APBC along each lattice direction.

any boundary effects due to the finite system. In what follows, we find that such finite-size and boundary effects play a role in the functional form of χ_α.

Since we wish to study the entanglement entropy in the ground state, we can make use of the reflective property that $S_\alpha(A) = S_\alpha(\overline{A})$, and thus $\chi_\alpha(u) = \chi_\alpha(1-u)$. We therefore restrict many of our plots to the regime where $0 \leq u \leq \frac{1}{2}$. Further, since we do not expect any singular behaviour in the limit where $u \to \frac{1}{2}$, one can use this reflective property to express $\chi_\alpha(u)$ for u near $\frac{1}{2}$ as

$$\chi_\alpha\left(b_2, b_3, \ldots, b_d, u \approx \frac{1}{2}\right) = \sum_{m=0}^{\infty} \beta_m \left(u - \frac{1}{2}\right)^{2m}, \tag{2.68}$$

where the coefficients β_m in general depend upon the aspect ratios $b_2, b_3, \ldots, b_d$.

Let us now consider the thin-cylinder limit where $L_A \ll L_i$ for all lattice directions i. One expects that the entanglement entropy is limited to contributions from length scales L_A and below and, as a result, the finite system's boundary has negligible effect on the functional form of χ_α when $L_A \to 0$ [27]. One can then use the same techniques as in Section 1.5.2 to predict the scaling of the entanglement entropy (and, in particular, the subleading term χ_α), but with the length scale r limited to the range a to L_A such that

$$\begin{aligned} S_{\alpha,\text{thin}} &= c_{\alpha,0}\, L_2 \times L_3 \times \cdots \times L_d \int_a^{L_A} \mathrm{d}r \frac{1}{r^d} \\ &= \frac{c_{\alpha,0}}{d-1} L_2 \times L_3 \times \cdots \times L_d \left[\frac{1}{a^{d-1}} - \frac{1}{L_A^{d-1}}\right] \qquad \text{(for } d > 1\text{)}, \end{aligned} \tag{2.69}$$

where we recall that $c_{\alpha,0}$ is a constant that depends upon both the Rényi index α and the spatial dimension d.

The first term in this expression is just the area law, while the second term predicts that χ_α behaves in the thin-cylinder limit according to [32]

$$\left.\begin{aligned} \chi_\alpha(b_2, b_3, \ldots, b_d, u \to 0) &= -\kappa_\alpha \frac{L_2 \times L_3 \times \cdots \times L_d}{L_A^{d-1}} \\ &= \frac{-\kappa_\alpha}{b_2 \times b_3 \times \cdots \times b_d} \times \frac{1}{u^{d-1}} \end{aligned}\right\} \quad \text{(for } d > 1\text{)}, \tag{2.70}$$

where $\kappa_\alpha = c_{\alpha,0}/(d-1)$ is a universal coefficient. This coefficient has been computed for non-interacting scalar fields for $2 \leq d \leq 5$ by numerically solving an integral equation corresponding to the continuum limit in Reference [32]. We examine this thin-cylinder limit for $d = 2$ and $d = 3$, for which we expect

$$\begin{aligned}\chi_\alpha^{d=2}(b_y, u \to 0) &= \frac{-\kappa_\alpha^{d=2}}{b_y\, u}, \\ \chi_\alpha^{d=3}(b_y, b_z, u \to 0) &= \frac{-\kappa_\alpha^{d=3}}{b_y b_z\, u^2}.\end{aligned} \tag{2.71}$$

Recall from Section 1.5.4 that for a corner with opening angle θ in two spatial dimensions (see Figure 1.3a), we expect the entanglement entropy to scale according to $S_{\alpha,\text{corner}}^{d=2} = a_\alpha L/a + v_\alpha(\theta)\log(L/a) + \ldots$, where the ground state imposes the reflective property $v_\alpha(\theta) = v_\alpha(\pi - \theta)$. In fact, it was shown in Reference [32] that in the limit where $\theta \to 0$, the corner coefficient for non-interacting theories behaves such that $v_\alpha \to -\kappa_\alpha^{d=2}/\theta$, where $\kappa_\alpha^{d=2}$ is the same universal coefficient as in Equation (2.71). In Figure 2.9, we consider whether such a relationship between the universal numbers for the cylinder and the corner holds away from the thin-cylinder limit. We set $\alpha = 1$ and compare the universal functions $\chi_1^{d=2}(u)$ and $v_1(\theta)$ after normalizing them so that they agree in the limit where u and θ are close to zero. We find that these functions nearly overlap for the entire allowed range $0 < u \leq \frac{1}{2}$ (or $0 < \theta \leq \pi$) for various lattice aspect ratios $b_y \equiv b \leq 1$, and that the overlap becomes stronger as b decreases from 1. The agreement between these functions suggests a connection between different geometries in the underlying theory describing the system's critical behaviour, although an analytical explanation for this agreement remains an open question for future work.

2.5.1 Entanglement entropy in one spatial dimension

For a (1+1)-dimensional critical system with periodic boundary conditions and length $L_x = L$, the Rényi entanglement entropies are known to scale such that [14, 15, 16, 17, 18, 19]

$$S_\alpha^{d=1} = \frac{c}{6}\left(1 + \frac{1}{\alpha}\right)\ln\left[\frac{L}{\pi}\sin(\pi u)\right] + c', \tag{2.72}$$

where c is the universal central charge of the underlying conformal field theory and c' is a non-universal constant. For non-interacting scalar fields in one spatial dimension, the central charge is given by $c = 1$.

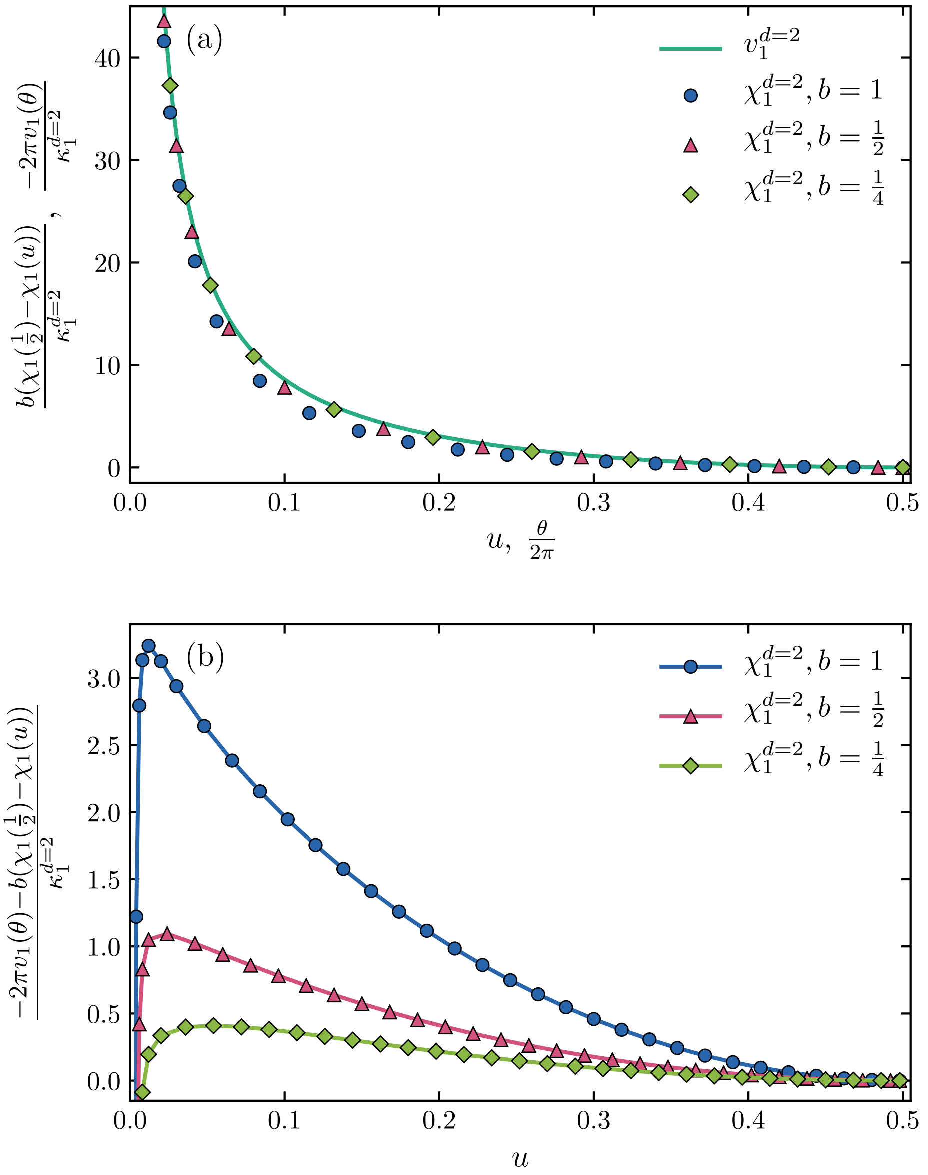

Figure 2.9: The universal two-cylinder function χ_1 compared with the universal corner coefficient v_1 in two spatial dimensions. For the cylinder, we consider various lattice aspect ratios $b_y \equiv b$. In (a), we show that the (appropriately normalized) two-cylinder function has a similar functional form to the corner coefficient for $b \leq 1$. In (b), we show that the difference between these two functions becomes smaller as b decreases. The data for $v_1(\theta)$ and the value for $\kappa_\alpha^{d=2}$ are from Reference [32].

Comparing with Equation (2.67), we find that the corresponding correction χ_α is given by

$$\chi_\alpha^{d=1}(u) = c_\alpha \, \ln\left[\sin(\pi u)\right] + \gamma_\alpha^{d=1}, \tag{2.73}$$

where $\gamma_\alpha^{d=1}$ is a u-independent constant and $c_\alpha \equiv c/6(1 + 1/\alpha)$.

For the case of $(1+1)$-dimensional non-interacting scalar fields, we can use the techniques outlined in Sections 2.1 and 2.2 to calculate the Rényi entanglement entropies $S_\alpha^{d=1}$. In Figure 2.10, we plot results for $S_\alpha^{d=1}$ as a function of the size of region A as well as fits to Equation (2.72) for the case where the lattice has PBC and APBC. For PBC, we observe that the Rényi entanglement entropies scale roughly linearly when plotted as a function of $\log\left[L/\pi \sin\left(\pi u\right)\right]$, as expected from Equation (2.72). However, for APBC, the form given in Equation (2.72) provides a lower-quality fit to the data. Although these fits appear to describe the data relatively well when plotted as a function of u, we observe significant discrepancies when the results are plotted a function of $\log\left[L/\pi \sin\left(\pi u\right)\right]$.

In order to reduce the number of fitting parameters from two to one, we now perform least-squares fits of $S_\alpha^{d=1}(1/2) - S_\alpha^{d=1}(u)$ to the form $\chi_\alpha^{d=1}(1/2) - \chi_\alpha^{d=1}(u)$ such that c_α becomes the sole fitting parameter. In order to study more qualitatively the difference between PBC and APBC in $1+1$ dimensions, we also introduce a measure of the fitting error similar to Equation (2.66) given by

$$\Delta_\alpha = \frac{1}{n_u - n_p - 1} \sum_{i=1}^{n_u} \Big(\left[\chi_\alpha(1/2) - \chi_\alpha(u_i)\right] - \left[S_\alpha(1/2) - S_\alpha(u_i)\right] \Big)^2, \tag{2.74}$$

where $S_\alpha(u_i)$ are the values of the numerical data, χ_α is the function used in the fit (Equation (2.73) in this case), n_u is the number of data points used in the fit and n_p is the number of fitting parameters. The integer $n_u - n_p - 1$ corresponds to the number of degrees of freedom. For simplicity, we have suppressed here the functional dependence on the aspect ratios $b_2, b_3, \ldots, b_d$.

In doing many of the fitting procedures in this and upcoming sections, we find that the errors are especially sensitive to the data points at small u. In particular, if the fitting procedure uses all $L/2$ available unique data points, then the errors often appear to diverge as the lattice size L increases. However, this divergence can be attributed to the fact that the resolution of a lattice scales according to $\Delta u = 1/L$, and thus larger lattices are capable of probing smaller values of u. Since these small-u effects are not what we wish to measure, we perform our fits using a resolution Δu and corresponding number of data points $n_u = 1/(2\Delta u)$ that remain fixed as the lattice size L increases. Such a constraint limits the lattice sizes on which we perform our fits to multiples of $1/\Delta u$.

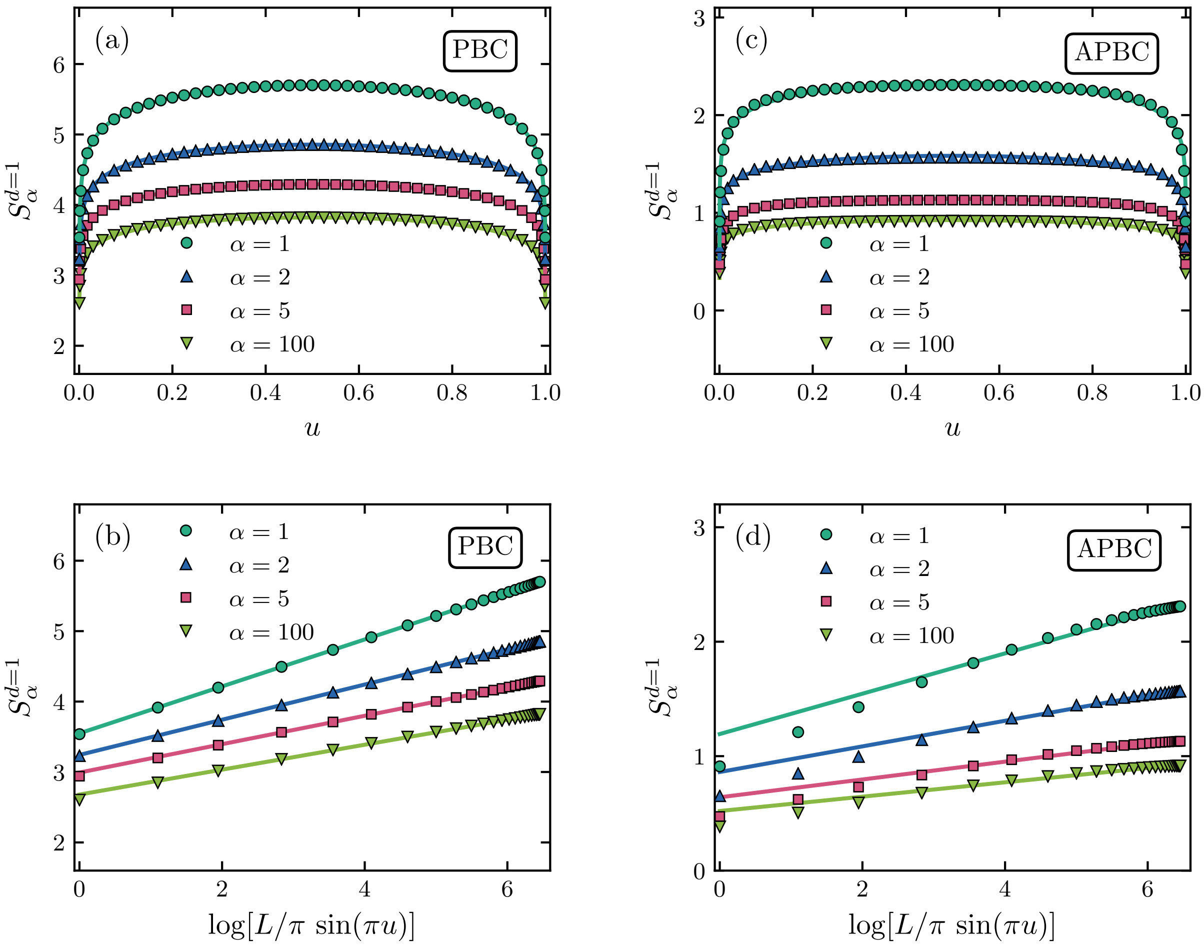

Figure 2.10: Rényi entanglement entropies in $1+1$ dimensions as a function of the length of region A for free scalar fields on a lattice with $L = 2000$. The points correspond to numerical results for various Rényi indicies α and the solid curves are two-parameter fits to Equation (2.72). In (a) and (b), we plot data for PBC, while in (c) and (d) we consider APBC. In each case, we show results as a function of $u \equiv L_A/L$ and also as a function of $\log\left[L/\pi \sin\left(\pi u\right)\right]$. For the periodic case, we set $m = 10^{-6}$ as explained in Section 2.1.2.

We plot in Figure 2.11 the fitting errors from Equation (2.74) corresponding to the Rényi entanglement entropies for various values of α. We find that, as expected, these errors trend to zero as $L \to \infty$ for PBC. However, for APBC, the fitting errors do not approach zero in the thermodynamic limit. A new analytic form for $\chi_\alpha^{d=1}(u)$ in the presence of antiperiodic or more general twisted boundary conditions was recently suggested in Reference [48].

2.5.2 Candidate functions for cylinders in two spatial dimensions

We consider now the case of the two-cylinder entropy for non-interacting bosonic fields in two spatial dimensions, with the goal of gaining insight into the universal function $\chi_\alpha^{d=2}(b,u)$, where $b \equiv b_y = L_x/L_y$. Unlike the one-dimensional case, here there is no known analytical expression for this function in the thermodynamic limit. However, below we discuss several candidate functional forms for $\chi_\alpha^{d=2}(b,u)$ based on various ansatzes (although none of these are expected to be exact in the thermodynamic limit).

Previous work suggested that the known one-dimensional function $\chi_\alpha^{d=1}(u)$ in Equation (2.72) may also apply in two spatial dimensions [49]. However, in the results that follow, we show that although this one-dimensional function has some of the same qualitative features as $\chi_\alpha^{d=2}(b,u)$, it fails to completely characterize our two-dimensional data in the thermodynamic limit. In particular, this functional form does not obey the thin-cylinder limit of Equation (2.71).

Another candidate functional form was proposed by Stéphen, Ju, Fendley and Melko in the context of studying the Quantum Lifshitz model (QLM) [50]. In this case, the functional form for the two-cylinder universal function is given by

$$\chi_{\alpha,\mathrm{QLM}}(b,u) = \frac{24\,\kappa_\alpha^{d=2}}{\pi}\ln\left[\frac{\eta(2ibu)\,\eta(2ib(1-u))}{\theta_3(ib\lambda u)\,\theta_3(ib\lambda(1-u))}\right] + \gamma_{\alpha,\mathrm{QLM}}, \tag{2.75}$$

where $\gamma_{\alpha,\mathrm{QLM}}$ is a constant (independent of b and u), $\theta_3(\tau) \equiv \theta_3(0,\tau)$ is the Jacobi theta function, $\eta(\tau) = \theta_2(\pi/6,\tau/6)/\sqrt{3}$ is the Dedekind eta function and λ is a model-dependent parameter. We fix $\lambda = 2$ in the following, although in principle this parameter can take other values. This function has been normalized [35] so that it reduces to Equation (2.71) in the thin-cylinder limit.

In Reference [35], Chen, Cho, Faulkner and Fradkin use the AdS/CFT correspondence to derive another candidate functional form for $\chi_\alpha^{d=2}(b,u)$. For lattice aspect ratios $b \leq 1$,

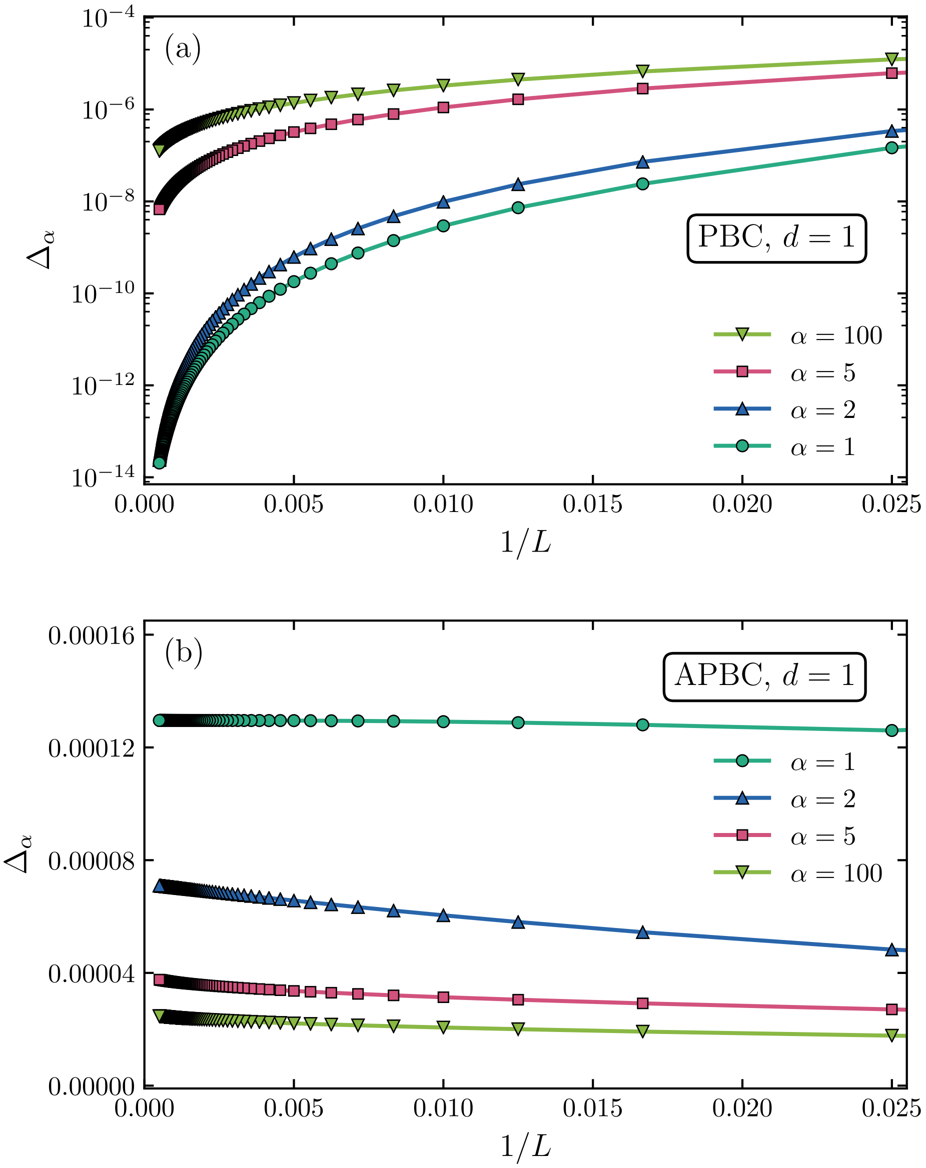

Figure 2.11: The fitting errors corresponding to one-parameter fits of the $(1 + 1)$-dimensional Rényi entanglement entropies to the expression in Equation (2.73) for (a) PBC and (b) APBC. We observe that this expression is exact in the thermodynamic limit (*i.e.* the errors trend to zero) for PBC but not for APBC. These errors are measured using resolution $\Delta u = 0.05$ on lattices of size $L = 40, 60, \ldots, 2000$. We set $m = 10^{-6}$ for PBC and $m = 0$ for APBC. Note the logarithmic scale on the y-axis in (a).

this derivation gives

$$\chi_{\alpha,\mathrm{AdS}}(b,\omega) = \frac{\kappa_\alpha^{d=2}\,\Gamma^4\left(\frac{1}{4}\right)}{3\pi^2 b}\,\omega^{-1/3}\left[\int_0^1 \frac{d\zeta}{\zeta^2}\left(\frac{1}{\sqrt{P(\omega,\zeta)}}-1\right)-1\right]+\gamma_{\alpha,\mathrm{AdS}} \qquad (\text{for } b \leq 1), \tag{2.76}$$

where $\gamma_{\alpha,\mathrm{AdS}}$ is a constant, $\Gamma(x)$ is the gamma function and $P(\omega,\zeta) = 1-\omega\zeta^3-(1-\omega)\zeta^4$. The parameter ω is related to u through the integral

$$u(\omega) = \frac{3\omega^{1/3}(1-\omega)^{1/2}}{2\pi}\int_0^1 \frac{d\zeta\zeta^2}{(1-\omega\zeta^3)}\frac{1}{\sqrt{P(\omega,\zeta)}}. \tag{2.77}$$

A final candidate form for $\chi_\alpha^{d=2}(b,u)$ comes from the extensive mutual information (EMI) model [51, 52, 12], which has been used in previous works to gain insight into entanglement scaling behaviour in various dimensions [53, 54]. Recently, it was shown for the case of two cylinders on a torus that the EMI model predicts [27]

$$\chi_{\alpha,\mathrm{EMI}}(b,u) = \frac{-2\kappa_\alpha}{\pi b}\left[\frac{\operatorname{arccot}(2bu)}{u}+\frac{\operatorname{arccot}(2b(1-u))}{1-u}\right]+\gamma_{\alpha,\mathrm{EMI}}, \tag{2.78}$$

where $\gamma_{\alpha,\mathrm{EMI}}$ is a constant.

Here, we focus on studying the dependence of $\chi_\alpha^{d=2}$ on u for lattice aspect ratio $b=1$. As in Section 2.5.1, we calculate $S_\alpha^{d=2}(1/2) - S_\alpha^{d=2}(u)$ so as to cancel both the area-law contribution to the entanglement entropy as well as the b- and u-independent universal constant γ_α (which has been studied in Reference [37]). In Figure 2.12, we show the results of these least-squares fits for $\alpha = 1$ as well as the amount that each fit deviates from the numerical data. It is immediately clear that the one-dimensional function of Equation (2.72) provides a poor characterization of that data.

We proceed to study the quality of these fits for $\chi_\alpha^{d=2}$ as a function of system size L, with the goal of understanding the functional behaviour of the two-cylinder entanglement entropy in the thermodynamic limit. We calculate the fitting errors as in Equation (2.74) for each of the four candidate functional forms and display our results in Figure 2.13.

We find that the behaviour of the finite-size scaling trends depend both upon the chosen resolution Δu and upon the lattice boundary conditions. PBC along the x-direction and APBC along the y-direction are used to generate the plots presented in Figures 2.12 and 2.11. Table 2.1 summarizes the fitting errors measured using resolution $\Delta u = 0.05$ for

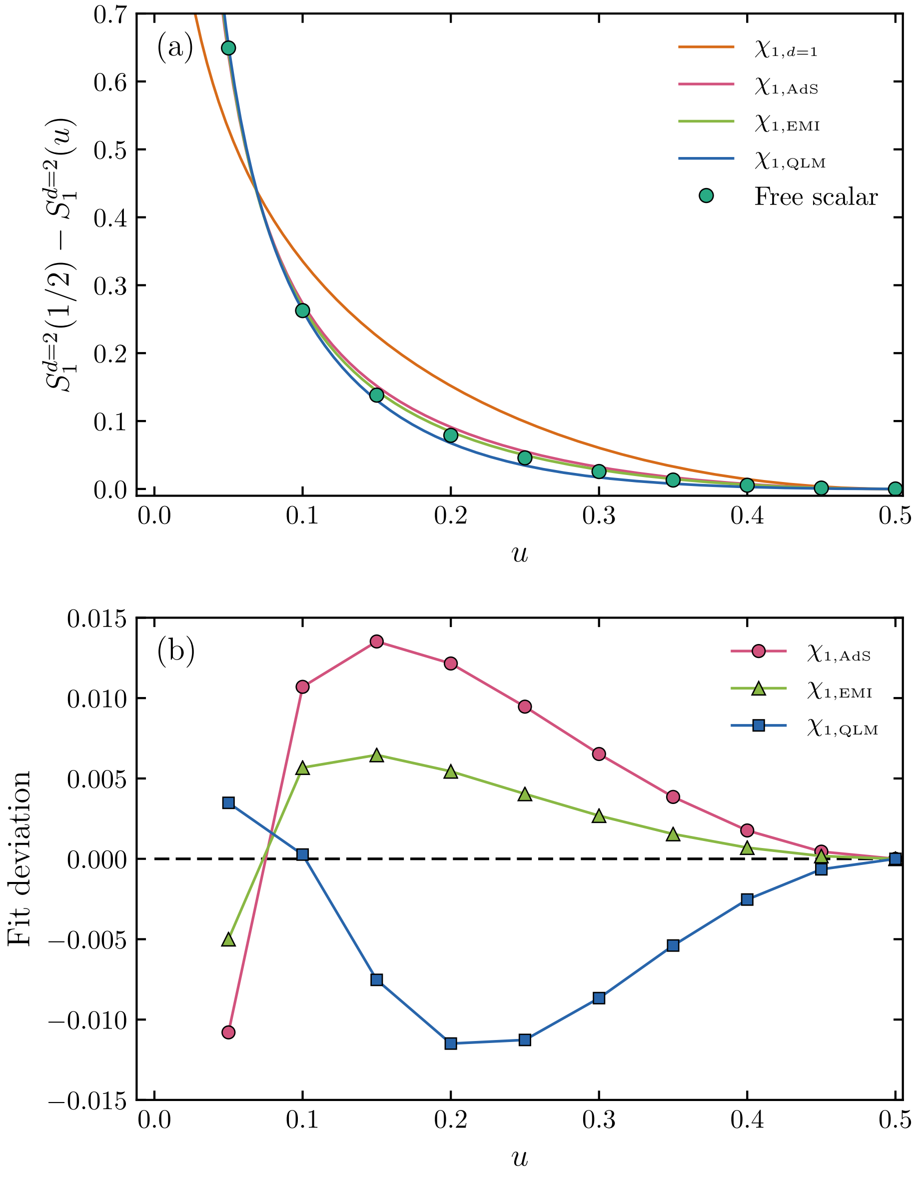

Figure 2.12: Fits of the von Neumann entanglement entropy to the four candidate functions for $\chi_\alpha(b, u)$ discussed in Equations (2.73), (2.78), (2.75) and (2.76) (each with $b = 1$ and resolution $\Delta u = 0.05$). The data points come from an $L = 3000$ free scalar system with PBC along the x-direction and APBC along the y-direction. In (a), we show the shape dependence of the data points and the fits. In (b), we illustrate the amount that each fit deviates from each data point. The fit deviation for $\chi_{1,d=1}$ is excluded since it is much larger in magnitude than the other three curves.

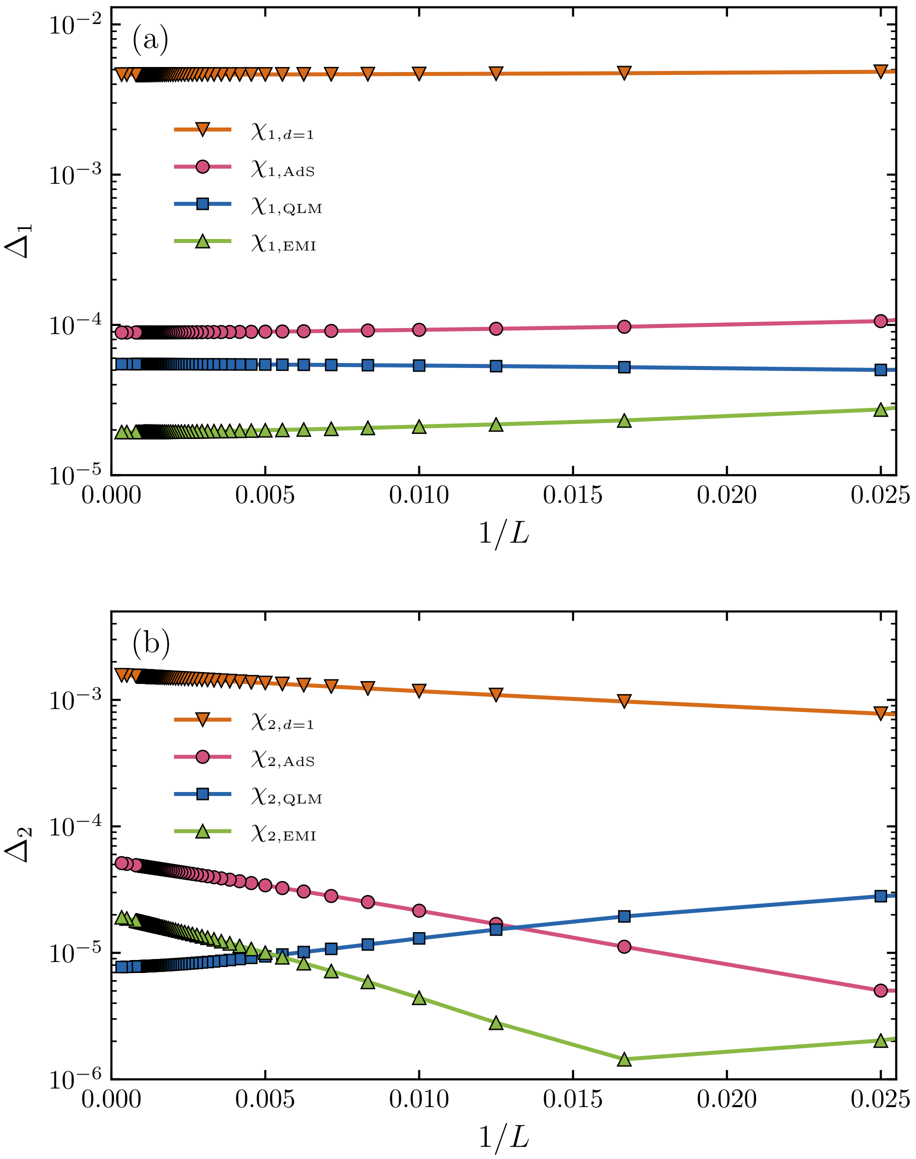

Figure 2.13: The fitting errors corresponding to the four candidate functions for γ_α as a function of $1/L$ for the 2D free boson (a) von Neumann and (b) second Rényi entropies. Both plots have PBC along the x direction and APBC along the y direction. The errors are measured using resolution $\Delta u = 0.05$ on lattices of linear size $L = 40$ up to 3000.

Fitting error	x-direction	y-direction	$d=1$	QLM	AdS	EMI
Δ_1	PBC	PBC	3.18×10^{-3}	4.13×10^{-3}	1.56×10^{-3}	2.25×10^{-3}
	PBC	APBC	4.63×10^{-3}	5.49×10^{-5}	8.90×10^{-5}	1.94×10^{-5}
	APBC	PBC	4.60×10^{-3}	4.24×10^{-5}	1.12×10^{-4}	3.27×10^{-5}
	APBC	APBC	5.05×10^{-3}	2.85×10^{-5}	3.10×10^{-4}	1.69×10^{-4}
Δ_2	PBC	PBC	9.28×10^{-4}	2.61×10^{-3}	1.19×10^{-3}	1.59×10^{-3}
	PBC	APBC	1.56×10^{-3}	7.73×10^{-6}	5.12×10^{-5}	1.91×10^{-5}
	APBC	PBC	1.51×10^{-3}	9.94×10^{-6}	4.68×10^{-5}	1.70×10^{-5}
	APBC	APBC	1.67×10^{-3}	2.06×10^{-5}	1.35×10^{-4}	8.28×10^{-5}

Table 2.1: The fitting errors corresponding to the four candidate functions for the two-cylinder correction χ_α to the area law in $2+1$ dimensions [29]. Results are displayed for the von Neumann and second Rényi entropies and for different boundary conditions The errors in this table are measured using resolution $\Delta u = 0.05$ on a square lattice of size $L = 3000$. Calculations for the fully periodic system include a small mass $m = 10^{-6}$ as explained in Section 2.1.2.

various boundary conditions. For the von Neumann entropy S_1, the functions χ_{QLM} and χ_{EMI} consistently yield the lowest fitting errors out of the four candidate functions, once at least one boundary is antiperiodic. For the case of periodic boundary conditions in both directions, the fitting errors for χ_{QLM}, χ_{EMI} and χ_{AdS} all become much larger, while for $\chi_{d=1}$ these errors change only slightly and no longer correspond to the worst fit. In the case of the second Rényi entropy, the errors corresponding to γ_{QLM} are consistently lowest, except (again) for the case of PBC in both directions.

In addition to exploring the most suitable functional form for $\chi_\alpha^{d=2}(u)$ for $\alpha = 1$ and 2, we also examine the ability of our fits to extract the universal number $\kappa_\alpha^{d=2}$, which was defined from the thin-cylinder limit in Equation (2.71). For $(2+1)$-dimensional massless real free bosons in the continuum, this coefficient κ_1 has been calculated numerically for the von Neumann entropy [32] to be $\kappa_1^{d=2} = 0.0397$ as well as for the second Rényi entropy [54] to be $\kappa_2^{d=2} = 0.0227998$. On a lattice, one can calculate $\kappa_\alpha^{d=2}$ by fitting to $\chi_\alpha^{d=2}(u \to 0)$ in Equation (2.71) for small u. Here we use a slightly different procedure than the fixed-resolution approach used to fit the four candidate functions: for a given lattice of size $L \geq 80$, we extract $\kappa_\alpha^{d=2}$ in the $u \to 0$ limit from our free boson calculations by fitting $S_\alpha^{d=2}(40/L) - S_\alpha^{d=2}(u)$ to Equation (2.71) for $u = 31/L, 32/L, \ldots, 40/L$ (we ignore the smallest 30 values of u due to numerical issues that arise when the cylinder becomes very thin). Results are illustrated in Figure 2.14.

The QLM, AdS and EMI functions all obey the known thin-cylinder behaviour of Equation (2.71) in the small-u limit, allowing for predictions of the universal number $\kappa_\alpha^{d=2}$ from each. In Figure 2.14 we illustrate the $\kappa_1^{d=2}$ and $\kappa_2^{d=2}$ coefficients as predicted from fits (for the entire range of u values and with fitting resolution $\Delta u = 0.05$) to χ_{QLM}, χ_{AdS} and χ_{EMI}. Although we know from the fitting errors that none of these three candidate functions are exact in the thermodynamic limit, they are all still capable of extracting estimates for $\kappa_\alpha^{d=2}$ that agree relatively well with the previously-calculated continuum values [32, 54] and the lattice values from fits to Equation (2.71). In particular, χ_{QLM} and χ_{EMI} both yield estimates for $\kappa_1^{d=2}$ ($\kappa_2^{d=2}$) that are within less than 5% (9%) of the value calculated in Reference [32] (Reference [54]).

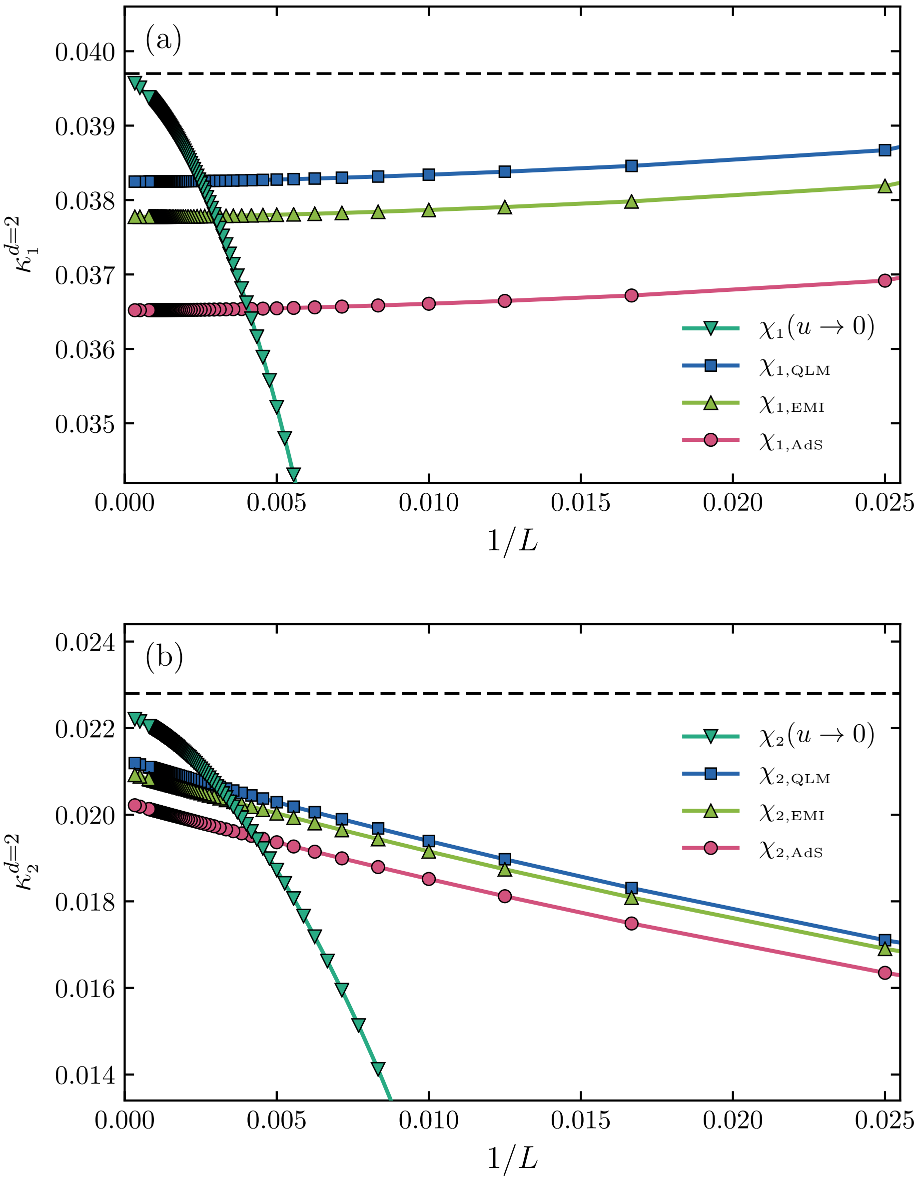

Figure 2.14: The universal number $\kappa_\alpha^{d=2}$ in two spatial dimensions for the (a) von Neumann and (b) second Rényi entropies, as extracted from fits to $\gamma_\alpha(u \to 0)$, γ_{QLM}, γ_{AdS} and γ_{EMI}. The dashed lines indicate the values calculated in the continuum in the $u \to 0$ limit [32, 54].

Chapter 3

Monte Carlo methods for classical interacting theories

This chapter includes results from the computational project for PHYS 705, as well as original results not published elsewhere.

Having established certain properties about the non-interacting limit of lattice field theories in Chapter 2, we now turn to more complicated interacting models such as the lattice models and field theories introduced in Section 1.1. We consider both the classical d-dimensional $O(N)$ model as well as closely-related symmetry-broken Hamiltonians. We thus add to the Hamiltonian of Equation (1.2) more general on-site (non-interacting) terms that depend on a set of site-dependent parameters $\{g_i\}$ such that

$$\begin{aligned} H &= -J\sum_{\langle ij\rangle}\mathbf{n}_i\cdot\mathbf{n}_j + \sum_i f\left(\{g_i\},\mathbf{n}_i\right) \\ H &= H_{O(N)} + H_{\mathrm{on-site}}, \end{aligned} \tag{3.1}$$

with

$$H_{\mathrm{on-site}} = \sum_i f\left(\{g_i\},\mathbf{n}_i\right), \tag{3.2}$$

where the function f can in general be an expansion in powers of the components of $\mathbf{n}_i$. For example, the parameters $\{g_i\}$ might represent a (site-dependent) applied magnetic field $\mathbf{B}_i$

such that $f(\{g_i\}, \mathbf{n}_i) = -\mathbf{B}_i \cdot \mathbf{n}_i$. As in Chapter 2, we focus our studies on hypercubic lattices with linear lengths $L_1, L_2, \ldots, L_d$ along each respective lattice direction.

3.1 Monte Carlo methods

The goal of a Monte Carlo simulation is to calculate the expectation value $\langle \mathcal{O} \rangle$ of some observable quantity $\mathcal{O}$. In a classical system, such an expectation value depends upon the Hamiltonian H according to

$$\langle \mathcal{O} \rangle = \frac{1}{\mathcal{Z}} \sum_{\text{states } \mu} \mathcal{O}_\mu e^{-E_\mu/T}, \tag{3.3}$$

where the sum is over all possible system states μ. $\mathcal{O}_\mu$ is the value of the observable in state μ and E_μ is the energy of state μ as calculated from the Hamiltonian. The symbol $\mathcal{Z}$ represents the partition function, which is given by

$$\mathcal{Z} = \sum_{\text{states } \mu} e^{-E_\mu/T}. \tag{3.4}$$

The probability of finding the system in a particular state μ can be expressed as

$$p_\mu = \frac{1}{\mathcal{Z}} e^{-E_\mu/T}, \tag{3.5}$$

such that the expectation value $\langle \mathcal{O} \rangle$ can be written as a weighted sum over the observables of each state μ as $\langle \mathcal{O} \rangle = \sum_\mu \mathcal{O}_\mu \, p_\mu$.

An exact evaluation of the sums in Equations (3.3) and (3.4) is only feasible for very small interacting systems due to the fact that the number of terms in these sums grows exponentially with the size of the system. For the Ising model, for example, evaluating such sums with an optimized algorithm for a system of 25 spins requires about a minute of CPU time [55], but the time required for 80 spins is longer than the age of the universe. Monte Carlo methods approximate these sums by considering the values of the observable quantity $\mathcal{O}$ that correspond to only M different states of the system at M different Monte Carlo "times" t. These M states are chosen at random but in a way that the probability of sampling a state μ is given by p_μ. The expectation value $\langle \mathcal{O} \rangle$ can then be approximated from [6]

$$\langle \mathcal{O} \rangle \approx \frac{1}{M} \sum_{t=1}^{M} \mathcal{O}_{\mu_t}. \tag{3.6}$$

Every Monte Carlo algorithm should be designed such that this approximation becomes exact in the limit $M \to \infty$.

Monte Carlo algorithms utilize Markovian processes to sample the M states μ_t in Equation (3.6). When in a sampled state μ_t, such processes randomly select the next state μ_{t+1} in the Markov chain with a transition probability $P(\mu_t \to \mu_{t+1})$ that depends only upon the state μ_t (and not upon any earlier states $\mu_{t-1}, \mu_{t-2}, \ldots$). Each Monte Carlo algorithm must sample the states μ_t in such a way that the corresponding probabilities p_{μ_t} of sampling a state are given by Equation (3.5). Such a constraint on the probabilities p_{μ_t} amounts to enforcing two conditions known as *ergodicity* and *detailed balance*.

The condition of ergodicity states that the probability of sampling a given state μ within a Monte Carlo algorithm must always be nonzero. Although many of the transition probabilities $P(\mu \to \nu)$ can be zero within a given algorithm, there must always exist a chain of states $\mu \to \mu' \to \mu'' \to \cdots \to \nu$ with nonzero transition probabilities $P(\mu \to \mu'), P(\mu' \to \mu''), \ldots$ for any pair of initial and final states μ and ν [6].

The detailed balance condition ensures that the overall probability of transitioning into a state μ_t is the same as the probability of transitioning out of the state μ_t such that [6]

$$\sum_{\mu_{t+1}} p_{\mu_t} P(\mu_t \to \mu_{t+1}) = \sum_{\mu_{t-1}} p_{\mu_{t-1}} P(\mu_{t-1} \to \mu_t), \tag{3.7}$$

which guarantees that the probability distribution p_μ does not change over time. Detailed balance is, in fact, a particular solution of Equation (3.7) given by

$$p_\mu P(\mu \to \nu) = p_\nu P(\nu \to \mu), \tag{3.8}$$

where μ and ν can be any two system states. Since we wish for the probability distribution p_μ to satisfy Equation (3.5), detailed balance therefore requires that the transition probabilities of a Monte Carlo sampling algorithm satisfy

$$\frac{P(\mu \to \nu)}{P(\nu \to \mu)} = e^{-(E_\nu - E_\mu)/T}. \tag{3.9}$$

In the sections that follow, we examine various Monte Carlo algorithms for sampling states of classical interacting Hamiltonians. We show that, although every algorithm we study satisfies the conditions of ergodicity and detailed balance, different algorithms may have different sampling efficiencies such that the number of samples M required to obtain a converged estimate of $\langle \mathcal{O} \rangle$ may vary drastically.

3.1.1 Local updates

The first Monte Carlo sampling algorithm was proposed and studied by Metropolis, Rosenbluth, Rosenbluth, Teller and Teller in 1953 [56] and by Hastings in 1970 [57]. This algorithm is based on local changes to a system's state μ such that the difference between the current state and the proposed state only differ at a single lattice site i, which is selected at random.

For the Hamiltonian of Equation (3.1), this algorithm works by selecting a site i at random and proposing the change $\mathbf{n}_i \to \mathbf{n}_{\text{new}}$, where the orientation of the vector $\mathbf{n}_{\text{new}}$ is selected at random. (Methods for selecting such N-dimensional unit vectors at random are discussed in Section 3.2.) The energy change corresponding to this move is given by [6]

$$\begin{aligned} \Delta E &= -J \sum_{\text{n.n. } j \text{ of } i} \left(\mathbf{n}_{\text{new}} \cdot \mathbf{n}_j - \mathbf{n}_i \cdot \mathbf{n}_j \right) + \big[f\left(\{g_i\}, \mathbf{n}_{\text{new}}\right) - f\left(\{g_i\}, \mathbf{n}_i\right) \big] \\ &= J \left(\mathbf{n}_i - \mathbf{n}_{\text{new}} \right) \cdot \sum_{\text{n.n. } j \text{ of } i} \mathbf{n}_j + \big[f\left(\{g_i\}, \mathbf{n}_{\text{new}}\right) - f\left(\{g_i\}, \mathbf{n}_i\right) \big]. \end{aligned} \tag{3.10}$$

There are various possible choices for the transition probabilities $P(\mathbf{n}_i \to \mathbf{n}_{\text{new}})$ that satisfy the condition of detailed balance, but the optimal strategy is to set

$$P(\mathbf{n}_i \to \mathbf{n}_{\text{new}}) = \begin{cases} e^{-\Delta E/T} & \text{if } \Delta E > 0 \\ 1 & \text{otherwise.} \end{cases} \tag{3.11}$$

The procedure for performing a local Monte Carlo update is given in Algorithm 3.1. The steps of this algorithm must be executed many times in order to obtain independent sample configurations. The M different configurations used to calculate $\langle \mathcal{O} \rangle$ in Equation (3.6) should be sufficiently spaced in Monte Carlo time so that each state μ_t in the sum is uncorrelated with the previous state μ_{t-1}.

Algorithm 3.1: Metropolis-Hastings algorithm applied to the nearest-neighbour interacting Hamiltonian with on-site energy terms of Equation (3.1) [56, 57, 6]. This algorithm describes a local (single-spin) Monte Carlo update and must be executed several times in order to obtain uncorrelated system configurations.

```
choose a site $i$ from the lattice at random;
choose a random new orientation $\mathbf{n}_{\text{new}}$ for the spin at this location;
calculate the energy difference $\Delta E$ associated with changing the
  current spin orientation $\mathbf{n}_i$ to $\mathbf{n}_{\text{new}}$ using Equation (3.10);
if $\Delta E \leq 0$ then
    accept the move $\mathbf{n}_i \rightarrow \mathbf{n}_{\text{new}}$;
else
    accept the move $\mathbf{n}_i \rightarrow \mathbf{n}_{\text{new}}$ with probability $\exp(-\Delta E/T)$;
end
```

In principle, this algorithm satisfies the condition of ergodicity at any finite temperature since there is always a nonzero probability of selecting any site i and changing the vector $\mathbf{n}_i$ to any desired configuration. However, at temperatures near a critical point T_c, large fluctuations in observables can lead to a feature known as critical slowing down, whereby the Monte Carlo time required to obtain independent sample configurations diverges with system size. At low temperatures, this algorithm can be get stuck in local energy minima such that every path in configuration space to the global energy minimum requires a temporary increase in energy, which becomes highly improbable at low temperatures. Therefore, in practice this algorithm can be nonergodic for the timescales used in a typical simulation.

3.1.2 Cluster updates

In order to combat the issues of practical nonergodicity that can result from using only local Monte Carlo updates, new Monte Carlo algorithms were introduced by Swendsen and Wang in 1987 [58] and by Wolff in 1989 [59]. Both of these algorithms probabilistically generate clusters of spins and then collectively update the spins within the clusters. Here,

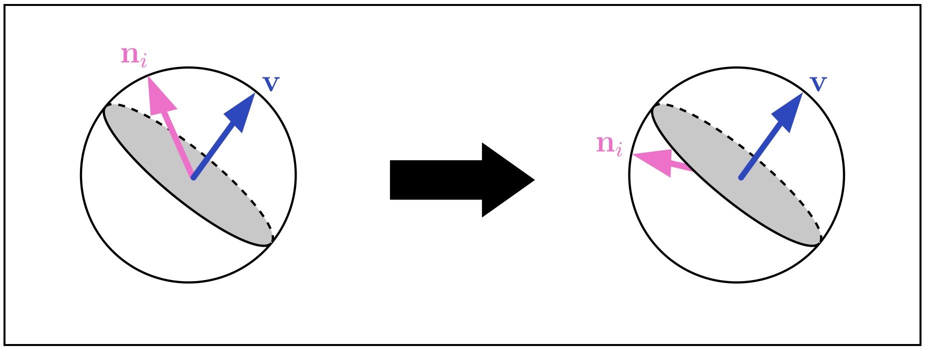

Figure 3.1: Illustration of the spin update procedure within the Monte Carlo Wolff cluster algorithm [59]. After a cluster has been generated, all spins within the cluster are reflected about the hyperplane orthogonal to the vector $\mathbf{v}$ with a probability that depends upon the cluster's change in on-site energy.

we focus on the algorithm by Wolff since it is be utilized in the sections that follow as well as in Chapter 4.

Within the Wolff algorithm, an N-dimensional unit vector $\mathbf{v}$ is chosen at random and spins with the same sign of projection onto $\mathbf{v}$ are added to a cluster with a probability that depends upon the nearest-neighbour coupling energy. The original Wolff algorithm was designed for a Hamiltonian with no on-site energy term such that $H = H_{\text{n.n.}}$. In this case, the group of spins that results from the iterative cluster-building procedure are all reflected about the hyperplane orthogonal to the vector $\mathbf{v}$, as illustrated in Figure 3.1.

In the presence of an on-site term $H_{\text{on-site}}$ in the Hamiltonian, the Wolff cluster algorithm can be modified slightly in order to incorporate a cluster acceptance probability given by [6, 60]

$$\begin{aligned} P_{\text{accept}} &= \min\left\{1, \exp\left(-\Delta E_{\text{on-site}}/T\right)\right\} \\ &= \min\left\{1, \exp\left[-\frac{1}{T}\sum_{i\in\text{cluster}} f\left(\{g_i\}, R(\mathbf{v})\mathbf{n}_i\right) - f\left(\{g_i\}, \mathbf{n}_i\right)\right]\right\}, \end{aligned} \tag{3.12}$$

such that the cluster built within the original algorithm is only accepted and flipped with probability P_{accept}. A summary of the steps corresponding to a Wolff update for a Hamiltonian of the general form in Equation (3.1) is given in Algorithm 3.2.

Algorithm 3.2: Wolff cluster algorithm for non-local Monte Carlo updates for the $O(N)$ model of Equation (3.1) [59, 6]. A cluster of spins is generated probabilistically based on the nearest-neighbour interaction energy and then the corresponding update is either accepted or rejected with a probability that depends upon Hamiltonian's on-site energy.

```
choose a random $N$-dimensional unit vector $\mathbf{v}$;
create an empty cluster and an empty buffer;
choose a site $i$ from the lattice at random;
add site $i$ to the cluster and to the buffer;
while buffer is not empty do
    pop site $i$ off the buffer;
    for each n.n. $j$ of $i$ that is not already in the cluster do
        add site $j$ to the cluster and to the buffer with probability
        $1 - \exp\{\min[0, -2(J/T)(\mathbf{v}\cdot\mathbf{n}_i)(\mathbf{v}\cdot\mathbf{n}_j)]\}$;
    end
end
calculate $P_{\text{accept}}$ from Equation (3.12);
with probability $P_{\text{accept}}$ do
    //reflect all spins in the cluster:
    for each site $i$ in the cluster do
        reflect $\mathbf{n}_i$ about the hyperplane orthogonal to $\mathbf{v}$ such that
        $\mathbf{n}_i \to R(\mathbf{v})\mathbf{n}_i = \mathbf{n}_i - 2(\mathbf{v}\cdot\mathbf{n}_i)\mathbf{v}$;
    end
end
```

3.2 Random points on hyperspheres

The local and global Monte Carlo updates described in Sec. 3.1 all rely on an algorithm capable of generating pseudorandom N-component unit vectors $\mathbf{n}$. One can think of these unit vectors as starting at the origin and ending on the surface of a unit hypersphere embedded in N dimensions. Such a hypersphere is known as an $(N-1)$-sphere.

One can parametrize the surface a hypersphere in terms of hyperspherical angular coordinates $\theta_1, \theta_2, \dots \theta_{N-1}$, where $\theta_i \in [0, \pi]$ for $i = 1, 2, \dots N-2$ and $\theta_{N-1} \in [0, 2\pi)$. The Cartesian components are given in terms of these angular coordinates as

$$\begin{aligned}
n_1 &= \cos(\theta_1) \\
n_2 &= \sin(\theta_1)\cos(\theta_2) \\
n_3 &= \sin(\theta_1)\sin(\theta_2)\cos(\theta_3) \\
&\vdots \\
n_{N-1} &= \sin(\theta_1)\cdots\sin(\theta_{N-2})\cos(\theta_{N-1}) \\
n_N &= \sin(\theta_1)\cdots\sin(\theta_{N-2})\sin(\theta_{N-1}).
\end{aligned} \tag{3.13}$$

One might think that it is possible to generate random points that are uniformly distributed on the surface of a hypersphere by choosing the angles $\theta_1, \theta_2, \dots \theta_{N-1}$ from uniform distributions. Such an approach works when $N = 2$, where choosing the angle θ_1 from a uniform distribution with $\theta_1 \in [0, 2\pi)$ indeed produces points that are uniformly distributed on the surface of a 2-sphere (circle). However, this approach fails for $N \geq 3$. For $N = 3$, for example, selecting the angles θ_1 and θ_2 from uniform distributions produces points on the hypersphere that are more dense near the poles (where $\theta_1 = 0$ or π) and more sparse near the equator (where $\theta_1 = \frac{\pi}{2}$), as illustrated in Fig. 3.2a.

There are several methods available for choosing points uniformly from the surface of a hypersphere [61, 62, 63, 64, 65, 66]. In $N = 3$, these methods generate a distribution such as the one illustrated in Fig. 3.2b. Two common algorithms that work for all $N \geq 2$ are the rejection method and the Gaussian method.

The rejection method (Algorithm 3.3) repeatedly generates N independent Cartesian coordinates from a uniform distribution until it finds a point inside the unit hypersphere. It then projects such a point to the surface of the hypersphere. This method becomes infeasible as N increases because it must call a (uniform) random number generator an average of

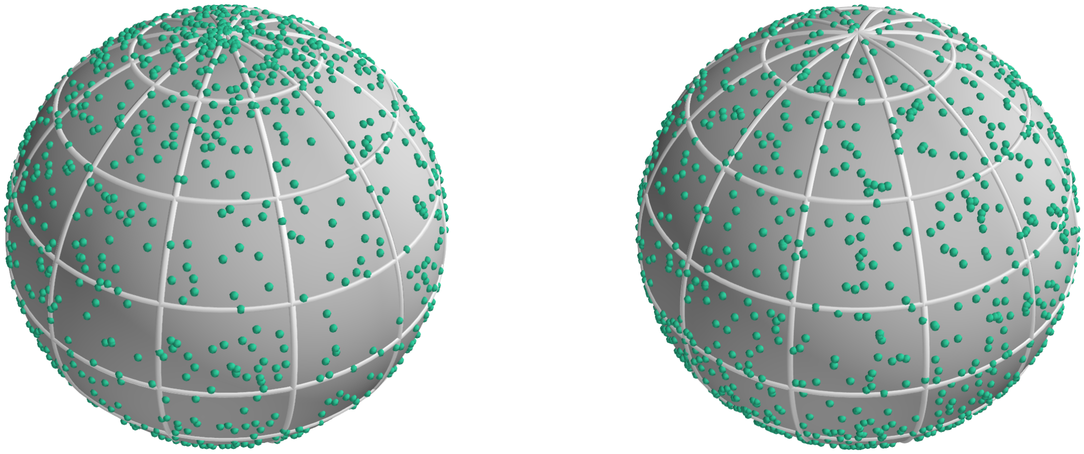

(a)

(b)

Figure 3.2: Points chosen at random on the surface of a sphere ($N = 3$). In (a), the spherical coordinates θ_1 and θ_2 are chosen from uniform distributions, which results in non-uniform "clustering" near the poles. In (b), the points are chosen to be uniformly distributed on the surface of the sphere by using an algorithm such as Algorithm 3.3 or 3.4.

$NV_{\text{hypercube}}/V_{\text{hypersphere}}$ times, where $V_{\text{hypercube}} = 2^N$ is the volume of the hypercube inside of which each generated point lies and $V_{\text{hypersphere}} = \pi^{N/2}/\Gamma\left(\frac{N}{2}+1\right)$ is the volume of the hypersphere inside of which accepted points must lie. This number of required random numbers thus grows rapidly (faster than exponentially) as N increases.

Alternatively, the Gaussian method (Algorithm 3.4) requires that N numbers be selected from a Gaussian (normal) distribution, which can be accomplished by using uniformly-distributed random numbers in conjunction with an algorithm such as the Box-Muller transformation [67]. Although the process of choosing from a Gaussian distribution is significantly slower than choosing from a uniform distribution, the Gaussian method is still most efficient for $N \gtrapprox 2$ or 3 since it requires far fewer random numbers than the rejection method.

Algorithm 3.3: Rejection method for choosing points on the surface of a unit hypersphere in N-dimensional space, where $N \geq 2$ [65]. This method generates points within a hypercube with linear length 2 until it finds a point inside the boundary of the unit hypersphere. It then projects this point to the surface of the hypersphere.

```
initialize $S$ to any value greater than 1;
while $S < 1$ do
    choose $n_1, n_2, \ldots, n_N$ from a uniform distribution with $n_i \in (-1, 1)$;
    set $S = \sum_{i=1}^{N} n_i^2$;
end
return $(n_1/\sqrt{S}, n_2/\sqrt{S}, \ldots, n_N/\sqrt{S})$;
```

Algorithm 3.4: Gaussian method for choosing points on the surface of a unit hypersphere in N-dimensional space, where $N \geq 2$ [63, 65]. This method independently generates N Cartesian coordinates from a (hyperspherically-symmetric) Gaussian distribution with mean 0 (and any finite variance). It then projects the resulting point to the surface of the hypersphere.

```
choose $n_1, n_2, \ldots, n_N$ from a Gaussian distribution with mean 0;
set $S = \sum_{i=1}^{N} n_i^2$;
return $(n_1/\sqrt{S}, n_2/\sqrt{S}, \ldots, n_N/\sqrt{S})$;
```

3.3 Critical exponents for the $O(4)$ model in three spatial dimensions

We now put the methods introduced in the previous sections into practice by utilizing Monte Carlo simulation in order to extract observables and critical exponents corresponding to the $O(4)$ model. Such critical exponents have been calculated previously [68], and we thus use these calculations as a means of establishing the validity of the Monte Carlo methods introduced in Sections 3.1 and 3.2. We then proceed to explore new, unstudied models in Chapter 4.

We consider the Hamiltonian of Equation (1.2) (with no on-site energy term) with $N = 4$ and in $d = 3$ spatial dimensions. This model is known to have a critical temperature given by [69]

$$T_c/J = 1.06835(13). \tag{3.14}$$

A conventional order parameter m for the $O(N)$ model of Equation (1.2) is the magnetization per spin, which is defined in terms of the vectorial magnetization per spin $\mathbf{m}$ as

$$\begin{aligned} m &= \left\langle \sqrt{\mathbf{m} \cdot \mathbf{m}} \right\rangle, \\ \mathbf{m} &= \frac{1}{L^d} \sum_i \mathbf{n}_i. \end{aligned} \tag{3.15}$$

However, one can also study the critical exponents associated with a different order parameter m_T which is expressed in terms of the tensorial magnetization per spin $\mathcal{M}_{\alpha\beta}$ as [68]

$$\begin{aligned} \mathcal{M}_{\alpha\beta} &= \frac{1}{L^3} \sum_i \left[n_{i\alpha} n_{i\beta} - \frac{1}{4} \delta_{\alpha\beta} \right], \\ m_T &= \left\langle \sqrt{\mathrm{Tr}\left(\mathcal{M}^2\right)} \right\rangle, \end{aligned} \tag{3.16}$$

where $n_{i\alpha}$ are the components of $\mathbf{n}_i$, with $\alpha, \beta = 1, 2, 3, 4$.

Recall the critical exponents as defined in Section 1.3. While the exponents α and ν can be calculated without requiring definition of an order parameter, the exponents β, γ and η in general depend upon how the order is defined [68]. We therefore adopt the notation whereby we use a subscript T to denote the critical exponents that specifically correspond to the tensorial magnetization. Based on the hyperscaling relations of Equation (1.25), we note that in $d = 3$ the anomalous dimension η_T can be expressed in terms of other critical exponents as

$$\eta_T = \frac{2\beta_T}{\nu} - 1, \tag{3.17}$$

or

$$\eta_T = 2 - \frac{\gamma_T}{\nu}. \tag{3.18}$$

Exactly at the critical point T_c, we know from Equation (1.29) that the order parameter on a finite size lattice with $L_x = L_y = L_z \equiv L$ is expected to scale with the system size such that

$$m_T(t = 0) \sim L^{-\beta_T/\nu}. \tag{3.19}$$

Therefore, when the system is critical, we expect that the slope of $\log(m_T)$ versus $\log L$ should give an estimate for β_T/ν, which can in turn be used to estimate η_T through Equation (3.17).

Similarly, the tensorial susceptibility per spin at the critical point is expected to scale with system size such that

$$\chi_T(t=0) \sim L^{\gamma_T/\nu}, \tag{3.20}$$

and one can therefore utilize the slope of $\log(\chi_T)$ versus $\log L$ in conjunction with Equation (3.18) in order to extract another estimate for η_T.

We utilize the Monte Carlo methods of Section 3.1 to measure the observables m_T and χ_T at the critical temperature given in Equation (3.14). We perform simulations on cubic lattices with lengths $L = 8, 10, 12, 16, 24$ and 32 using a total of 10^7 Monte Carlo sweeps for each lattice. One Monte Carlo sweep (MCS) consists of $L^3/2$ local updates (Algorithm 3.1), followed by one Wolff cluster step (Algorithm 3.2), followed by another $L^3/2$ local updates.

In Figure 3.3, we plot the Monte Carlo results for m_T and χ_T on a logarithmic scale as a function of L for the case where the temperature is given by $T/J = 1.06835$, which is the the median expected critical temperature calculated in Reference [69] (see Equation (3.14)). Fits of the tensorial magnetization to Equation (3.17) in this case yield $\eta_T = 1.362(1)$, while fits of the tensorial susceptibility to Equation (3.18) predict $\eta_T = 1.361(1)$. The errors here are calculated by adding Gaussian noise to the Monte Carlo data and repeating the fitting procedure.

Due to the error in the value of T_c in Equation (3.14), we repeat the simulation and calculations at $T/J = 1.06822$ and $T/J = 1.06848$ (the upper and lower bounds for T_c/J). The resulting predictions for the anomalous dimension η_T are given in Table 3.1.

In Reference [68], Ballesteros, Fernández, Martín-Mayor and Muñoz Sudupe calculate η_T using methods similar to those described above, but with infinite volume extrapolations that account for additional finite size corrections in Equations (3.17) and (3.18) due to the first irrelevant operator. The results of three such extrapolations yield estimates of 1.374(5), 1.375(5) and 1.376(2) for the tensorial anomalous dimension η_T [68]. At $T/J = 1.06822$ and $T/J = 1.06835$, our results do not agree with these published values. However, at the upper-bound critical temperature $T/J = 1.06848$, our results are in partial agreement with the results of Ballestero *et al.* In order to obtain a more reliable estimate for this tensorial anomalous dimension, it would be best to first measure the critical temperature T_c to higher precision since the estimates for η_T are quite sensitive to temperature. In

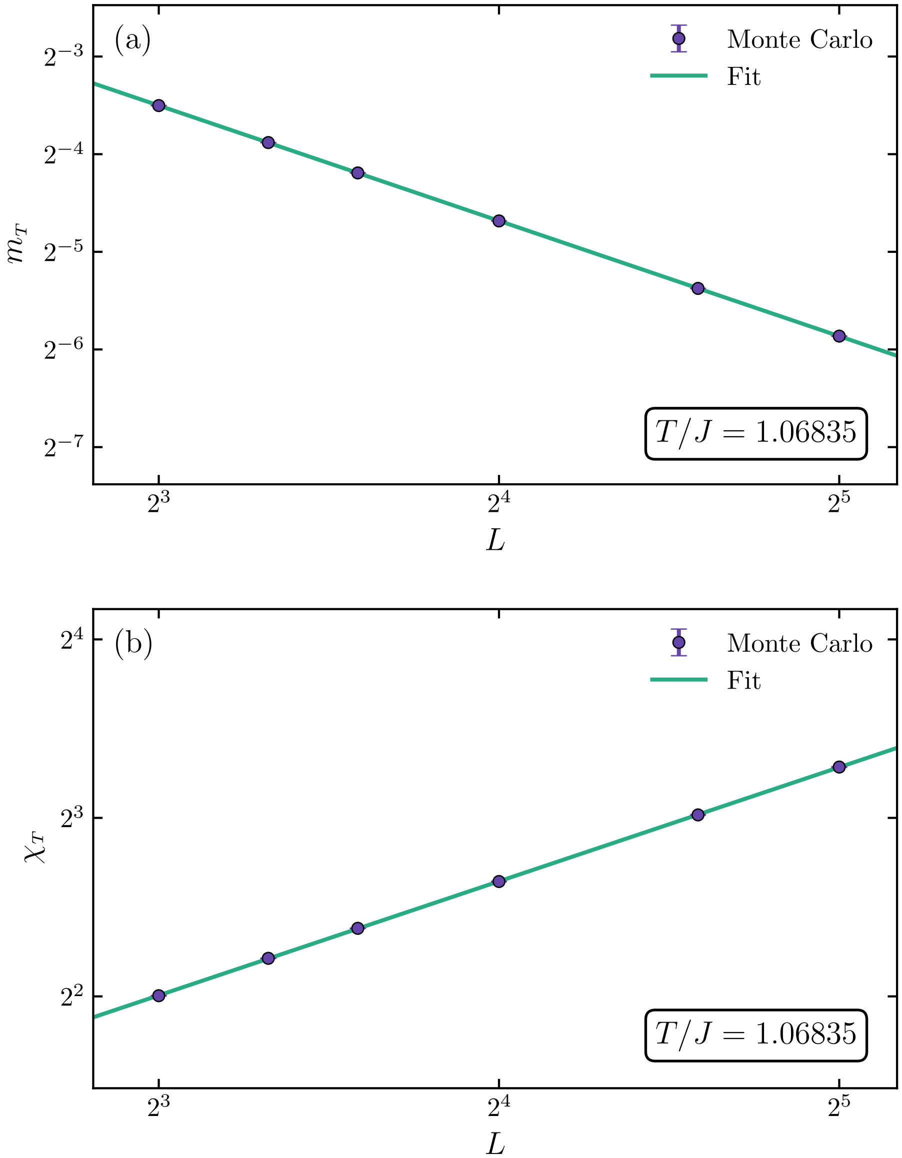

Figure 3.3: Fits used to extract the tensorial anomalous dimension η_T for the $O(4)$ model in $d = 3$. Note the logarithmic scale on both axes. In (a), we plot Monte Carlo results for m_T as a function of L and perform a fit to Equation (3.17). In (b), we plot χ_T versus L and fit to Equation (3.18). All data in this figure corresponds to $T/J = 1.06835$, which is estimated to be the median critical temperature [69] (see Equation (3.14)).

Estimate for T_c/J	Estimate for η_T	
	From m_T	From χ_T
1.06822	1.355(1)	1.354(1)
1.06835	1.362(1)	1.361(1)
1.06848	1.369(1)	1.368(1)

Table 3.1: Estimates for the tensorial anomalous dimension η_T for the $O(4)$ model in $d = 3$. We perform fits to Equations (3.17) and (3.18) using the lower-bound, median and upper-bound estimates for the critical temperature in Equation (3.14).

addition, we could improve the quality of our estimates by accounting for additional finite size corrections as in Reference [68]. Nonetheless, our results for η_T still give us confidence in the validity of our Monte Carlo methods, are we proceed to apply these methods to more exotic, previously unexplored models in the next chapter.

Chapter 4

Effective theories of high-temperature superconductivity

This chapter includes results from References [60], [70] and [71], as well as original results not published elsewhere.

As introduced in Section 1.1, coarse-graining procedures provide useful approaches to addressing the issues of exponential complexity that are inherently present within interacting many-body systems. In principle, all models within condensed matter physics employ some degree of coarse-graining since the Hamiltonian rarely accounts for interactions at the subatomic level. In some situations, the coarse-grained order parameter can be expressed in terms of certain measurable microscopic variables while, for other models, this order parameter represents a more effective description of the system. For lattice models in the latter case, the effective model describes interactions at a new characteristic lattice length scale that, in general, has an unknown relationship to the system's (smaller) underlying physical lattice spacing.

In this chapter, we describe techniques for developing effective field theories in the context of strongly-interacting systems by exploiting certain fundamental symmetries. We specifically focus on building such an effective theory to describe exotic behaviours of high-temperature superconductors within their mysterious pseudogap regime.

4.1 The cuprate pseudogap

While a microscopic description of the mechanism responsible for low-temperature (conventional) superconductivity was established in 1957 [72, 73], a corresponding microscopic theory for high-temperature superconducting materials has eluded physicists since the discovery of such materials in 1986 [74]. However, even though this microscopic mechanism remains unknown, many characteristic features and symmetries of high-temperature superconductors have been established over the past several decades, and effective theories can yield valuable predictions and insight by exploiting such features. One distinguishing characteristic of high-temperature superconductors is the existence of the so-called *pseudogap* regime, which corresponds to temperatures above the superconducting (SC) critical temperature T_c. Within this regime, the Fermi surface has a momentum-dependent energy gap that disappears along certain momentum directions.

Many of the most widely-studied high-temperature superconductors belong to a class of materials known as *cuprates*. One such cuprate material is $\mathrm{YBa_2Cu_3O_{6+x}}$ (YBCO), for which the underlying elemental structure is shown in Figure 4.1. Recent x-ray scattering experiments on YBCO [75, 76, 77] have detected significant spatial fluctuations of charge distribution, known as charge-density wave (CDW) order, which is now widely believed to be a ubiquitous feature of the cuprate pseudogap regime. In order to detect such fluctuations, these experiments first measure scattering intensities as a function of wave vector $\mathbf{q}$ and then extract the peak value of this intensity as a function of temperature.

The resulting CDW order in these experiments increases gradually as one lowers the temperature from $T \approx 200\,\mathrm{K}$ down to temperatures in the vicinity of T_c. As shown in Figure 4.2, the x-ray scattering intensity corresponding to CDW order has a concave-upward shape as a function of temperature during this onset, which is different from the concave-downward shape that is traditionally observed for an order parameter corresponding to a broken symmetry. By analogy with previous work [78, 79, 80], this concave-upward shape suggests that the underlying effective model leading to this behaviour may correspond to angular fluctuations of an order parameter with at least three components, much like the model of Equation (3.1) (with $N \geq 3$). In the following section, we discuss in more detail the specific symmetries that constrain the form of our effective model.

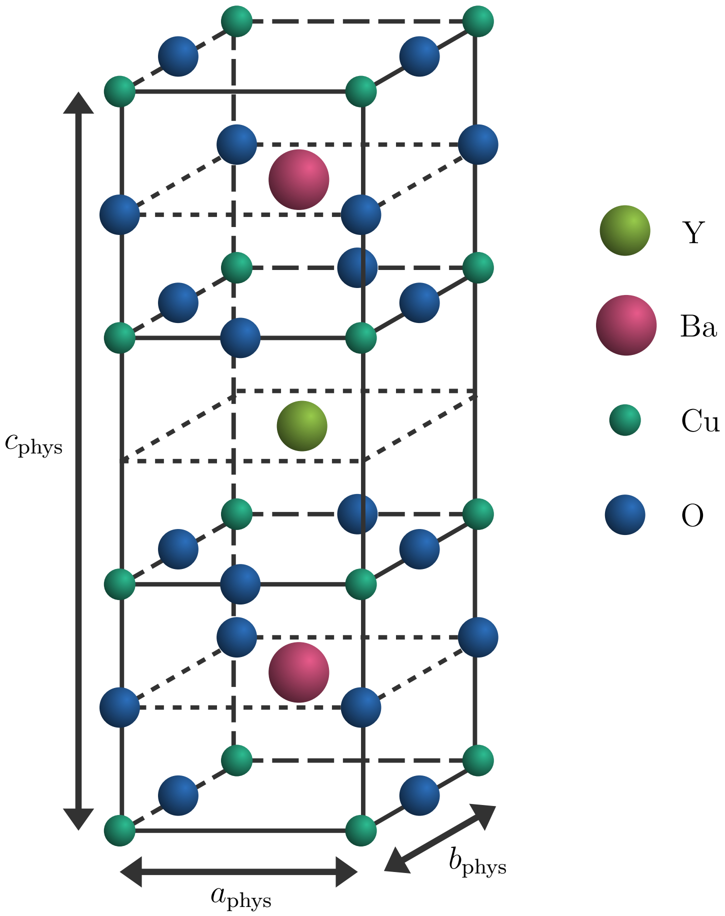

Figure 4.1: The underlying physical lattice structure of $\mathrm{YBa_2Cu_3O_7}$ with lattice parameters a_{phys}, b_{phys} and c_{phys}. We compare our simulation data with experimental results on related compounds $\mathrm{YBa_2Cu_3O_{6+x}}$, with $0.5 \lesssim x \lesssim 0.67$.

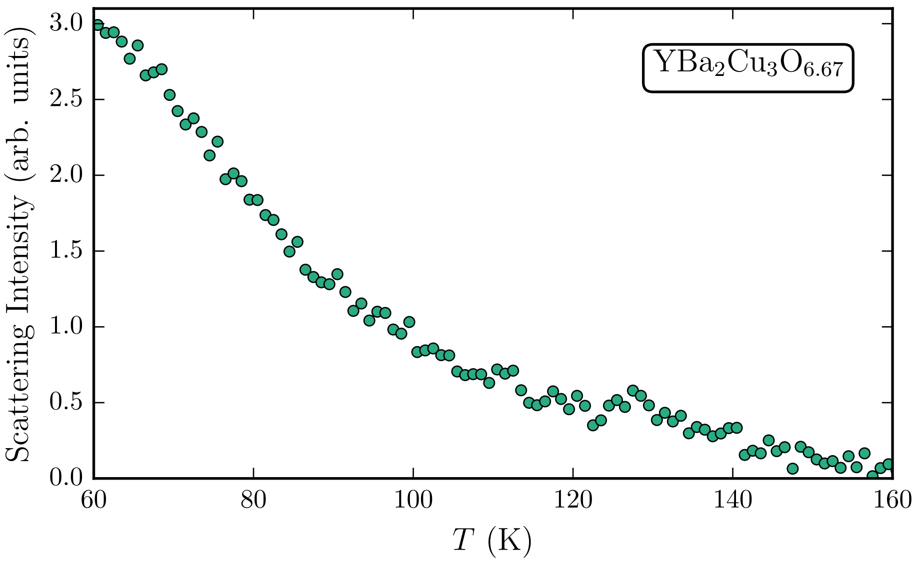

Figure 4.2: Peak CDW scattering intensities resulting from resonant soft x-ray scattering experiments on YBa$_2$Cu$_3$O$_{6.67}$ [81]. This material has superconducting critical temperature $T_c = 65.5\,\mathrm{K}$, and the plotted data corresponds to wave vector $\mathbf{q} = (-0.31, 0, 1.48)$. The CDW order increases with a concave-up shape as the temperature is lowered down to T_c.

4.2 Competing superconducting and charge-density wave orders

Experimental observations of CDW order through x-ray scattering have led to the suggestion that CDW order plays a significant role in the physics of the pseudogap regime of the cuprate superconductors. In particular, it seems likely that the competition between CDW order and SC order within the this regime can help to explain the destruction of SC order as one raises the temperature above T_c. We now propose a model for the pseudogap regime of the cuprate superconductors that incorporates this competition.

Our model is described by a six-dimensional order parameter $\mathbf{n}(\mathbf{r})$ [60]. This order parameter has components $n_\alpha(\mathbf{r})$, with $\alpha = 1, 2, \ldots, 6$. The first two components of the order parameter represent the SC order, which is given by the complex field

$$\Psi(\mathbf{r}) \propto n_1(\mathbf{r}) + in_2(\mathbf{r}). \tag{4.1}$$

The remaining four components of $\mathbf{n}(\mathbf{r})$ represent the charge-density wave order along the x and y directions, which are given respectively by the fields

$$\begin{aligned} \Phi_x(\mathbf{r}) &\propto n_3(\mathbf{r}) + in_4(\mathbf{r}), \\ \Phi_y(\mathbf{r}) &\propto n_5(\mathbf{r}) + in_6(\mathbf{r}). \end{aligned} \tag{4.2}$$

We consider these degrees of freedom to interact with each other in two-dimensional space such that the vectors $\mathbf{r}$ have two components. In Section 4.6, we further extend our model to consider interactions in three-dimensional space.

We assume that the system always prefers to acquire either SC or CDW order locally. As a result, the magnitude of $\mathbf{n}(\mathbf{r})$ is non-negligible at every location $\mathbf{r}$. The order parameter is thus excluded from existing in the vicinity of the origin of the six-dimensional space defined by the components of $\mathbf{n}(\mathbf{r})$. At low T, we expect the system to acquire SC order such that the order parameter lives mainly within the two-dimensional plane corresponding to Ψ. However, as the temperature increases, we expect the order parameter to explore the entire six-dimensional space more completely. See Figure 4.3 for a visualization of these expectations at low and high temperatures. At intermediate temperatures (within the pseudogap regime), we expect the system to be characterized by a competition between SC and CDW order. We note that, in the limit of very high temperatures, this assumption is not valid since a thermal system no longer acquires any type of local order as $T \to \infty$. We therefore do not expect our model to agree with experimental observations in the limit of high temperatures.

The above assumptions indicate that radial fluctuations of $\mathbf{n}(\mathbf{r})$ are restricted and less significant to the underlying physics than angular fluctuations within the six-dimensional space. In order to further simplify our model in the calculations that follow, we neglect amplitude fluctuations completely and take the order parameter to be a unit vector $\hat{\mathbf{n}}(\mathbf{r})$. Our effective model accounts for the competition between SC and CDW order in the pseudogap regime through angular fluctuations of these unit vectors.

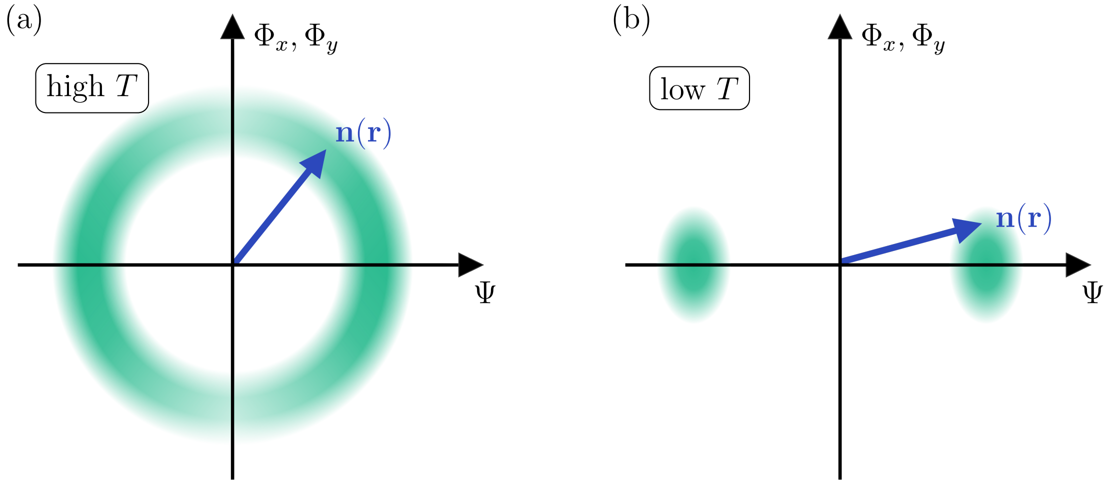

Figure 4.3: Expected behaviour of the order parameter $\mathbf{n}(\mathbf{r})$ at (a) high and (b) low temperatures. The competition between SC and CDW order is accounted for by angular fluctuations of $\mathbf{n}(\mathbf{r})$ within a six-dimensional space. At high temperatures, the system explores both SC and CDW order. At low temperatures, we expect the system to prefer SC order.

4.2.1 Effective classical Hamiltonian

The partition function we introduce to describe angular fluctuations of the unit vectors $\hat{\mathbf{n}}(\mathbf{r})$ is given by

$$\mathcal{Z} = \int \mathcal{D}\mathbf{n}\, \delta\left(\sum_{\alpha=1}^{6} n_\alpha^2(\mathbf{r}) - 1\right) e^{-\beta H}, \tag{4.3}$$

where $\int \mathcal{D}\mathbf{n} \equiv \prod_{\mathbf{r}} \prod_\alpha \int n_\alpha(\mathbf{r})$ denotes a functional integral and the Hamiltonian is given in the continuum by [60, 70]

$$\begin{aligned} H = \frac{\rho_s}{2} \int d^2\mathbf{r} \Bigg[& \sum_{\alpha=1}^{2} (\nabla n_\alpha)^2 + \lambda \sum_{\alpha=3}^{6} (\nabla n_\alpha)^2 + g \sum_{\alpha=3}^{6} n_\alpha^2 \\ & + g' \left(\sum_{\alpha=3}^{6} n_\alpha^2 \right)^2 + w \left[\left(n_3^2 + n_4^2\right)^2 + \left(n_5^2 + n_6^2\right)^2 \right] \Bigg], \end{aligned} \tag{4.4}$$

with the additional constraint that $\sum_{\alpha=1}^{6} n_\alpha^2(\mathbf{r}) = 1$ such that $\mathbf{n}(\mathbf{r})$ is a unit vector at every location $\mathbf{r}$. The parameters ρ_s, λ, g, g' and w are used to describe the material-dependent features of hole-doped cuprate superconductors and are taken to be temperature-independent. The parameter ρ_s corresponds to the zero-temperature helicity modulus, which controls the overall temperature scale. The coupling λ represents the relative energy cost for spatial variations of SC versus CDW order. The parameters g and g' are coefficients of quadratic and quartic energy anisotropy terms (respectively) and together they represent the relative energy cost for ordering along the SC versus CDW directions. Finally, the parameter w controls the relative energy cost for the chosen symmetry of the CDW order. When $w < 0$, the energy is minimized when the system imposes stripe CDW order such that only one of Φ_x or Φ_y is nonzero. On the other hand, when $w > 0$, the system prefers checkerboard CDW order such that the CDW order is split equally along the x and y lattice directions.

We note that when $\lambda = 1$ and $g = g' = w = 0$, this Hamiltonian respects an $O(6)$ symmetry (and, as discussed in Section 4.2, we also expect for general choices of parameters that the Hamiltonian respects an approximate $O(6)$ symmetry in the limit of high temperatures). When $w = 0$, but $\lambda \neq 1$, $g \neq 0$ or $g' \neq 0$, then this symmetry is broken down to $O(2) \times O(4)$. The w term is responsible for breaking the $O(4)$ symmetry corresponding to the four CDW components of $\hat{\mathbf{n}}(\mathbf{r})$ down to $O(2) \times O(2) \rtimes \mathbb{Z}_2$, where the $\mathbb{Z}_2$ represents the symmetry between x and y. For general choices of parameters, the resulting overall symmetry is thus given by $O(2) \times O(2) \times O(2) \rtimes \mathbb{Z}_2$.

In order to perform Monte Carlo simulations corresponding to this Hamiltonian, we place the system on a two-dimensional square lattice with L sites along both the x and y directions. We choose a lattice with periodic boundary conditions, lattice spacing a and sites labelled by index i. The discretized version of the Hamiltonian is then given by

$$H = H_1 + H_2, \tag{4.5}$$

where

$$H_1 = \frac{\rho_s}{2} \sum_{\langle ij \rangle} \left[\sum_{\alpha=1}^{2} (n_{i\alpha} - n_{j\alpha})^2 + \lambda \sum_{\alpha=3}^{6} (n_{i\alpha} - n_{j\alpha})^2 \right] \tag{4.6}$$

and

$$H_2 = \frac{\rho_s a^2}{2} \sum_{i} \left[g \sum_{\alpha=3}^{6} n_{i\alpha}^2 + g' \left(\sum_{\alpha=3}^{6} n_{i\alpha}^2 \right)^2 + w \left[\left(n_{i3}^2 + n_{i4}^2 \right)^2 + \left(n_{i5}^2 + n_{i6}^2 \right)^2 \right] \right]. \tag{4.7}$$

Here, as in Equations (2.1) and (1.2), $\langle ij \rangle$ denotes that the corresponding sum is over all nearest-neighbouring pairs of sites on the lattice. The total number of sites on the lattice is $N_{\text{sites}} = L^2$. We emphasize that, since the lattice Hamiltonian H represents an effective theory, the lattice spacing a is not given by any of the lattice parameters a_{phys}, b_{phys} and c_{phys} for the physical underlying lattice illustrated in Figure 4.1.

By expanding the factors of $(n_{i\alpha} - n_{j\alpha})^2$ in the expression for H_1, one can write the Hamiltonian as

$$\begin{aligned}\frac{H}{\rho_s} = &-\sum_{\langle ij\rangle}\left[\sum_{\alpha=1}^{2} n_{i\alpha}n_{j\alpha} + \lambda\sum_{\alpha=3}^{6} n_{i\alpha}n_{j\alpha}\right] \\ &+ \frac{1}{2}\sum_{i}\left[\left[ga^2 + 4(\lambda-1)\right]\sum_{\alpha=3}^{6} n_{i\alpha}^2 + g'a^2\left(\sum_{\alpha=3}^{6} n_{i\alpha}^2\right)^2\right. \\ &\left. + wa^2\left[\left(n_{i3}^2 + n_{i4}^2\right)^2 + \left(n_{i5}^2 + n_{i6}^2\right)^2\right]\right],\end{aligned} \tag{4.8}$$

which is of the same form as Equation (3.1) when $\lambda = 1$. As a result, one can use the Monte Carlo method described in Algorithm 3.2 (as well as local updates and more sophisticated methods that are discussed in Section 4.3.2) in order to compute observables corresponding to this Hamiltonian in the case where the couplings are isotropic such that $\lambda = 1$.

In Figure 4.4, we show a sample configuration from a Monte Carlo simulation of Equation (4.8) for a given set of model parameters. This sample was taken at temperature $T/\rho_s = 0.18$, which is below the SC critical temperature T_c, as will be discussed in Section 4.4.2). This figure illustrates the competition between SC and CDW order within our model. Specifically, it is known through the theory developed by Berezinskii, Kosterlitz and Thouless that the loss of superconducting order as temperature increases is related to an increased presence of SC vortex-antivortex pairs, which become unbound for temperatures above T_c [82, 83, 84, 85, 86]. Here, we see that the SC vortices and antivortices observed in our sampling (which correspond to regions of weakened SC order) are indeed correlated with spatial regions of enhanced CDW order.

4.2.2 Ground-state order

At zero temperature, the system exists in a state where its energy is minimized. From Equations (4.4) and (4.5), we see such a state is thus spatially uniform such that the gradient terms in Equation (4.4) (or, equivalently, the finite difference terms in Equation (4.6))

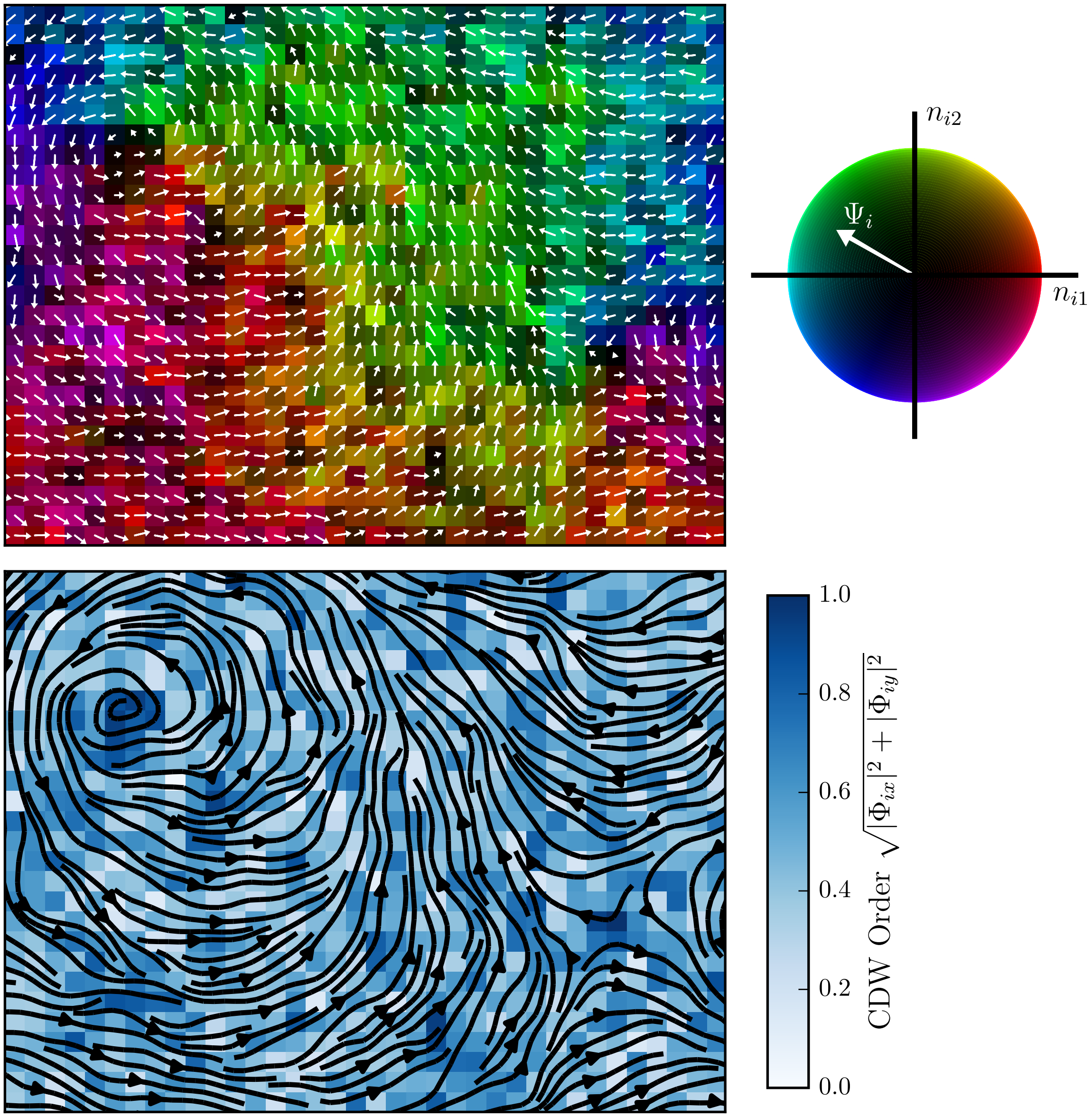

Figure 4.4: Two visualizations of a sample Monte Carlo configuration for the model described by Equation (4.8) for parameters $\lambda = 1$, $ga^2 = 0.4$, $g'a^2 = 0.0$, $wa^2 = -0.2$, $L = 64$ and $T/\rho_s = 0.18$. In the upper plot, we use white arrows as well as colour and shading to illustrate the magnitude and orientation of the degrees of freedom in the SC plane. Darker shading corresponds to stronger CDW magnitude. In the lower plot, the colour corresponds to the CDW magnitude while the black arrow are the streamlines of the SC order.

Favoured CDW order	Ground state	Constraints on g and g'
Stripe ($w < 0$)	SC	$g > 0, \quad g + g' > -w$
	CDW	$g + g' < -w, \quad g + 2g' < -2w$
	SC + CDW	$g < 0, \quad g + 2g' > -2w$
Checkerboard ($w > 0$)	SC	$g > 0, \quad 2g + 2g' > -w$
	CDW	$2g + 2g' < -w, \quad g + 2g' < -w$
	SC + CDW	$g < 0, \quad g + 2g' > -w$

Table 4.1: Ground-state phases corresponding to the model in Equation (4.8). The type of CDW order depends upon the sign of the model parameter w. The corresponding phase diagrams are shown in Figure 4.5.

vanish and one can write $n_{i\alpha} = n_\alpha$ for all lattice sites i. Determining the ground state then amounts to determining the components n_α that minimize H_2 in Equation (4.7).

As discussed in Section 4.2.1, when $w < 0$ our model prefers for the CDW to be stripe-like such that only one of Φ_x or Φ_y is nonzero. In this case one can choose an orientation of the CDW order such that the ground state satisfies

$$n_\alpha = (\cos\theta, 0, \sin\theta, 0, 0, 0) \tag{4.9}$$

for some angle θ that depends on the parameters of our model. The ground state corresponds to SC order when $\theta = 0$ or π, while it corresponds to CDW order when $\theta = \pi/2$ or $3\pi/2$. For all other angles, the SC and CDW orders coexist and we label the ground state as SC + CDW. From this expression for n_α, the ground-state Hamiltonian is then given by

$$H_{\text{g.s.}}(\theta, w < 0) = H_2(\theta) = \frac{\rho_s a^2 L^2}{2}\left[g\sin^2\theta + (g' + w)\sin^4\theta\right]. \tag{4.10}$$

Minimizing $H_{\text{g.s.}}(\theta, w < 0)$ then allows us to determine the ground-state order as a function of our model parameters. The results are summarized in Table 4.1 and illustrated in Figure 4.5a.

On the other hand, when $w > 0$ the system favours checkerboard CDW order such that the magnitudes of Φ_x and Φ_y are equal. One can then specify the ground state according

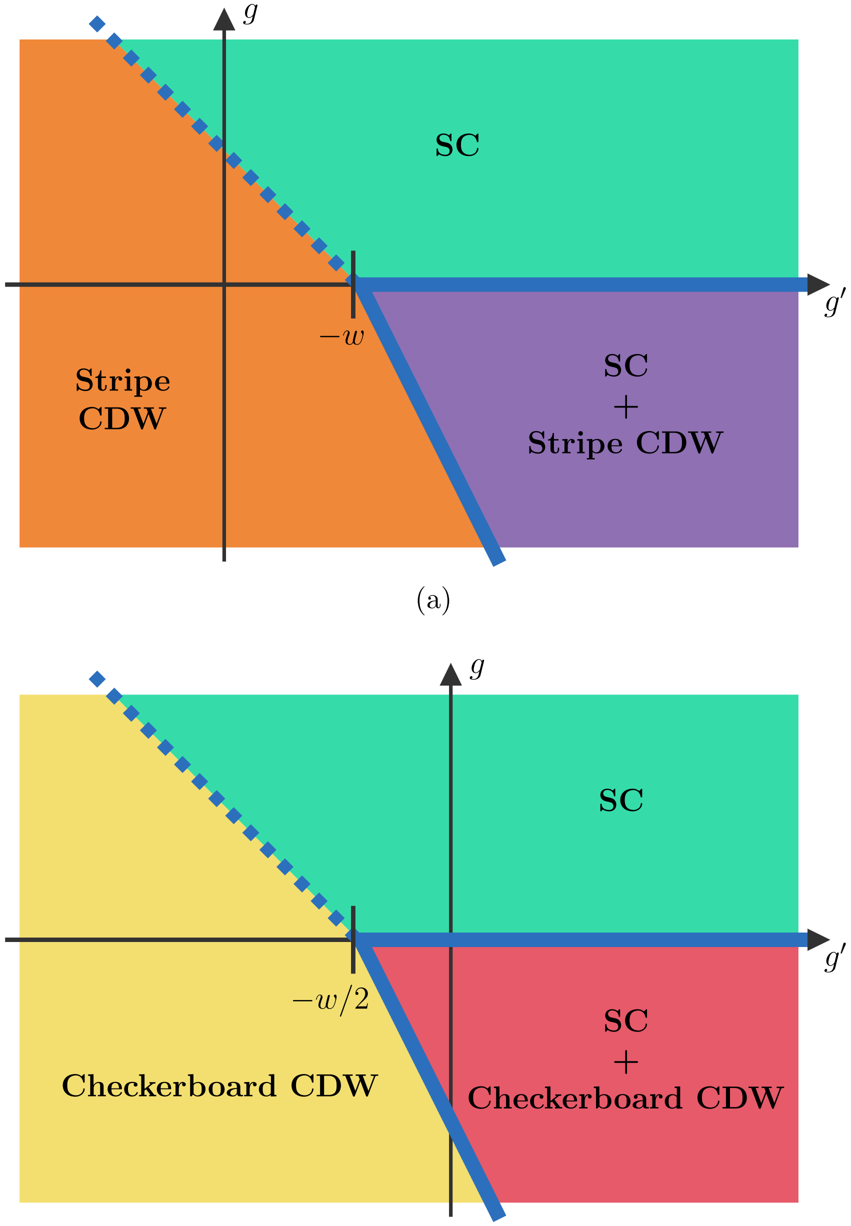

(a)

(b)

Figure 4.5: Ground-state phase diagrams for the model in Equation (4.8) when (a) $w < 0$ and (b) $w > 0$. The dashed lines indicate first-order phase transitions, while the solid lines mark second-order transitions.

to

$$n_\alpha = \left(\cos\theta, 0, \frac{\sin\theta}{\sqrt{2}}, 0, \frac{\sin\theta}{\sqrt{2}}, 0\right), \tag{4.11}$$

where the value of θ corresponds to the nature of the ground state as before. In this case the ground-state Hamiltonian is given by

$$H_{\text{g.s.}}(\theta, w > 0) = H_2(\theta) = \frac{\rho_s a^2 L^2}{2}\left[g\sin^2\theta + \left(g' + \frac{w}{2}\right)\sin^4\theta\right]. \tag{4.12}$$

Comparing Equations (4.12) and (4.10) then shows that the parameters that minimize $H_{\text{g.s.}}(\theta, w > 0)$ are the same as those for $H_{\text{g.s.}}(\theta, w < 0)$ except that one must replace w with $w/2$. The resulting parameter-dependent ground states are listed in Table 4.1 and the ground-state phase diagram is shown in Figure 4.5b.

Since we wish compare with experimental materials that are superconductors at low temperatures, we restrict our choices of model parameters g, g' and w such that the ground state corresponds to SC order.

4.3 Analytical and numerical techniques

In this section, we examine various techniques for measuring the expectation value of observable quantities $\mathcal{O}$ within the model given by Equation (4.8). Such expectation values depend on the Hamiltonian H according to Equation (3.3). One observable that we will be particularly interested in computing in the following sections is the CDW structure factor S_{Φ_x}, since it can be compared with the peak x-ray scattering intensities that are plotted in Figure 4.2. We introduce an explicit expression for S_{Φ_x} in Section 4.4.1. Here, we start by describing an approximate analytical method for computing the expectation values of certain observables. We then compare the results with exact numerical results from Monte Carlo simulations. We show that although such analytical approximations are valid at certain temperatures, numerical techniques are necessary in order to extract the predictions of the effective theory of Equation (4.8) for temperatures in the vicinity of the superconducting phase transition T_c. We then proceed to develop Monte Carlo cluster updates in order to efficiently simulate this theory.

4.3.1 Large-N expansion

While observables corresponding to the Hamiltonian in Equation (4.4) or (4.8) cannot be calculated exactly, one can obtain an approximation for such observables by considering a more general model where the order parameter $\hat{\mathbf{n}}(\mathbf{r})$ has N components rather than 6 components. In such a model, the SC field Ψ corresponds to the components $n_1(\mathbf{r}), n_2(\mathbf{r}), \ldots, n_{N/3}(\mathbf{r})$ and the CDW fields Φ_x and Φ_y correspond to the components $n_{(N/3)+1}(\mathbf{r}), n_{(N/3)+2}(\mathbf{r}), \ldots, n_{2N/3}(\mathbf{r})$ and $n_{(2N/3)+1}(\mathbf{r}), n_{(2N/3)+2}(\mathbf{r}), \ldots, n_N(\mathbf{r})$ (respectively). The Hamiltonian for this generalized N-component order parameter is given by [60]

$$\begin{aligned} \frac{H_N}{\rho_s} = &- \sum_{\langle ij \rangle} \left[\sum_{\alpha=1}^{N/3} n_{i\alpha} n_{j\alpha} + \lambda \sum_{\alpha=(N/3)+1}^{N} n_{i\alpha} n_{j\alpha} \right] \\ &+ \frac{1}{2} \sum_i \left(\left[g a^2 + 4(\lambda - 1) \right] \sum_{\alpha=(N/3)+1}^{N} n_{i\alpha}^2 + g' a^2 \left(\sum_{\alpha=(N/3)+1}^{N} n_{i\alpha}^2 \right)^2 \right. \\ &\qquad \left. + w a^2 \left[\left(\sum_{\alpha=(N/3)+1}^{2N/3} n_{i\alpha}^2 \right)^2 + \left(\sum_{\alpha=(2N/3)+1}^{N} n_{i\alpha}^2 \right)^2 \right] \right) . \end{aligned} \tag{4.13}$$

Such a model can be solved analytically in the limit of large N [60]. In Figure 4.6a, we compare results for the CDW structure factor (to be defined in Section 4.4.1) as extracted from this large-N analytical expansion versus exact numerical calculations from Monte Carlo simulations. Since experimental results yield scattering intensities in arbitrary units, in the following sections we fit a parameter that rescales the y-axis of such structure factor plots. Therefore, in Figure 4.6b we plot the same curves as in Figure 4.6a, but with the Monte Carlo data rescaled such that the location of the peak structure factors match. In both plots, we find that these methods yield significant differences for certain model parameters and temperatures. We therefore turn to Monte Carlo methods in order to extract exact estimates for observables from the model of Equation (4.8).

4.3.2 Monte Carlo methods

We use a combination of local and Wolff cluster updates as described in Section 3.1 in order to simulate the effective Hamiltonian of Equation (4.8). However, since the Wolff

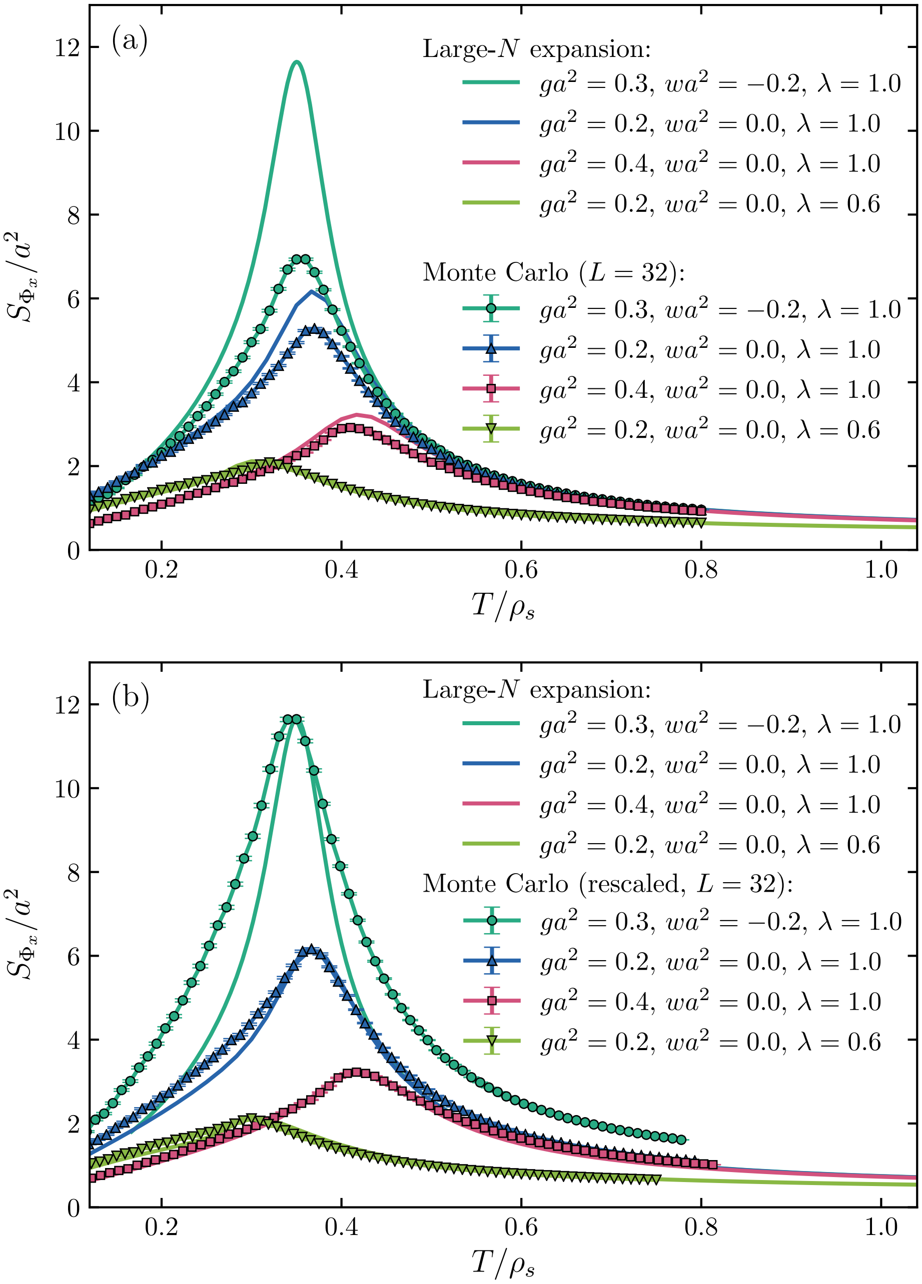

Figure 4.6: Comparisons of results for the CDW structure factor S_{Φ_x} using large-N analytical methods versus exact Monte Carlo simulations. In (a), we compare directly the results extracted from these two methods, while in (b) we rescale the y-axis of the Monte Carlo data such that the locations of the peak structure factors match. Note that all curves have the model parameter $g'a^2$ set to zero.

cluster update of Algorithm 3.2 can only be performed in the case where the nearest-neighbour couplings are isotropic in the six-dimensional space of the order parameter, we restrict most of our Monte Carlo studies to the parameter regime where $\lambda = 1$. In this case, the Hamiltonian can be written (in the same form as Equation (3.1)) as a sum of a nearest-neighbour interaction term (with isotropic interactions for all components α) and an on-site energy term as

$$H_{\lambda=1} = H_{\text{n.n.}} + H_{\text{on-site}}, \tag{4.14}$$

where

$$H_{\text{n.n.}} = -\rho_s \sum_{\langle ij \rangle} \hat{\mathbf{n}}_i \cdot \hat{\mathbf{n}}_j \tag{4.15}$$

and

$$H_{\text{on-site}} = \frac{\rho_s a^2}{2} \sum_i \left[g \sum_{\alpha=3}^{6} n_{i\alpha}^2 + g' \left(\sum_{\alpha=3}^{6} n_{i\alpha}^2 \right)^2 + w \left[\left(n_{i3}^2 + n_{i4}^2 \right)^2 + \left(n_{i5}^2 + n_{i6}^2 \right)^2 \right] \right]. \tag{4.16}$$

Recall that, in the Wolff method of Algorithm 3.2, a random vector $\mathbf{v}$ on the six-dimensional unit sphere is generated and clusters of spins (with the same sign of projection onto $\mathbf{v}$) are then reflected about the hyperplane normal to $\mathbf{v}$. Within this model, once a cluster is generated, it is accepted or rejected with probability given by Equation (3.12), which depends upon the difference $\Delta E_{\text{on-site}}$ in the on-site energy (as calculated using Equation (4.16)) that would result from reflecting the cluster of spins built during the first stage of the algorithm. Such cluster moves are most beneficial at low T, where the configurations and observables corresponding to local updates can get stuck in local energy minima and become non-ergodic for the typical time scales used for the simulations.

We note that this Wolff cluster algorithm considers all directions of the six-dimensional order parameter space symmetrically. Many of the proposed cluster moves vainly attempt to reflect spin clusters about random hyperplanes in the $O(6)$ unit sphere, without making use of all the information known about the Hamiltonian's symmetry. As a result, many of the proposed cluster moves correspond to large increases in energy that are rarely accepted, especially at low temperatures where efficient cluster updates are most needed. In the left-hand side of Figure 4.7, we show histograms of the typical cluster sizes that are generated and accepted within this Wolff algorithm. At $T/\rho_s = 0.1$ less than 0.1% of the largest clusters generated by the algorithm are accepted, which indicates that this algorithm is quite inefficient at low temperatures. At the higher temperature $T/\rho_s = 0.5$ (which is above the superconducting critical temperature, as will be discussed in Section 4.4.2), most of the generated clusters are accepted and we note that the typical cluster sizes are smaller than in the low-temperature regime.

This original Wolff cluster algorithm would yield efficient updates for a Hamiltonian with $O(6)$ symmetry. However, since we know that the Hamiltonian in Equation (4.8) has $O(2) \times O(2) \times O(2) \rtimes \mathbb{Z}_2$ symmetry, we now proposed a new cluster move that takes advantage of the $O(2)$ symmetry for each of the three complex fields Ψ, Φ_x and Φ_y. Within this new cluster algorithm, the random vector $\mathbf{v}$ is constrained to one of the $O(2)$ unit circles corresponding to the $n_1 - n_2$ plane, the $n_3 - n_4$ or the $n_5 - n_6$ plane. Spins in the resulting clusters are then only reflected about hyperplanes that are orthogonal to one of the three $O(2)$ unit circles, which corresponds to a rotation within the corresponding two-dimensional plane. Such rotations never change the on-site energy of the system and, as a result, the cluster moves generated within this new method are always accepted. The steps of this $O(2)$ method are summarized in Algorithm 4.1.

Algorithm 4.1: Cluster algorithm for non-local Monte Carlo updates for the model in Equation (4.8). This algorithm explicitly exploits the Hamiltonian's $O(2) \times O(2) \times O(2) \rtimes \mathbb{Z}_2$ symmetry.

```
choose a random 6-dimensional unit vector $\mathbf{v}$ within either the $n_1 - n_2$
  plane, the $n_3 - n_4$ or the $n_5 - n_6$ plane;
execute steps 2-9 of Algorithm 3.2 to build a cluster;
//reflect all spins in the cluster (with probability one):
for each site $i$ in the cluster do
    reflect $\mathbf{n}_i$ about the hyperplane orthogonal to $\mathbf{v}$ such that
    $\mathbf{n}_i \rightarrow R(\mathbf{v})\mathbf{n}_i = \mathbf{n}_i - 2(\mathbf{v} \cdot \mathbf{n}_i)\mathbf{v}$;
end
```

In the right-hand side of Figure 4.7, we examine histograms of the sizes of clusters that are generated within this algorithm at both high and low temperature. We find that the sizes of clusters generated are comparable to those of the original cluster method, and therefore this new method offers a significant advantage since the proposed clusters are always accepted.

In Figure 4.8, we show the runtime for each cluster algorithm as a function of temperature.

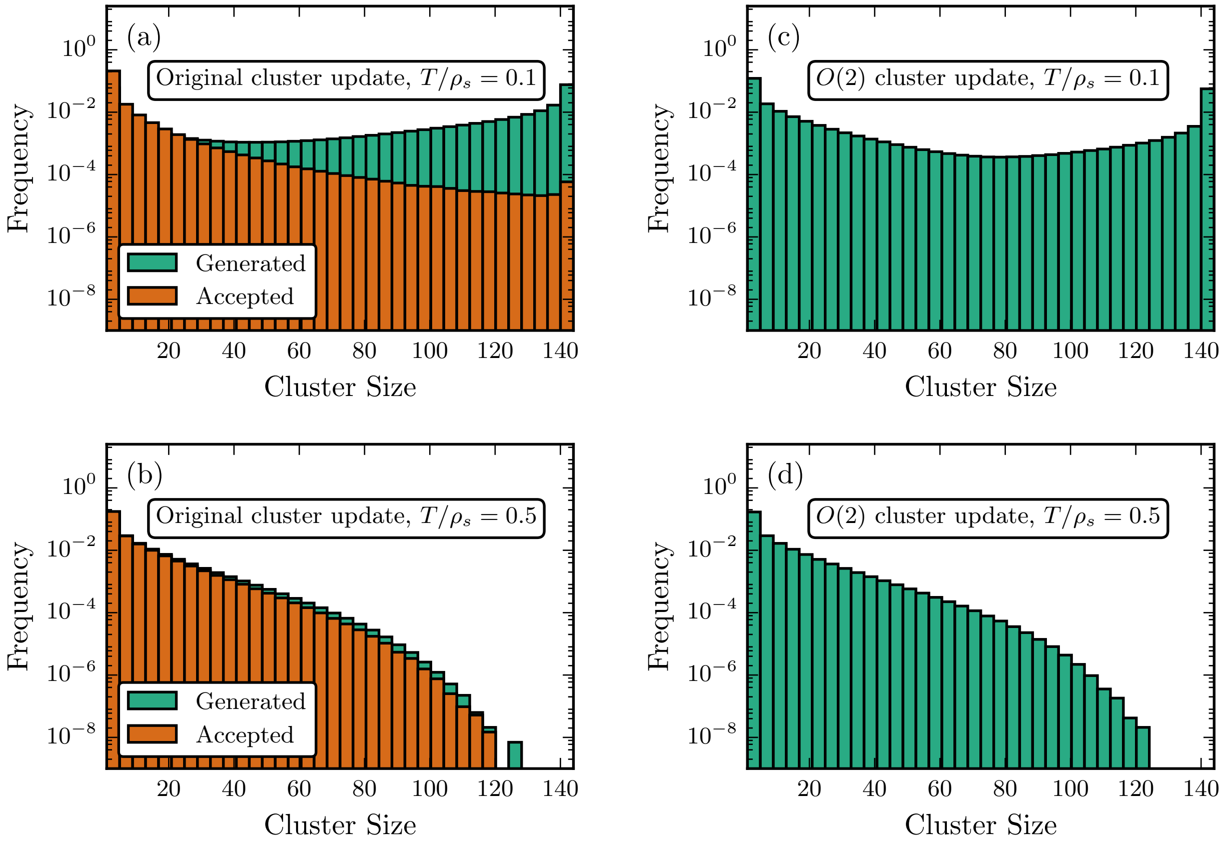

Figure 4.7: Histograms of the sizes of the clusters that are built within two Monte Carlo cluster algorithms. Note the logarithmic scale on the y-axis. These histograms are normalized such that the frequencies sum to one. In (a) and (b), we study the clusters sizes for the original Wolff method described in Algorithm 3.2. At low temperatures, less than 0.1% of the largest clusters generated by the algorithm are accepted. In (c) and (d), we show the cluster sizes for the improved method described in Algorithm 4.1, which exploits the symmetries of the Hamiltonian. All cluster updates are accepted within this algorithm. Note that plots (a) and (c) correspond to $T/\rho_s = 0.1$, while (b) and (d) correspond to $T/\rho_s = 0.5$. All simulations for these histograms are performed on lattices of size $L = 12$ and use model parameters $\lambda = 1$, $ga^2 = 0.35$, $g'a^2 = 0.00$, $wa^2 = -0.20$.

We find that these algorithms require similar runtimes at high temperatures, but the $O(2)$ algorithm becomes much faster in at lower temperatures $T/\rho_s \lesssim 0.35$. The inset of this figure shows that both algorithms yield a similar error bar for the CDW structure factor (to be defined in Section 4.4.1) at all temperatures.

In the sections that follow, we utilize local Monte Carlo updates (Algorithm 3.1) as well as both the original Wolff cluster updates (Algorithm 3.2) and the $O(2)$ cluster updates. When using the latter cluster algorithm, we always perform an equal number of updates for each of the three $O(2)$ unit circles corresponding to the fields Ψ, Φ_x and Φ_y.

4.4 Comparisons with experiment

In order to test the validity of the model corresponding to Equation (4.8), we use the Monte Carlo algorithms presented in Section 4.3.2 to generate predictions for various experimentally-measurable quantities. In particular, here we compare predictions corresponding to various sets of model parameters with experimental data obtained through resonant soft x-ray scattering [81]. We start by comparing our simulation results with the scattering intensities corresponding to CDW order, which experimentally have an intriguing concave-upward shape over a wide range of temperatures above T_c, as discussed in Section 4.1. We also investigate the value of T_c within our model and compare with the location of the peak in the CDW order. In later sections, we will introduce and explore additional quantities, such as diamagnetic susceptibility and CDW correlation length.

4.4.1 Charge-density wave structure factor

In order to compare our model with resonant soft x-ray scattering experiments that probe CDW order, we calculate the CDW structure factor. This structure factor is a Fourier transform of the two-point CDW correlation function C_{Φ_x} and is given by [3]

$$S_{\Phi_x}(\mathbf{q}) = \sum_{\mathbf{r}} C_{\Phi_x}(\mathbf{r})\, e^{i\mathbf{q}\cdot\mathbf{r}} = \sum_{\mathbf{r}} C_{\Phi_x}(\mathbf{r})\, \cos\left(\mathbf{q}\cdot\mathbf{r}\right), \tag{4.17}$$

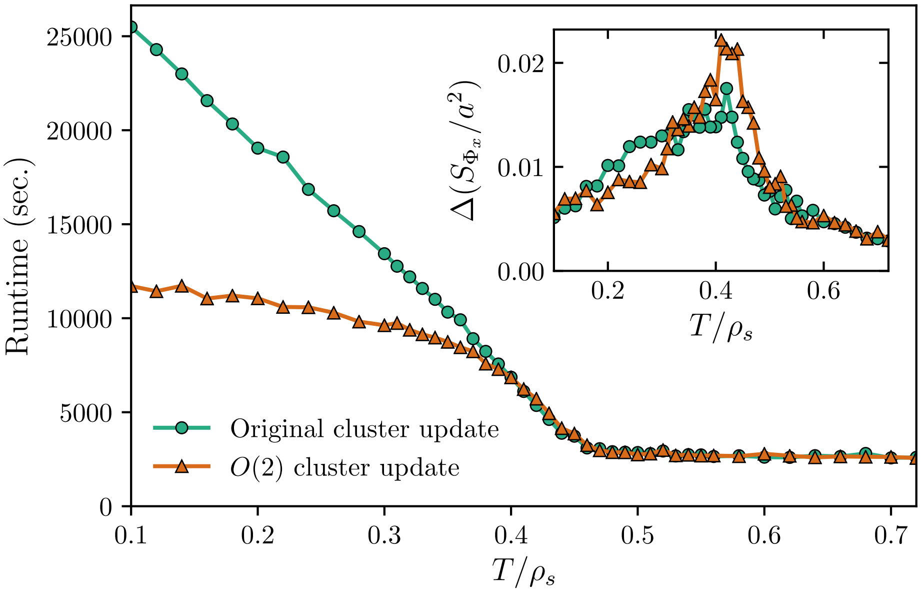

Figure 4.8: Runtimes as a function of temperature for the original Wolff cluster method (Algorithm 3.2) and the $O(2)$ method (Algorithm 4.1). For each value of temperature, we run $10^6 \times L^3$ local Monte carlo updates as well as $10^6 \times L \times 3$ cluster updates. For the original cluster method, all cluster updates are the same, while for the $O(2)$ method we run $10^6 \times L$ updates for each of the three $O(2)$ unit circles, as described in the text. The inset has the same legend and shows the error bar on the CDW structure factor (to be defined in Section 4.4.1). These simulations are performed on lattices of size $L = 12$ and use model parameters $\lambda = 1$, $ga^2 = 0.35$, $g'a^2 = 0.00$, $wa^2 = -0.20$. These results also have a three-dimensional interlayer coupling $V_z = 0.1$ (to be defined in Section 4.6), although we expect similar results for the two-dimensional model of Equation (4.8).

where the C_{Φ_x} is calculated according to

$$C_{\Phi_x}(\mathbf{r}-\mathbf{r}') = \left\langle \sum_{\alpha=3}^{4} n_\alpha(\mathbf{r})\, n_\alpha(\mathbf{r}') \right\rangle . \tag{4.18}$$

As discussed in Section 4.1, the experimental curve in Figure 4.2 is produced by scanning in reciprocal space and extracting the peak scattering intensity for each value of T. Consequently, we compare this experimental curve with the peak value of $S_{\Phi_x}(\mathbf{q})$ as a function of $\mathbf{q}$. For the model of Equation (4.8), this peak occurs when $\mathbf{q} = 0$. We thus define $S_{\Phi_x} \equiv S_{\Phi_x}(\mathbf{q}=0)$ for all that follows.

On a two-dimensional translationally-invariant square lattice, the structure factor can in principle be calculated relative to any reference lattice site j as

$$S_{\Phi_x,j} = a^2 \sum_i \left\langle \sum_{\alpha=3}^{4} n_{i\alpha}\, n_{j\alpha} \right\rangle . \tag{4.19}$$

Averaging over all possible reference sites j then gives

$$\begin{aligned} S_{\Phi_x} &= \frac{1}{N_{\text{sites}}} \sum_j S_{\Phi_x,j} \\ &= \frac{a^2}{N_{\text{sites}}} \sum_{i,j} \left\langle \sum_{\alpha=3}^{4} n_{i\alpha}\, n_{j\alpha} \right\rangle . \end{aligned} \tag{4.20}$$

Since this formula involves a double sum $\sum_{i,j}$, measuring S_{Φ_x} using this expression requires a runtime that scales with N_{sites} as $\mathcal{O}(N_{\text{sites}}^2)$. However, one can reduce the runtime to $\mathcal{O}(N_{\text{sites}})$ by noting that the above expression can be rewritten as

$$S_{\Phi_x} = \frac{a^2}{N_{\text{sites}}} \left\langle \sum_{\alpha=3}^{4} \left(\sum_i n_{i\alpha} \right)^2 \right\rangle . \tag{4.21}$$

In Figure 4.9, we compare the CDW structure factors measured within our Monte Carlo simulations for various model parameters with experimental resonant soft x-ray scattering data for $\text{YBa}_2\text{Cu}_3\text{O}_{6.67}$ [81]. For each set of parameters, we employ a fitting procedure with

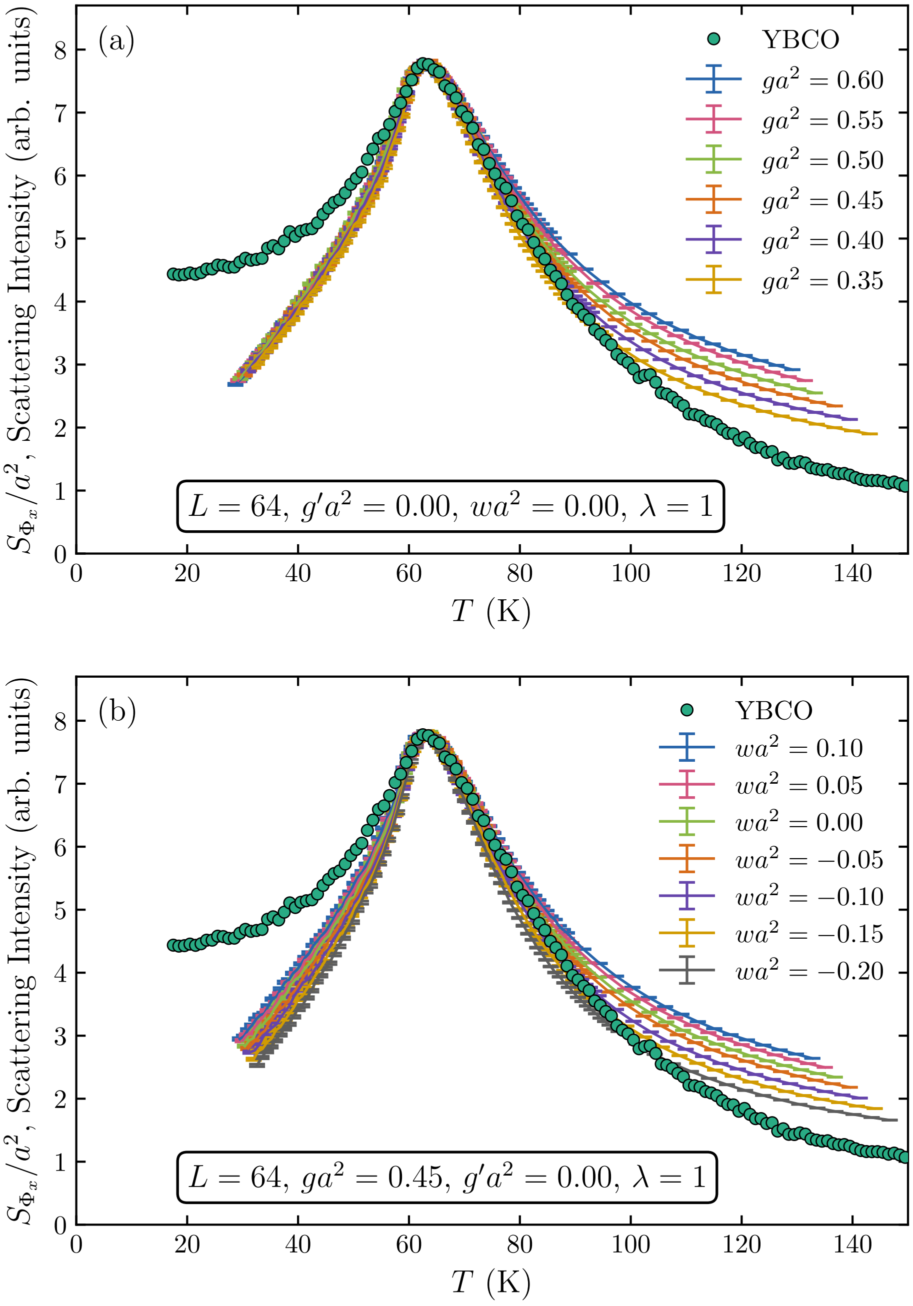

Figure 4.9: Comparison of experimental scattering intensities with the structure factors S_{Φ_x}/a^2 calculated using Monte Carlo simulations of the model in Equation (4.8) for (a) various values of g and (b) various values of w. Scattering intensities are obtained through resonant soft x-ray scattering experiments on $\mathrm{YBa_2Cu_3O_{6.67}}$ [81].

two free parameters whereby we rescale (but do not shift) the horizontal and vertical axes of our Monte Carlo results such that the location of the peak CDW structure factor matches with the location of the peak found in experimental. Rescaling the horizontal (temperature) axis amounts to determining the model parameter ρ_s. Such a fitting procedure does not have the freedom to modify peak shape nor the ratio of the peak width to the peak height.

The fits in Figure 4.9 show that our model is capable of reproducing the experimental scattering intensities corresponding to CDW order within the vicinity of the peak in S_{Φ_x}. While there are discrepancies between our Monte Carlo results and the experimental data both at high and at low temperatures, we emphasize that our model was designed with a focus on describing the pseudogap regime, and such discrepancies are expected. Specifically, at high T, our model's assumption that one can ignore amplitude fluctuations of the order parameter $\hat{\mathbf{n}}_i$ becomes invalid. Such amplitude fluctuations would lead to a lower expected magnitude of $\mathbf{n}_i$ at high temperatures (corresponding to a lack of local order), and are thus expected to reduce S_{Φ_x}, as required to achieve better agreement with experiment. In the limit of low temperatures, on the other hand, our model predicts that $S_{\Phi_x} \to 0$ as $T \to 0$. However, the experimental results indicate a finite value of S_{Φ_x} in this limit, which can likely be attributed to charge-order pinning due to impurities. As we will see in Section 4.6, incorporating random-field disorder into our model can help to resolve this discrepancy.

4.4.2 Superconducting phase transition

Within the model described by Equation (4.8), the superconducting order Ψ_i undergoes a Berezinskii-Kosterlitz-Thouless (BKT) transition [82, 83, 84, 85, 86] with critical temperature T_c. Such a transition is attributed to the binding of vortex-antivortex pairs for temperatures below T_c and is known to satisfy the Nelson-Kosterlitz criterion [87] in the thermodynamic limit such that

$$\gamma_\mu(T_c) = \frac{2T_c}{\pi}, \tag{4.22}$$

where $\gamma_\mu(T)$ is the helicity modulus along lattice direction μ and $\mu = x$ or y.

On a periodic square lattice, the helicity modulus along the lattice direction μ is measured within a Monte Carlo simulation according to [88, 89, 90]

$$\gamma_\mu^{\mathrm{MC}}(T, L) = -\frac{1}{L^2}\left[\langle H_\mu \rangle + \frac{1}{T}\left\langle I_\mu^2 \right\rangle\right], \tag{4.23}$$

where H_μ is the order's contribution to the Hamiltonian from nearest neighbours along the lattice direction μ and I_μ is the order's current along lattice direction μ. In SC order undergoes the BKT transition and we thus define γ_μ^{MC} in terms of the components n_{i1} and n_{i2}. The expressions for H_μ and I_μ are given by [88, 89, 90]

$$\begin{aligned} H_\mu &= -\rho_s \sum_{\langle ij \rangle_\mu} \left(n_{i1} n_{j1} + n_{i2} n_{j2} \right), \\ I_\mu &= -\rho_s \sum_{\langle ij \rangle_\mu} \left(n_{i1} n_{j2} - n_{i2} n_{j1} \right), \end{aligned} \tag{4.24}$$

where the notation $\langle ij \rangle_\mu$ indicates that the corresponding sum is over nearest neighbours along the μ lattice direction.

It turns out that the quantity $\gamma_\mu^{\mathrm{MC}}(T, L)$ measured using Equation (4.23) within Monte Carlo simulation on finite lattices with PBC is not quite the same as the helicity modulus $\gamma_\mu(T)$ within Equation (4.22) [91]. This phenomenon is known as stiffness renormalization and it is present even when one uses finite-size scaling analysis to approach the thermodynamic limit $L \to \infty$. On an $L_x \times L_y$ lattice with aspect ratio $b = L_x/L_y$, the quantities γ_μ^{MC} and γ_μ are related such that

$$\gamma_\mu^{\mathrm{MC}}(T_c, L_x \to \infty, L_y \to \infty) = f_\mu(b)\, \gamma_\mu(T_c), \tag{4.25}$$

where $f_x \neq f_y$ except in the case where $b = 1$. The quantities f_x and f_y were calculated for various aspect ratios in Reference [92]. Our present calculations are performed on lattices with $b = 1$, for which $f_x = f_y = f \approx 0.9998247$ [91]. The Nelson-Kosterlitz criterion corresponding to our calculations is therefore modified for finite-lattice calculations such that

$$\gamma_\mu^{\mathrm{MC}}(T_c, L \to \infty) = \frac{2f\, T_c}{\pi}. \tag{4.26}$$

In Figure 4.10, we plot $\gamma_\mu^{\mathrm{MC}}(T_c, L)$ as a function of temperature for various lattice lengths L and a given set of model parameters. We also plot the line $2fT/\rho_s$ since, according to Equation (4.26), this line should intersect with γ_μ^{MC} at $T = T_c$ in the thermodynamic limit $L \to \infty$.

In order to properly approach the thermodynamic limit from our finite lattice calculation, we utilize the relationship

$$\gamma_\mu^{\mathrm{MC}}(T_c, L) = \gamma_\mu^{\mathrm{MC}}(T_c, L \to \infty)\, F(L), \tag{4.27}$$

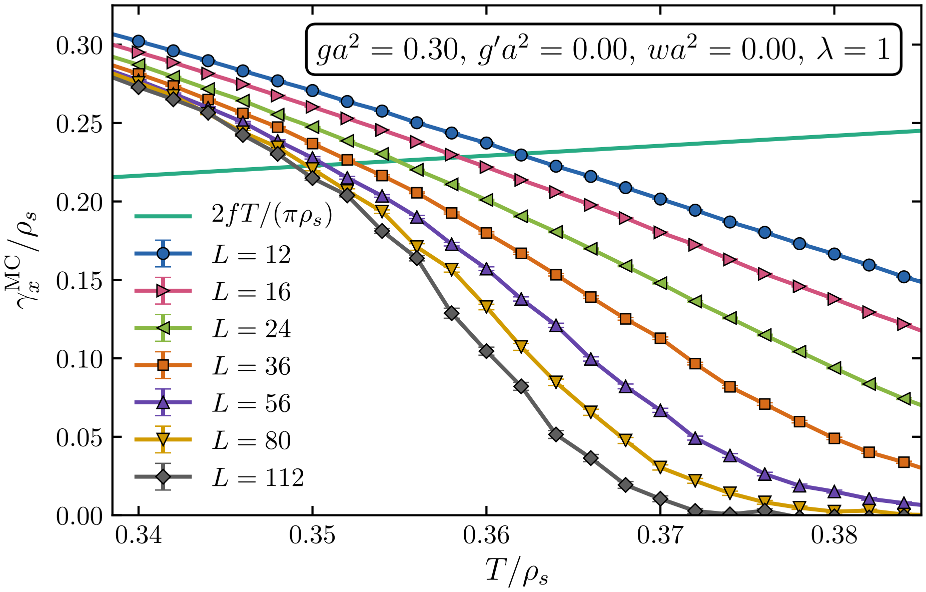

Figure 4.10: The helicity modulus γ_x^{MC} corresponding to the superconducting order as a function of temperature for various lattice sizes. The helicity modulus is calculated along the x lattice direction using Equation (4.23). The solid line corresponds to the Nelson-Kosterlitz criterion in Equation (4.26).

where the function $F(L)$ is given to leading order in L by [93, 94]

$$F(L) = 1 + \frac{g}{2\ln(L) + C} \tag{4.28}$$

with $g \approx 1.00202783$. Following the procedure outlined in Reference [95], we then extract the critical temperature T_c by solving for the parameters T^* and C in the set of equations

$$\frac{\gamma_\mu^{\mathrm{MC}}(T^*, L_1)}{F(L_1)} = \frac{\gamma_\mu^{\mathrm{MC}}(T^*, L_2)}{F(L_2)} = f\frac{2T^*}{\pi}, \tag{4.29}$$

where the relationship between the lattices sizes L_1 and L_2 can be chosen arbitrarily. In our analysis, we use $L_1 = L$ and $L_2 = 2L_1$ as in Reference [95]. Since $F(L) \to 1$ as $L \to \infty$, the value of $T^*(L)$ extracted from Equation (4.29) is expected to approach the critical temperature T_c in the thermodynamic limit. As illustrated in Figure 4.11, the values of $T^*(L)$ corresponding to our Monte Carlo data show no clear trend as a function of L, and we conclude that finite-size scaling behaviour of $T^*(L)$ is obscured due to the relatively large error bars on our Monte Carlo data. We therefore estimate T_c and its error bar ΔT_c

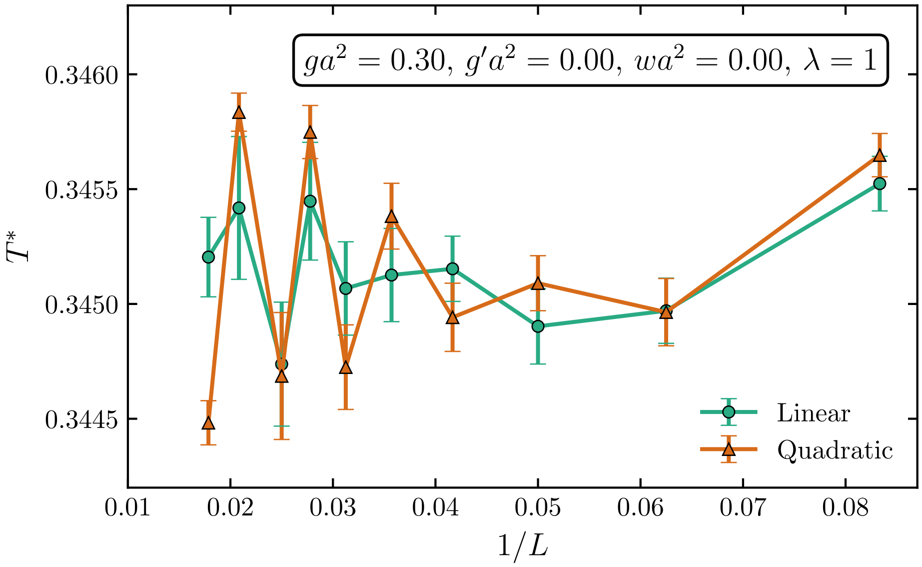

Figure 4.11: The value for T^* extracted from solving Equation (4.29) for various lattice sizes L. In order to solve this equation, we first interpolate the Monte Carlo results for $\gamma_x(T, L)/\rho_s$ as a function of T. We show results for T^* corresponding to both linear and quadratic interpolation.

from the extrema $T^*_{\text{min}} = \min\{T^*(L) - \Delta T^*(L)\}$ and $T^*_{\text{max}} = \max\{T^*(L) + \Delta T^*(L)\}$ such that

$$\begin{aligned} T_c &= \frac{T^*_{\text{min}} + T^*_{\text{max}}}{2} \\ \Delta T_c &= \frac{T^*_{\text{max}} - T^*_{\text{min}}}{2}. \end{aligned} \tag{4.30}$$

These equations predict that $T_c/\rho_s = 0.3451(8)$ for the case where the model parameters are given by $ga^2 = 0.30$, $g'a^2 = 0.00$, $wa^2 = 0.00$ and $\lambda = 1$.

We now compare this extracted value for T_c/ρ_s with the location T_{peak} of the peak in the CDW structure factor. As shown in Figure 4.12, we find that the superconducting transition occurs at a lower temperature than T_{peak}. This observation is consistent the theory presented in Reference [96], which predicted that the charge order increases within the cuprate superconductors as one increases T through T_c. However, this observation contradicts x-ray experiments [75, 76, 77, 97, 98], which find that the superconducting transition occurs very close to the peak CDW structure factor such that $T_c \approx T_{\text{peak}}$. While the numerical results in this section are for a strictly two-dimensional model, we will see

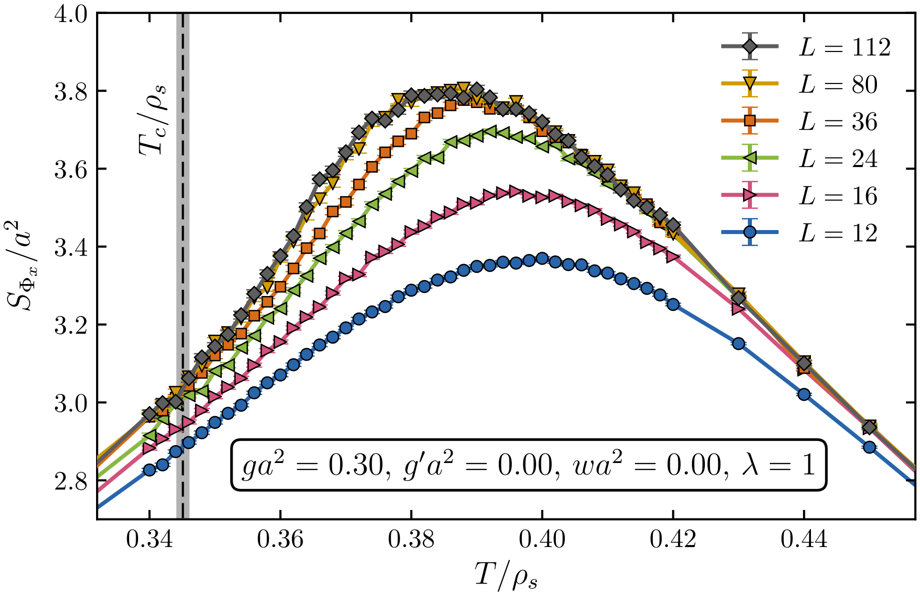

Figure 4.12: Comparison of the SC transition temperature T_c with the location T_{peak} of the peak in the CDW structure factor S_{Φ_x}/a^2 for various lattice sizes L. The vertical dashed line corresponds to T_c with the gray shading corresponding to the approximate error ΔT_c. Our Monte Carlo simulations find that $T_c < T_{\text{peak}}$.

in Section 4.6 that adding an interlayer coupling (such that the model becomes three-dimensional) causes T_c to approach T_{peak}, as required to achieve better agreement with experiments.

4.5 Diamagnetism and charge-density wave order

As discussed in Section 4.2, the competition between SC and CDW orders plays a significant role in controlling the behaviour observed in the pseudogap. As a result, the pseudogap can be characterized in terms of experiments that probe either SC or CDW fluctuations. In particular, strong SC fluctuations lead to a large diamagnetic susceptibility χ_{d} above the superconducting critical temperature [99, 100, 101, 102], while strong CDW correlations with correlation length ξ_{CDW} have been measured through x-ray scattering experiments [75, 76, 77, 103, 104, 81, 105]. As shown in Section 4.4.1, the model in Equation (4.8) produces good agreement with such experimental CDW correlations.

With the goal of reconciling the distinct experimental probes χ_{d} and ξ_{CDW}, we now introduce a new, experimentally-accessible dimensionless quantity, given by

$$R(T) = 12\pi s \frac{12\pi s \chi_{\mathrm{d}}}{T\,\xi_{\mathrm{CDW}}^2}, \tag{4.31}$$

where s is the interlayer lattice spacing. The susceptibility can be written as $\chi_{\mathrm{d}} = M/B$, where M is the magnetization per unit volume in the case where a magnetic field B is applied perpendicular to the two-dimensional copper-oxygen planes. Since this quantity incorporates the effects of both SC and CDW fluctuations, it is in principle capable of characterizing the pseudogap more completely than experiments that probe only one type of these two competing orders.

4.5.1 Diamagnetic susceptibility measurement

In order to calculate the diamagnetic response of our model in Equation (4.8) to an applied magnetic field B, we introduce an external vector potential that couples to the superconducting order $\Psi_i = n_{i1} + in_{i2} \equiv |\Psi_i|\, e^{i\theta_i}$. We let H_Ψ correspond to the portion of the nearest-neighbour coupling term H_1 in Equation (4.6) that depends on the superconducting order such that

$$\begin{aligned} H_\Psi &= \frac{\rho_s}{2} \sum_{\langle ij \rangle} \sum_{\alpha=1}^{2} (n_{i\alpha} - n_{j\alpha})^2 \\ &= \frac{\rho_s}{2} \sum_{\langle ij \rangle} |\Psi_i - \Psi_j|^2 \\ &= \frac{\rho_s}{2} \sum_{\langle ij \rangle} \left[|\Psi_i|^2 + |\Psi_j|^2 - 2\,|\Psi_i|\,|\Psi_j| \cos(\theta_i - \theta_j) \right]. \end{aligned} \tag{4.32}$$

Adding a vector potential then amounts to adding a phase factor (or bond flux) $A_{ij} = -A_{ji}$ to every nearest-neighbour bond such that [106, 107, 108]

$$\begin{aligned} H_\Psi \to H_\Psi(A) &= \frac{\rho_s}{2} \sum_{\langle ij \rangle} \left[|\Psi_i|^2 + |\Psi_j|^2 - 2\,|\Psi_i|\,|\Psi_j| \cos(\theta_i - \theta_j + A_{ij}) \right] \\ &= \frac{\rho_s}{2} \sum_{\langle ij \rangle} \left[|\Psi_i|^2 + |\Psi_j|^2 - \Psi_i^* \Psi_j e^{iA_{ij}} - \Psi_j^* \Psi_i e^{-iA_{ij}} \right]. \end{aligned} \tag{4.33}$$

Now, instead of labelling by the two site indices i and j in the above equation, it is convenient to label by one site index i along with a lattice direction $\mathbf{u}$. On a two-dimensional lattice, $\mathbf{u}$ can in general extend over $\pm\hat{\mathbf{x}}a$ and $\pm\hat{\mathbf{y}}a$ (although it maybe extend over a more restricted range for sites on the boundary of a lattice with open boundary conditions). With this new notation, we can express $H_\Psi(A)$ as

$$\begin{aligned} H_\Psi(A) &= \frac{\rho_s}{2}\left[\sum_i Z_i \left|\Psi_i\right|^2 - \sum_{i,\mathbf{u}} \Psi_i^* \Psi_{i+\mathbf{u}} e^{iA_{i\mathbf{u}}}\right] \\ &= \frac{\rho_s}{2}\left[\sum_i Z_i \left|\Psi_i\right|^2 - \sum_{i,\mathbf{u}} \Psi_{i+\mathbf{u}}^* \Psi_i e^{-iA_{i\mathbf{u}}}\right], \end{aligned} \tag{4.34}$$

where Z_i is the called the coordination number of site i, which is the number of nearest neighbours that site i has. In this new notation, the elements $A_{i\mathbf{u}}$ are restricted such that $A_{i+\mathbf{u},-\mathbf{u}} = -A_{i\mathbf{u}}$. The current along link $i\mathbf{u}$ corresponding to this external vector potential is then given by

$$\mathbf{J}_{i\mathbf{u}} = \frac{\rho_s}{2}\left(i\Psi_i^*\Psi_{i+\mathbf{u}}e^{iA_{i\mathbf{u}}} - i\Psi_i\Psi_{i+\mathbf{u}}^*e^{-iA_{i\mathbf{u}}}\right)\mathbf{u}. \tag{4.35}$$

From this expression for the current, one can calculate the total magnetic moment per unit volume according to [106]

$$\begin{aligned} M &= \frac{1}{4L^2a^2s}\left|\sum_{i,\mathbf{u}} \mathbf{r}_i \times \left\langle \mathbf{J}_{i\mathbf{u}} \right\rangle\right| \\ &= \frac{\rho_s}{4L^2a^2s}\sum_{i,\mathbf{u}} \epsilon_{\alpha\beta} r_{i\alpha} u_\beta \left\langle i\Psi_i^*\Psi_{i+\mathbf{u}}e^{iA_{i\mathbf{u}}}\right\rangle, \end{aligned} \tag{4.36}$$

where $\epsilon_{\alpha\beta}$ is the two-dimensional Levi-Civita symbol and we have employed the Einstein summation convention over the indices α and β. We assume that the lattice length L is even and define the site coordinates $\mathbf{r}_i$ relative to an origin at the centre of the lattice's middle plaquette such that

$$\mathbf{r}_i \equiv (x_i, y_i) = \left(i_x - \frac{L+1}{2}, i_y - \frac{L+1}{2}\right)a, \tag{4.37}$$

where $i_{x,y} \in \{1, 2, \ldots, L\}$ are indices that label the x and y coordinates (respectively) in units of the lattice spacing a. We assume that the external magnetic field $\mathbf{B}$ is applied perpendicular to the two-dimensional lattice plane and specify the relationship between this field and the vector potential in the circular gauge such that

$$A_{i\mathbf{u}} = \frac{B}{2}\epsilon_{\alpha\beta} r_{i\alpha} u_{\beta}. \tag{4.38}$$

Previous works have performed calculations of the diamagnetic response on a lattice with cylindrical boundary conditions, which results in a quantized magnetic flux through the lattice. [107, 108]. In the calculations that follow, we consider lattices with open boundary conditions (OBC) such that we can take the limit where $B \to 0$. In this limit, one can calculate the linear diamagnetic susceptibility $\chi_{\mathrm{d}} = M/B$ by expanding the expression for the magnetic moment M in Equation (4.36) to first order in B, which gives

$$\begin{aligned}\chi_{\mathrm{d}} = M/B = &-\frac{\rho_s}{8L^2a^2s}\sum_{i,\mathbf{u}}\left(\epsilon_{\alpha\beta} r_{i\alpha} u_{\beta}\right)^2 \left\langle \Psi_i^* \Psi_{i+\mathbf{u}}\right\rangle_0 \\ &+ \frac{\rho_s^2}{16TL^2a^2s}\sum_{i,\mathbf{u}}\sum_{j,\mathbf{u}'}\left(\epsilon_{\alpha\beta} r_{i\alpha} u_{\beta}\right)\left(\epsilon_{\gamma\delta} r_{j\gamma} u'_{\delta}\right)\left\langle \Psi_i^* \Psi_{i+\mathbf{u}} \Psi_{j+\mathbf{u}'}^* \Psi_j\right\rangle_0 ,\end{aligned} \tag{4.39}$$

where the subscript 0 means that these expectation values are calculated in a model with zero field B. Alternatively, this expression can be written in terms of the components n_{i1} and n_{i2} as [70]

$$\begin{aligned}\chi_{\mathrm{d}} \equiv \frac{M}{B} = &-\frac{\rho_s}{4L^2a^2s}\sum_{i}\sum_{\mathbf{u}=+\hat{\mathbf{x}}a,+\hat{\mathbf{y}}a}\left(\epsilon_{\alpha\beta} r_{i\alpha} u_{\beta}\right)^2 \left\langle n_{i1} n_{i+\mathbf{u},1} + n_{i2} n_{i+\mathbf{u},2}\right\rangle_0 \\ &+ \frac{\rho_s^2}{4TL^2a^2s}\left\langle\left[\sum_{i}\sum_{\mathbf{u}=+\hat{\mathbf{x}}a,+\hat{\mathbf{y}}a}\left(\epsilon_{\alpha\beta} r_{i\alpha} u_{\beta}\right)\left(n_{i1} n_{i+\mathbf{u},2} - n_{i2} n_{i+\mathbf{u},1}\right)\right]^2\right\rangle_0 ,\end{aligned} \tag{4.40}$$

where we set $n_{i+u,\alpha} = 0$ in all cases where site i has no nearest neighbour in along the $\mathbf{u}$ direction due to the open boundary conditions. Note that the expression in Equation (4.40) involves only single sums over the lattice sites i such that the measurement runtime scales linearly with N_{sites} as $\mathcal{O}(N_{\text{sites}})$, as opposed to the quadratic runtime $\mathcal{O}(N_{\text{sites}}^2)$ that would result from naively evaluating Equation (4.39).

In order to verify that that the expression in Equation (4.40) provides a valid way of accessing the diamagnetic susceptibility for a system with OBC in the limit of arbitrarily small fields B, we first measure this expression in a simple Gaussian model, for which exact analytical results are known in the thermodynamic limit $L \to \infty$. After establishing agreement, we then proceed to measure this observable within simulations corresponding to the more complicated model of Equation (4.8).

4.5.2 Diamagnetic susceptibility in a Gaussian theory

We consider here simple a Gaussian theory that ignores all four CDW components of the order parameter $\mathbf{n}_i$ and neglects any constraints on the magnitude of $\mathbf{n}_i$. Such a simple theory considers only the SC order parameter Ψ_i such that the partition function is given by

$$\mathcal{Z}_{\mathrm{Gauss.}} = \int \mathcal{D}\Psi \, \exp\left(-\beta H_{\mathrm{Gauss.}}\right), \tag{4.41}$$

with Hamiltonian [70]

$$\begin{aligned} H_{\mathrm{Gauss.}} &= \frac{\rho_s}{2}\left[\sum_{\langle ij\rangle} \left|\Psi_i - \Psi_j\right|^2 + \sum_i \overline{\sigma} a^2 \left|\Psi_i\right|^2\right] \\ &= \frac{\rho_s}{2}\left[\sum_i \left(Z_i + \overline{\sigma} a^2\right)\left|\Psi_i\right|^2 - \sum_{i,\mathbf{u}} \Psi_i^* \Psi_{i+\mathbf{u}}\right] \\ &\equiv \frac{\rho_s}{2}\sum_{i,j} \Psi_i^* \mathcal{M}_{ij} \Psi_j, \end{aligned} \tag{4.42}$$

where $\overline{\sigma}$ is a constant and $\mathcal{M}$ is a symmetric matrix that is defined by the terms in the Hamiltonian. The inverse of this matrix can be used to calculate the two-point correlation functions according to $\left\langle \Psi_i \Psi_j^* \right\rangle = (2T/\rho_s)\mathcal{M}^{-1}_{ij}$. We consider a lattice with OBC such that the coordination number Z_i has a value of 4 within the bulk, 3 along the edges of the lattice, and 2 at the lattice's four corners.

By exploiting Wick's theorem, it is then possible to calculate χ_{d} from Equation (4.39) using the elements of $\mathcal{M}^{-1}$ such that

$$\frac{\chi_{\mathrm{d}}}{T} = \frac{1}{4L^2 a^2 s}\left[-\sum_{i,\mathbf{u}} \left(\epsilon_{\alpha\beta} r_{i\alpha} u_\beta\right)^2 \mathcal{M}^{-1}_{i,i+\mathbf{u}} + \sum_{i,\mathbf{u}}\sum_{j,\mathbf{u}'} \left(\epsilon_{\alpha\beta} r_{i\alpha} u_\beta\right)\left(\epsilon_{\gamma\delta} r_{j\gamma} u'_\delta\right) \mathcal{M}^{-1}_{ij} \mathcal{M}^{-1}_{j+\mathbf{u}',i+\mathbf{u}}\right], \tag{4.43}$$

where we note that the right-hand side of this expression is independent of both ρ_s and T.

In the thermodynamic limit $L \to \infty$, this expression can be written as [60]

$$\frac{\chi_{\mathrm{d}}(L\to\infty)}{T} = -\frac{1}{a^6 s}\int \frac{\mathrm{d}^2\mathbf{k}}{4\pi^2}\, \frac{8\sin^2(k_x a)\sin^2(k_y a)}{\left[\left(4 - 2\cos(k_x a) - 2\cos(k_y a)\right)/a^2 + \overline{\sigma}\right]^4}, \tag{4.44}$$

which reduces to $-1/(12\pi\overline{\sigma}a^2 s)$ in the limit where $\overline{\sigma} \to 0$.

We now consider Monte Carlo measurements of χ_{d} on systems with OBC with the goal of comparing such numerical results with the expressions in Equations (4.43) and (4.44). In order to more directly utilize Monte Carlo methods from Chapter 3 and Section 4.3.2, we first write the Gaussian Hamiltonian in terms of $\mathbf{n}_i \equiv (n_{i1}, n_{i2})$ as

$$H_{\mathrm{Gauss.}} = \rho_s \left[\frac{1}{2} \sum_i \left(Z_i + \overline{\sigma} a^2 \right) |\mathbf{n}_i|^2 - \sum_{\langle ij \rangle} \mathbf{n}_i \cdot \mathbf{n}_j \right]. \tag{4.45}$$

We note that the second term is the Hamiltonian for the $O(2)$ model of Equation (1.2). One can sample this Hamiltonian by using local updates that are similar to those in Algorithm 3.1 but with the new orientations for the components of $\mathbf{n}_i$ selected from a normal distribution with standard deviation $\sqrt{T/\left[\rho_s(Z_i + \overline{\sigma}a^2)\right]}$ so as to respect the detailed balance condition corresponding to the first term in Equation (4.45). The complete sampling method is given in Algorithm 4.2.

Algorithm 4.2: Local sampling algorithm for the Gaussian Hamiltonian in Equation (4.45).

```
choose a site $i$ from the lattice at random;
choose a random new orientation $\mathbf{n}_{\mathrm{new}} = (n_{\mathrm{new},1}, n_{\mathrm{new},2})$ for the spin at
  this location by generating $n_{\mathrm{new},1}$ and $n_{\mathrm{new},2}$ from a normal distribution
  with mean 0 and standard deviation $\sqrt{T/\left[\rho_s(Z_i + \overline{\sigma}a^2)\right]}$;
calculate the energy difference $\Delta E_{\mathrm{n.n.}}$ associated with changing the
  current spin orientation $\mathbf{n}_i$ to $\mathbf{n}_{\mathrm{new}}$, where $E_{\mathrm{n.n.}} = -\sum_{\langle ij \rangle} \mathbf{n}_i \cdot \mathbf{n}_j$ is the
  energy corresponding to the nearest-neighbour coupling;
if  $\Delta E_{\mathrm{n.n.}} \leq 0$ then
    accept the move $\mathbf{n}_i \to \mathbf{n}_{\mathrm{new}}$;
else
    accept the move $\mathbf{n}_i \to \mathbf{n}_{\mathrm{new}}$ with probability $\exp(-\beta \Delta E_{\mathrm{n.n.}})$;
end
```

In Table 4.2, we compare the exact results of Equations (4.43) and (4.44) with measurements of the diamagnetic susceptibility χ_{d} from Monte Carlo simulations on finite lattices of length L. We achieve agreement with the exact results for $L \to \infty$, which indicates that these Monte Carlo methods are capable of successfully accessing χ_{d} in the thermodynamic limit.

4.5.3 Diamagnetic susceptibility for the effective classical Hamiltonian

We now consider Monte Carlo measurements of the diamagnetic susceptibility χ_{d} as given in Equation (4.40) for the effective theory of Equation (4.8). Results are shown in Figure 4.13 for various lattices lengths L for a given set of model parameters. In the inset of this figure, we study the convergence of χ_{d} as L increases. We find that, for temperatures above T_c, the diamagnetic susceptibility converges to a constant value as $L \to \infty$ (or, equivalently, as $1/L \to 0$). However, for temperatures below the superconducting critical temperature, there is no such convergence to a finite value.

In fact, a simple model of the superconducting phase [70] predicts that

$$\frac{s\chi_{\mathrm{d}}(T < T_c)}{\gamma_x^{\mathrm{PBC}} L^2} = -0.03514425, \tag{4.46}$$

where γ_x^{PBC} is the helicity modulus, as defined in Equation (4.23). This helicity modulus must be measured on a lattice with PBC since it will be zero for the lattices with OBC that are used to calculate the diamagnetic susceptibility. We therefore must measure χ_{d} and γ_x^{PBC} in separate Monte Carlo simulations. In Figure 4.14, we plot the left-hand side of Equation (4.46) as a function of temperature. In its inset, we perform fits of $s\chi_{\mathrm{d}}/(\gamma_x^{\mathrm{PBC}} L^2)$ to a quadratic polynomial in $1/L$. These fits show that Equation (4.46) is satisfied for temperatures below T_c in the thermodynamic limit $L \to \infty$.

We note that Equation (4.46) states that the diamagnetic susceptibility diverges to $-\infty$ as $L \to \infty$. This divergence corresponds to the phenomenon known as the Meissner effect whereby magnetic fields are expelled from materials that are in a superconducting state.

$\overline{\sigma}$	L	$s\chi_{\mathrm{d}}/T$ Equation (4.43)	$s\chi_{\mathrm{d}}/T$ Equation (4.44)	Monte Carlo
1	5	-0.011490		-0.01149(2)
1	10	-0.011206		-0.01124(5)
1	20	-0.011108		-0.0110(2)
1	40	-0.011064		-0.0113(6)
1	80	-0.011043		-0.010(2)
1	∞	-0.011028(3)	-0.011024	-0.0108(4)
0.5	5	-0.038279		-0.03826(2)
0.5	10	-0.034226		-0.03426(5)
0.5	20	-0.032718		-0.0326(4)
0.5	40	-0.032004		-0.031(1)
0.5	80	-0.031656		-0.026(4)
0.5	∞	-0.03139(4)	-0.031315	-0.0308(9)
0.1	5	-0.420271		-0.404(4)
0.1	10	-0.322547		-0.320(2)
0.1	20	-0.268920		-0.275(6)
0.1	40	-0.247611		-0.24(1)
0.1	80	-0.237534		-0.18(3)
0.1	∞	-0.224(3)	-0.227827	-0.22(1)

Table 4.2: Linear diamagnetic susceptibility corresponding to the Gaussian Hamiltonian in Equation (4.42). The extrapolation to $L = \infty$ in the third and fifth columns is performed by a least-squares fit to a quadratic polynomial of $1/L$, and the error bars for $L = \infty$ come from the covariance matrix of the least-squares fit. The Monte Carlo data in the fifth column was taken at $T/\rho_s = 0.6$, although we also checked that the Monte Carlo results for $M/(BT)$ are independent of temperature. This Table is taken from Reference [70].

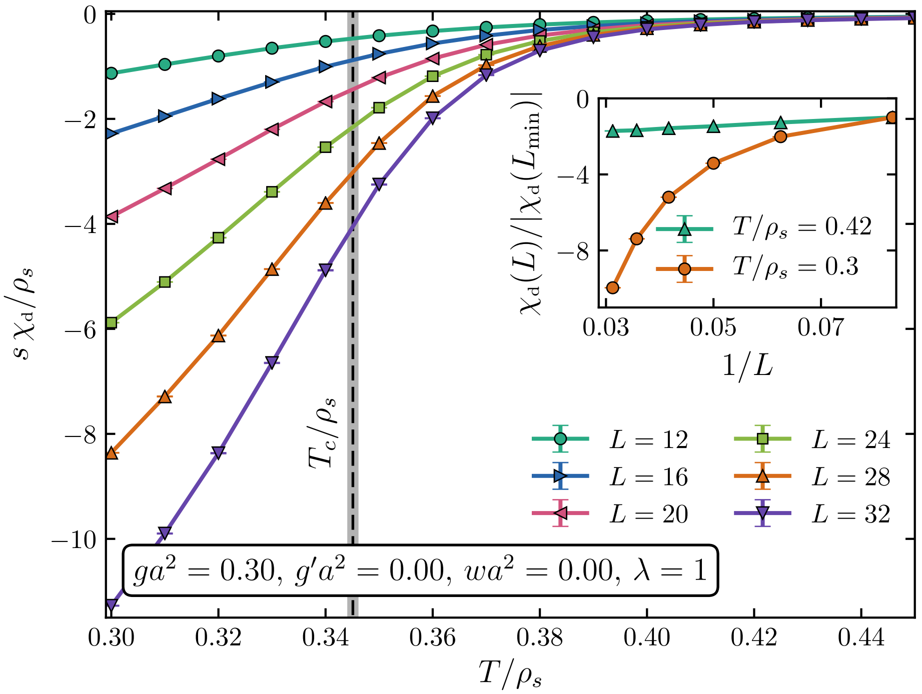

Figure 4.13: Diamagnetic susceptibility for the effective theory of Equation (4.8) as a function of temperature for various lattice sizes L. In the inset, we study the convergence of this susceptibility as a function of L for temperatures both above and below the superconducting critical temperature T_c.

4.5.4 Charge-density wave correlation length

We now consider methods for measuring the range of CDW correlations within our Monte Carlo simulations, with the ultimate goal of calculating the dimensionless ratio in Equation (4.31). As stated in Equation (1.17), we expect two-point correlation functions to experience an exponential decay with a characteristic length scale given by a correlation length ξ. Here, we focus specifically on correlations related to the CDW order and we examine the correlation length ξ_CDW corresponding to the CDW correlation function $C_{\Phi_x}(\mathbf{r}-\mathbf{r}')$ as given in Equation (4.18).

We examine the CDW structure factor $S_{\Phi_x}(\mathbf{q})$ as given in Equation (4.17) and take $\mathbf{q} = q_x\hat{\mathbf{x}}$. Such a structure is expected to behave according to a Lorentzian distribution. However, we find that such a function does not describe our data well unless we incorporate a shift

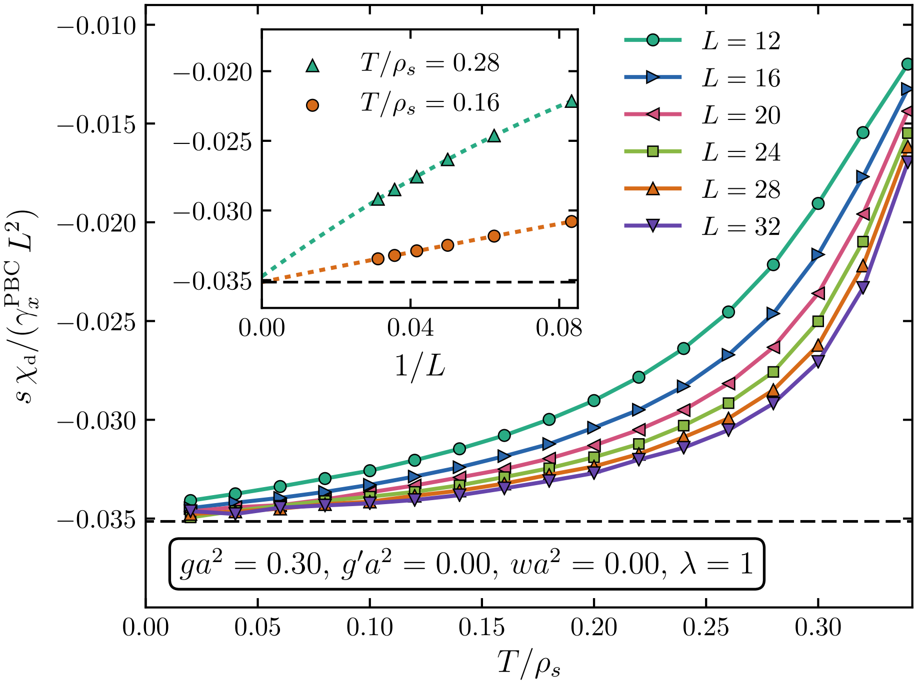

Figure 4.14: Convergence of the diamagnetic susceptibility for temperatures within the superconducting phase. We plot the quantity on the left-hand side of Equation (4.46) as a function of temperature and compare with the expected value from the right-hand side of this equation (which is indicated by a dashed black line). In the inset (which has the same y-axis as the main plot), we study this quantity as a function of $1/L$ for two different temperatures below T_c. We perform least-squares fits (indicated by the dotted lines) to a quadratic polynomial of $1/L$ and show that we achieve approximate agreement with Equation (4.46) as $1/L \to 0$.

c such that we fit to the shifted Lorentzian function

$$f(q_x) = \frac{A}{(q_x^2 + 1/\xi_{\text{CDW}}^2)} + c, \tag{4.47}$$

where the amplitude A, the shift c and the correlation length ξ_{CDW} are all free parameters within the least-squares fitting procedure.

We compare the results for ξ_{CDW} from this procedure with data obtained by following another method as described in Reference [90]. Specifically, this method calculates the correlation length from the structure factor evaluated at $q_x = 0$ and $q_x = 2\pi a/L$ according to

$$\xi_{\text{CDW}} = \frac{La}{2\pi}\sqrt{\left(\frac{8d}{(1+d)(3+d)}\right)\left(\frac{S_{\Phi_x}(0)}{S_{\Phi_x}(\frac{2\pi a}{L}\hat{\mathbf{x}})} - 1\right)}. \tag{4.48}$$

In Figure 4.15, we show results for ξ_{CDW} as extracted from our Monte Carlo data using these two methods. These methods give comparable results for a wide range of temperatures on a lattice of size $L = 24$. The error bars corresponding to the shifted Lorentzian fit come from the covariance matrix of the least-squares fitting procedure, while the error bars corresponding to the second method come from statistical Monte Carlo errors.

We also show in this figure the CDW correlation length as extracted from x-ray scattering experiments on $\text{YBa}_2\text{Cu}_3\text{O}_{6.67}$ with $T_c = 65.5\,\text{K}$ [81]. The experimental predictions for $\xi_{\text{CDW}}^{\text{x-ray}}$ are extracted by first subtracting off the fluorescence background (from measurements at $T = 160\,\text{K}$) and then performing a fit of the scattering intensity to an (unshifted) Lorentzian function. The error bars in this case reflect uncertainties in the background subtraction as well as uncertainties in the fitting procedure.

We note that our Monte Carlo data corresponds to a CDW correlation length on the order of 1 to 2.5 lattice spacings a, while the experiments detect correlation lengths of approximately 5 to 50 Å. These measurements give us a rough idea of the ratio between the lattice spacing a corresponding to the square lattice in the effective theory and the physical lattice parameters a_{phys}, b_{phys} and c_{phys} corresponding to YBCO materials (see Figure 4.1). We find that a is approximately 3 to 5 times the size of the physical lattice parameter a_{phys}.

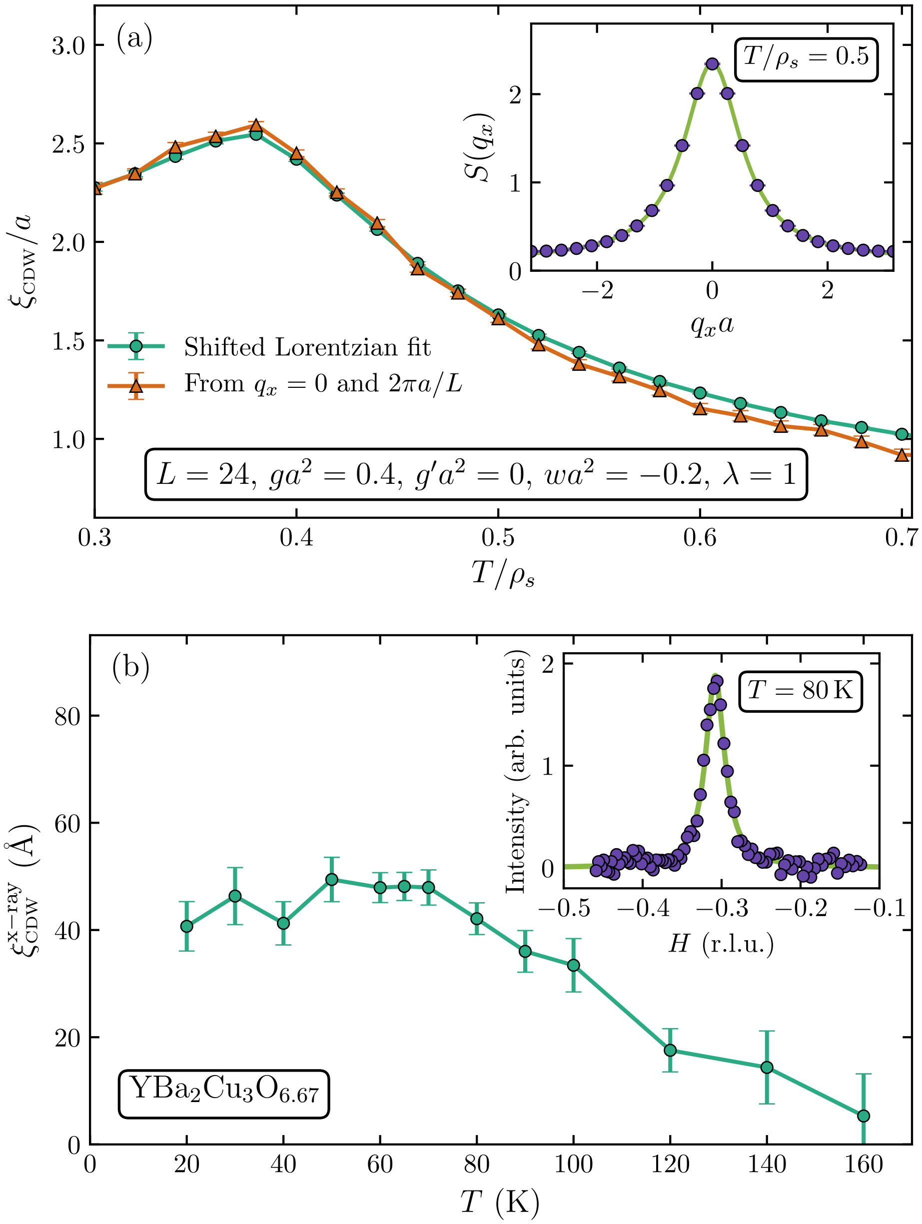

Figure 4.15: The charge-density wave correlation length as extracted from (a) Monte Carlo simulations [70] and (b) x-ray scattering experiments [81]. The inset in each case illustrates the fitting procedure for a given temperature. The quantity H in the inset of (b) corresponds to $\mathbf{q} = (H\ \ 0\ \ 1.48)$.

4.5.5 Comparisons with experimental dimensionless ratios

With the results for the diamagnetic susceptibility χ_{d} from Section 4.5.3 along with the results for the CDW correlation length ξ_{CDW} from Section 4.5.4, we can now compute the dimensionless ratio $R(T)$ in Equation (4.31). The Monte Carlo simulations for measuring χ_{d} are performed on lattices with OBC, while the ξ_{CDW} is calculated on lattices with OBC.

Experimentally, CDW correlation length is measured through x-ray scattering experiments as discussed in Section 4.5.4. The diamagnetic susceptibility is extracted through torque magnetometry experiments on $\mathrm{YBa_2Cu_3O_{6.5}}$ with $T_c = 57\,\mathrm{K}$ [102]. Such experiments measure a torque density as a function of the angle between an applied magnetic field and the sample's copper-oxygen planes. The resulting diamagnetic susceptibility can be expressed as

$$\chi_{\mathrm{d}}^{\mathrm{torque}} = -\frac{T\left(\xi_{\mathrm{d}}^{\mathrm{torque}}\right)^2}{12\pi s}, \tag{4.49}$$

where $\xi_{\mathrm{d}}^{\mathrm{torque}}$ is a coherence length corresponding to fluctuations parallel to the copper-oxygen planes. The dimensionless ratio $R(T)$ can then be expressed experimentally in terms of a ratio between the length scales $\xi_{\mathrm{CDW}}^{\mathrm{x-ray}}$ and $\xi_{\mathrm{d}}^{\mathrm{torque}}$ as

$$R(T) = -\left(\frac{\xi_{\mathrm{d}}^{\mathrm{torque}}}{\xi_{\mathrm{CDW}}^{\mathrm{x-ray}}}\right)^2. \tag{4.50}$$

In order to compare our Monte Carlo results for $R(T)$ with such experimental data, we must first determine the value of ρ_s (corresponding to the overall temperature scale) for each set of model parameters λ, ga^2, $g'a^2$ and wa^2 in Equation (4.8). To do so, we examine the peak CDW structure factor $S_{\Phi_x} = S_{\Phi_x}(\mathbf{q} = 0)$ as a function of T and perform fits to x-ray scattering data as we did in Figure 4.9. This fitting procedure is illustrated on the left-hand side of Figure 4.16 for various choices of model parameters. We then compute and plot $R(T)$ as a function of T with no additional fitting parameters on the right-hand side of this figure and compare with experimental results [81, 102, 109].

These plots show good qualitative agreement with the experimental data for a wide range of temperatures above the superconducting critical temperature T_c. However, the Monte Carlo predictions corresponding to the effective theory in Equation (4.8) are consistently larger in magnitude than the observed experimental values. One significant source of possible errors is that the two experiments were performed on different samples of YBCO with different dopings and different critical temperatures. In addition, our effective theory

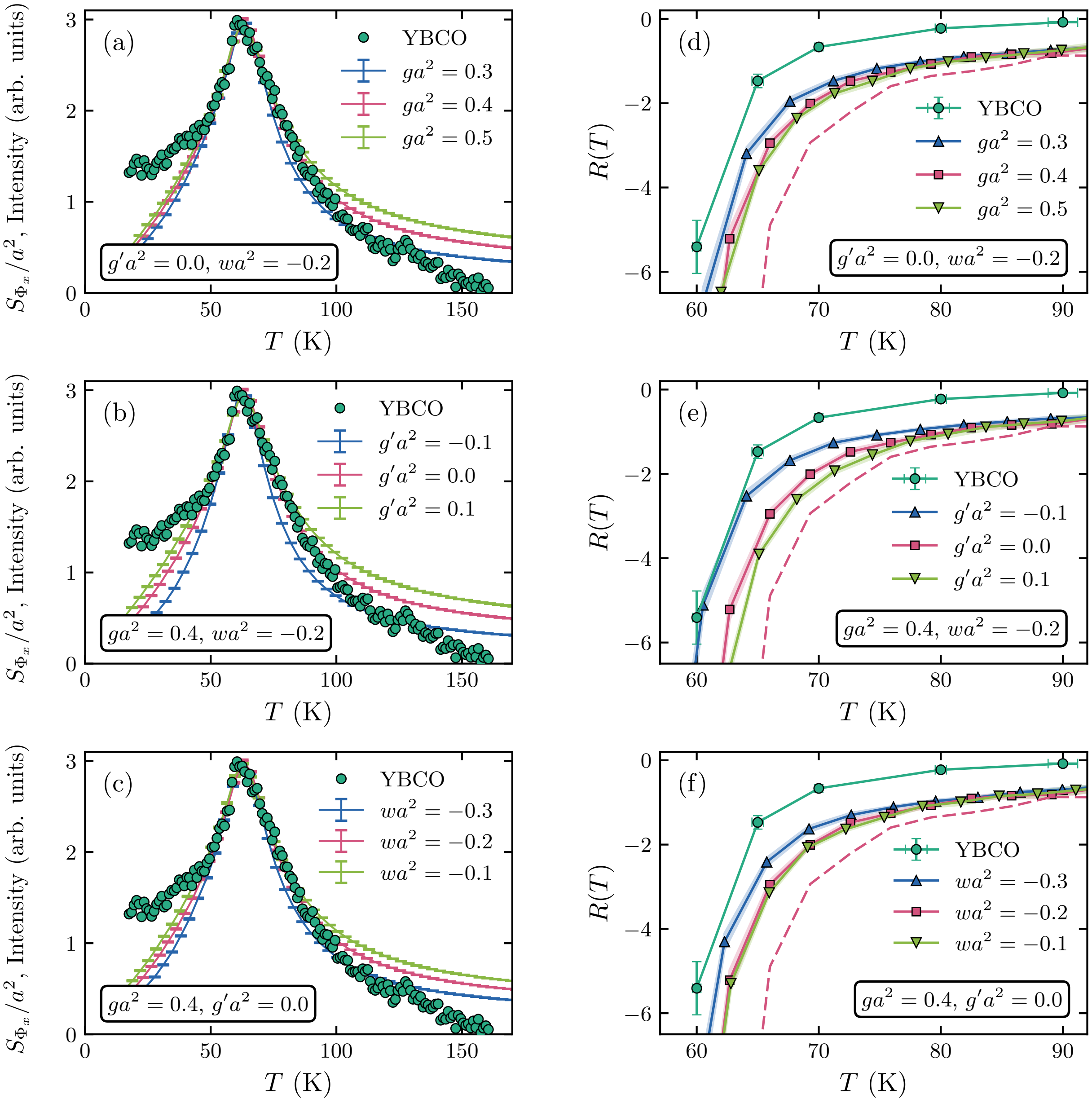

Figure 4.16: CDW structure factors and the dimensionless ratio $R(T)$ defined in Equation (4.31). In (a)-(c), we illustrate the fits used to determine the parameter ρ_s for various sets of model parameters. In (d)-(f), we show $R(T)$ versus T (with the shading incorporating statistical Monte Carlo errors as well as the uncertainty in the method for extracting ξ_{CDW}) for the same choices of parameters and compare with data from x-ray scattering [81] and torque magnetometry experiments [102, 109]. All Monte Carlo results correspond to $L = 24$ and $\lambda = 1$. The dashed lines in (d)-(f) correspond to an extrapolation to $L \to \infty$ for the model parameters $ga^2 = 0.4$, $g'a^2 = 0.0$, $wa^2 = -0.2$.

has certain limitations, as discussed in Section 4.4.1. In particular, the present model is two-dimensional such that it does not consider the interlayer coupling between copper-oxygen planes. Incorporating such an interlayer coupling (such that our model becomes three-dimensional) would help to reduce the strength of SC fluctuations above the critical temperature, which could help to lower the magnitude of $R(T)$ as required. We consider the effects of adding such an interlayer coupling in Section 4.6.

4.6 Improvements to the effective classical Hamiltonian

As seen from the comparisons with experimental data in Sections 4.4 and 4.5.5, the effective theory in Equation (4.8) suffers from certain limitations. In particular, we observe discrepancies in the value of T_c relative to the location T_{peak} of the peak in the CDW structure factor, as well as overly enhanced SC fluctuations that cause the magnitude of the dimensionless ratio $R(T)$ to be too large. In an attempt to combat these issues, here we consider the effects of a three-dimensional interlayer coupling. In addition, this model omits random-field disorder, and here we incorporate such disorder with the goal of yielding a finite value in the CDW structure factor S_{Φ_x} in the limit of low temperatures.

To this end, we now consider a new effective Hamiltonian on a three-dimensional square lattice given by [71]

$$\begin{aligned}\frac{H}{\rho_s} = &- \sum_{\langle ij\rangle_{xy}} \left[\sum_{\alpha=1}^{2} n_{i\alpha} n_{j\alpha} + \lambda \sum_{\alpha=3}^{6} n_{i\alpha} n_{j\alpha} \right] - \sum_{\langle ij\rangle_{z}} \left[V_z \sum_{\alpha=1}^{2} n_{i\alpha} n_{j\alpha} + V_z' \sum_{\alpha=3}^{6} n_{i\alpha} n_{j\alpha} \right] \\ &+ \frac{1}{2} \sum_i \left[\left[g a^2 + 4(\lambda - 1) \right] \sum_{\alpha=3}^{6} n_{i\alpha}^2 + g' a^2 \left(\sum_{\alpha=3}^{6} n_{i\alpha}^2 \right)^2 \right. \\ &\qquad \left. + w a^2 \left[\left(n_{i3}^2 + n_{i4}^2 \right)^2 + \left(n_{i5}^2 + n_{i6}^2 \right)^2 \right] + \frac{a^2}{2} \sum_{\alpha=3}^{6} h_{i\alpha} n_{i\alpha} \right],\end{aligned} \tag{4.51}$$

where the parameters ρ_s, λ, g, g', w and a are defined in the same way as in Equations (4.4) and (4.8). The notation $\langle ij\rangle_{xy}$ and $\langle ij\rangle_{z}$ indicates that the corresponding sums are over nearest-neighbours along the xy and z directions (respectively). The parameters V_z and V_z'

represent interlayer coupling strengths between between the xy planes, with V_z coupling the SC components of $\hat{\mathbf{n}}_i$ and V_z' coupling the CDW components. $h_{i\alpha}$ is a random field that is chosen independently for each site i and for each CDW component $\alpha = 3, 4, 5$ and 6. Specifically we choose each value $h_{i\alpha}$ from a Gaussian distribution with mean 0 and standard deviation σ such that

$$\begin{aligned} \overline{h_{i\alpha}} &= 0, \\ \overline{h_{i\alpha} h_{j\beta}} &= \sigma^2 \delta_{ij} \delta_{\alpha\beta}. \end{aligned} \tag{4.52}$$

Recall that the non-local Monte Carlo cluster updates of Algorithms 3.2 and 4.1 can only be applied to the two-dimensional effective Hamiltonian of Equation (4.8) when all coupling within the six-dimensional order parameter space were isotropic such that $\lambda = 1$. Similarly, for the Hamiltonian of Equation (4.51) we must fix $\lambda = 1$ and $V_z = V_z'$ in order to use similar cluster algorithms. In the presence of the interlayer coupling V_z and no disorder ($\sigma = 0$), one can still use Algorithms 3.2 and 4.1, but with the small adjustment that the probability of adding a nearest-neighbour spin j to the cluster must be changed to $1 - \exp\{\min[0, -2\beta V_z (\mathbf{r} \cdot \mathbf{n}_i)(\mathbf{r} \cdot \mathbf{n}_j)]\}$ for the cases where this site j is a neighbour along the z-direction. In order to use these algorithms in the presence of disorder, one must adjust the cluster acceptance probability to account for the on-site energy due to the disorder. In the case of Algorithm 4.1, this disorder term means that the generated clusters are no longer accepted with probability one.

In the calculations that following, we vary the parameters V_z, g, g', w and $h_{i\alpha}$, and we fix $\lambda = 1$ and $V_z = V_z'$. We consider Monte Carlo calculations on lattices with $L_x = L_y \equiv L_{xy}$ sites along each of the x and y directions and L_z sites along the z direction. In situations where we take the interlayer coupling V_z to be weaker than the in-plane coupling ρ_s, we find that we can achieve well-converged data by taking L_z smaller than L_{xy}. For example, in many of the calculations that follow, we perform simulations on lattices with $L_{xy} = 32$ and $L_z = 8$.

4.6.1 Interlayer coupling

We consider first the effects of the interlayer coupling V_z on the model of Equation (4.51). To this end, we set $\sigma = 0$ for now such that there is no disorder present in the model and we can isolate more clearly the effects of the parameter V_z. In Figure 4.17, we plot the CDW structure factor S_{Φ_x} as a function of temperature for various values of the interlayer coupling. We plot results from both Monte Carlo simulations as well as from large-N

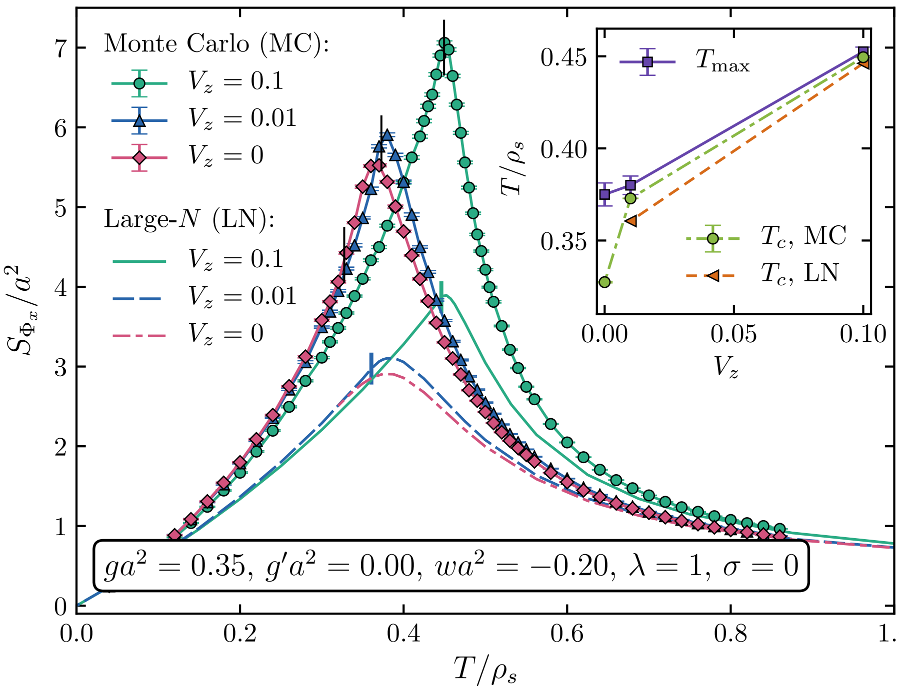

Figure 4.17: The effects of the interlayer coupling V_z on the CDW structure factors S_{Φ_x} and on the SC critical temperature T_c. In the main plot, we show Monte Carlo (MC) results for S_{Φ_x} as a function of T for various values of V_z. We compare with analytical large-N (LN) calculations. The short vertical lines mark T_c. In the inset, we demonstrate that T_c approaches the location T_{peak} of the peak in the CDW structure factor as the interlayer coupling is increased. The MC and LN calculations give the same estimates for T_{peak} within error.

expansions (see Section 4.3.1). The Monte Carlo calculations for $V_z = 0, 0.01$ and 0.1 are performed on lattices with sizes $L_x \times L_y \times L_z = 64 \times 64 \times 1$, $32 \times 32 \times 8$ and $24 \times 24 \times 14$ (respectively). We find that, as V_z increases (or, in other words, as the system becomes more 3D-like), the maximum value of S_{Φ_x} increases.

In addition, we consider the effects of the interlayer coupling strength on the SC transition temperature T_c. Within Figure 4.17, we use short vertical lines to indicate the locations of T_c for each curve. In the Monte Carlo simulations, we measure T_c by using the method described in Section 4.4.2. Within the large-N expansions, we note that there is no phase transition in the case where $V_z = 0$ (or, in other words, when the system is two-dimensional). In the inset, we compare these values of T_c with the location T_{peak} of the peak in the CDW structure factor. We find that T_c approaches T_{peak} from below as the interlayer coupling becomes stronger.

4.6.2 Random-field disorder

In the presence of random-field disorder ($\sigma \neq 0$), Monte Carlo calculations of the CDW structure factor S_{Φ_x} require averaging over many independent realizations of disorder (ROD), $\{h_{i\alpha}\}$. Even though each random field $h_{i\alpha}$ is generated from a symmetric distribution (about a mean value of 0), the corresponding distribution of S_{Φ_x} is in general asymmetric since S_{Φ_x} is a complicated, nonlinear function of $h_{\alpha i}$. In fact, our numerical studies reveal that, as σ is increased, the distribution of S_{Φ_x} over various ROD becomes increasingly asymmetric due to the fact that S_{Φ_x} is a complicated, nonlinear function of the disorder fields $h_{\alpha i}$. As a result, the average value, $[\langle S_{\Phi_x}\rangle]_{\text{ROD}}$, of this distribution becomes different from its typical value, $\exp\left[\ln\langle S_{\Phi_x}\rangle\right]_{\text{ROD}}$, where $\langle\ldots\rangle$ and $[\ldots]_{\text{ROD}}$ denote thermal and disorder averages, respectively [110]. However, in order to allow comparison with large-N results (for which calculations of the typical value are extremely difficult), all of the following Monte Carlo results correspond to average values of the disorder distributions. The qualitative behaviour of the structure factors is similar if one instead examines the typical values.

The Monte Carlo simulations are performed on lattices of size $L_x \times L_y \times L_z = 32 \times 32 \times 8$. In cases where no disorder is present ($\sigma = 0$), the error bars in our Monte Carlo results correspond to thermal averaging. In the presence of disorder, error bars instead correspond to the standard deviation of the mean over independent ROD. Our results average over between 10^2 and 10^3 ROD. We find that both when we increase σ and when we study temperatures near the structure factor peak, more ROD are required in order to obtain converged numerical results.

In Figure 4.18, we plot the CDW structure factors S_{Φ_x} as a function of temperature for various disorder strengths σ. We find that adding disorder leads to a finite value of S_{Φ_x} in the limit $T \to 0$, in contrast to the structure factors corresponding to no disorder in Figures 4.9, 4.16 and 4.17. Depending on the choices of the other model parameters, sometimes we find that S_{Φ_x} decreases monotonically as T is lowered from T_{peak} to $T = 0$, while in other cases we observe a local minimum in S_{Φ_x} at a finite value of T below T_{peak} such that the CDW structure factor increases as $T \to 0$.

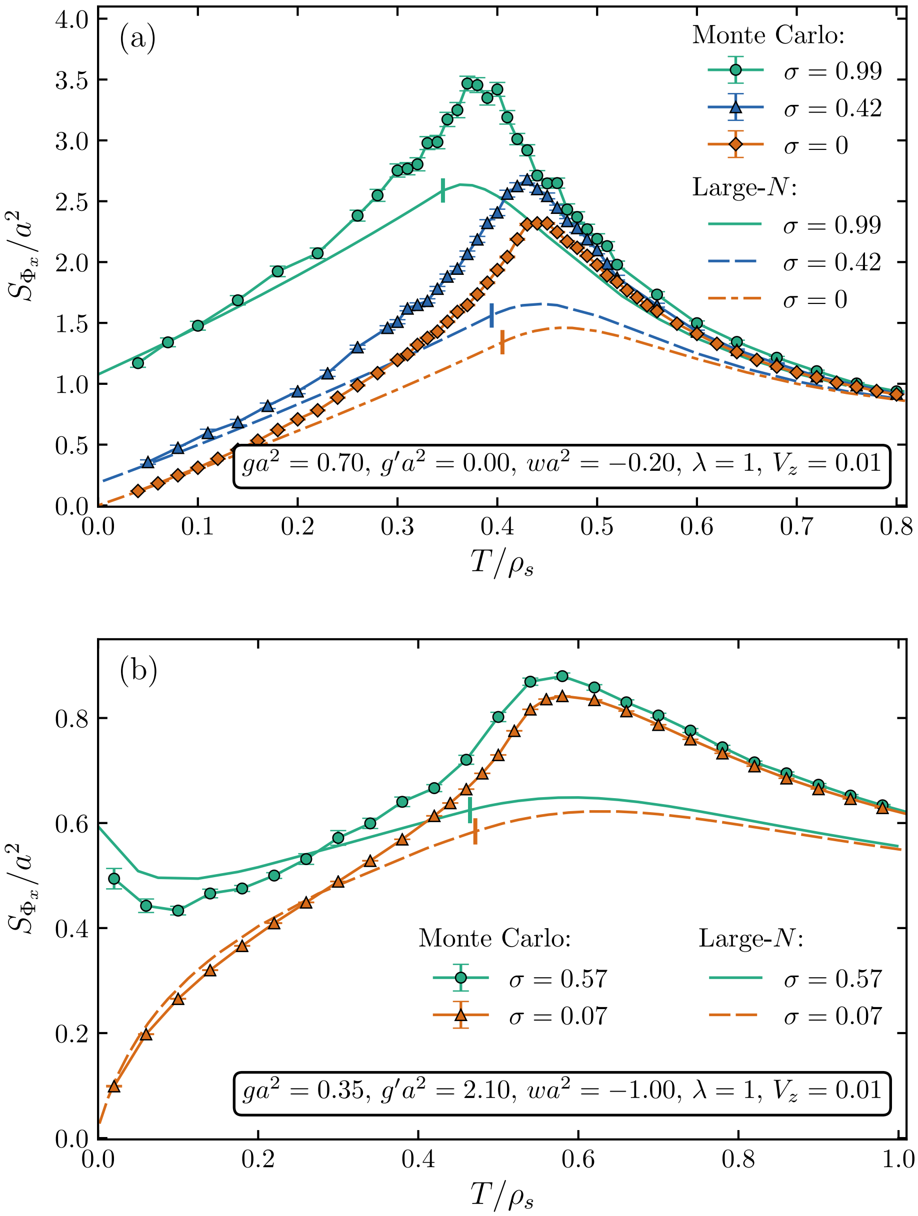

Figure 4.18: The CDW structure factor S_{Φ_x} as a function of temperature T for various choices of the disorder strength σ. (a) and (b) show S_{Φ_x} for different choices of the model parameters ga^2, $g'a^2$ and wa^2, but both sets of parameters correspond to SC order in the ground state [71].

4.6.3 Comparisons with x-ray scattering experiments

Unlike the Monte Carlo and large-N results presented in earlier sections, here we do not explicitly performs fits of our data to experimental measurements. The reason for omitting such comparisons in Figures 4.17 and 4.18 is that the parameter space corresponding to Equation (4.51) is quite large, and each Monte Carlo simulation becomes increasingly computationally expensive as either the interlayer coupling V_z or the disorder strength σ increases. However, one can still draw important conclusions about how well the model of Equation (4.51) agrees with data from x-ray scattering experiments.

In Section 4.6.1, we saw that the superconducting critical temperature T_c approaches T_{peak} from below as the interlayer coupling V_z becomes stronger. This approach corresponds to a better agreement with x-ray experiments [75, 76, 77, 97, 98], where $T_c \approx T_{\text{peak}}$ (as discussed in Section 4.4.2).

The calculations in Section 4.6.2 reveal that adding disorder leads to a finite value of S_{Φ_x} in the limit of low temperatures (with the rest of curve remaining qualitatively similar to the zero-disorder case). As a result, we conclude that the incorporation of the random disorder field $h_{i\alpha}$ in Equation (4.51) extends agreement with x-ray scattering intensities to a wider range of temperatures such that, in particular, this model can potentially describe such experimental data in the limit of low temperatures.

Chapter 5

Conclusions and future directions

Throughout this thesis, we have seen that computational studies of lattice field theories can reveal new exotic features of both non-interacting and interacting quantum systems. Theories related to the classical $O(N)$ model are capable of describing various types of classical and quantum phase transitions and critical behaviour. We have specifically seen that various lattice models are capable of yielding universal numbers that characterize criticality, and that certain effective models can reproduce experimental features of the pseudogap regime within high-temperature cuprate superconductors.

From entanglement entropy scaling arguments, we have seen that in the vicinity of a critical point, one can extract an abundant collection of universal quantities from various entangling geometries. In particular, we have extracted such quantities from both sharp vertices and smooth two-cylinder geometries for non-interacting bosonic field theories. Especially in higher spatial dimensions, universal corrections are often subleading to several higher-order entanglement scaling terms, and one must use numerical schemes such as the numerical linked cluster expansion in order to isolate these subleading universal features. In addition to revealing new fundamental characterizations of Gaussian fixed points, our resulting universal coefficients lay the groundwork for future studies of corresponding coefficients in interacting systems [111]. Comparisons between specific universal quantities at different fixed points have the potential to reveal new information about the underlying theories governing a system's renormalization group flows, akin to the c-theorem in one spatial dimension [112], the F-theorem in two spatial dimensions [113, 114, 115, 116, 117] and the a-theorem in three spatial dimensions [118, 119, 120]. Extracting universal numbers from both new entangling geometries and from other lattice models will lead to a more complete understanding of the connections and relationships between different quantum systems.

For strongly-interacting models, we have seen that numerical simulations offer analytically-unattainable insight into the system's emergent phases and critical behaviour. We have focussed on applications of such simulations to effective models of high-temperature superconductivity. By using symmetry constraints related to superconducting and charge-density wave order, we have introduced an effective classical field theory for modelling the behaviour of cuprate materials within the vicinity of their pseudogap regime. We have utilized traditional Monte Carlo methods along with new symmetry-based cluster updates in order to simulate the charge-density wave structure factor, correlation length, superconducting critical temperature and diamagnetic susceptibility associated with this effective lattice model. After establishing agreement with recent x-ray scattering experiments for a wide range of temperatures, we incorporated into our model effects of interlayer coupling and random-field disorder and performed new disorder-averaged simulations in order to further extend agreement with such experiments. Certain aspects of our effective model are yet to be explored, such as the effect of disorder strength on CDW correlation length. The underlying mechanism governing high-temperature superconductivity remains unknown, and a promising avenue for future research is to explore new effective models that incorporate the effects of other experimentally-observed features such as spin-density wave order [121]. $O(N)$-like models with higher-dimensional degrees of freedom are capable of incorporating more of these physical features and may lead to a more robust model of high-temperature superconductivity. Such future models will be based and built upon the simulation outcomes of our current effective model, which indicate that the competition between superconducting and charge-density wave order near the superconducting phase transition plays a fundamental role in describing the pseudogap physics of cuprate materials.

Strongly-interacting quantum systems are fundamentally characterized by their deep-rooted complexity, with analytical methods incapable of fully linking atomic-scale variables to thermodynamic observables. Computational methods are therefore indispensable for advancing studies of emergent phases and critical behaviour in quantum matter due to their unique ability to act as a bridge between microscopic lattice theories and macroscopic phenomena.

References

[1] P. Di Francesco, P. Mathieu and D. Sénéchal, *Conformal Field Theory*, Springer (1997).

[2] M. Kardar, *Statistical Physics of Fields*, Cambridge University Press (2007).

[3] S. Sachdev, *Quantum Phase Transitions*, Cambridge University Press, 2nd edition (2011).

[4] N. Goldenfeld, *Lectures on Phase Transitions and the Renormalization Group*, Westview Press (1992).

[5] J. Cardy, *Scaling and Renormalization in Statistical Physics*, Cambridge University Press (1996).

[6] M. E. J. Newman and G. T. Barkema, *Monte Carlo Methods in Statistical Physics*, Clarendon Press (1999).

[7] R. D. Sorkin, "On the Entropy of the vacuum outside a horizon", in B. Bertotti, F. de Felice and A. Pascolini (editors), "Tenth International Conference on General Relativity and Gravitation", Consiglio Nazionale Delle Ricerche, Roma (held in Padova, 4-9 July, 1983), (734–736), `arXiv:1402.3589`.

[8] L. Bombelli, R. K. Koul, J. Lee and R. D. Sorkin, "Quantum source of entropy for black holes", *Phys. Rev. D* **34**, 373–383 (1986).

[9] M. Srednicki, "Entropy and area", *Phys. Rev. Lett.* **71**, 666–669 (1993), `arXiv: hep-th/9303048`.

[10] A. Rényi, "On measures of information and entropy", in "Proceedings of the 4th Berkeley Symposium on Mathematics, Statistics and Probability", University of California Press (1961), volume 1, (547–561).

[11] A. Rényi, “On the foundations of information theory”, *Rev. Int. Stat. Inst.* **33** (1), 1–14 (1965).

[12] B. Swingle, “Mutual information and the structure of entanglement in quantum field theory”, (2010), `arXiv:1010.4038`.

[13] M. A. Metlitski, private communication (2016).

[14] C. Holzhey, F. Larsen and F. Wilczek, “Geometric and renormalized entropy in conformal field theory”, *Nucl. Phys. B* **424**, 443–467 (1994), `arXiv:hep-th/9403108`.

[15] G. Vidal, J. I. Latorre, E. Rico and A. Kitaev, “Entanglement in quantum critical phenomena”, *Phys. Rev. Lett.* **90**, 227902 (2003), `arXiv:quant-ph/0211074`.

[16] J. I. Latorre, E. Rico and G. Vidal, “Ground state entanglement in quantum spin chains”, *Quant. Inf. Comput.* **4**, 48–92 (2004), `arXiv:quant-ph/0304098`.

[17] V. E. Korepin, “Universality of entropy scaling in one dimensional gapless models”, *Phys. Rev. Lett.* **92**, 096402 (2004), `arXiv:cond-mat/0311056`.

[18] P. Calabrese and J. L. Cardy, “Entanglement entropy and quantum field theory”, *J. Stat. Mech.* **0406**, P06002 (2004), `arXiv:hep-th/0405152`.

[19] P. Calabrese and J. Cardy, “Entanglement entropy and conformal field theory”, *J. Phys. A* **42**, 504005 (2009), `arXiv:0905.4013`.

[20] S. N. Solodukhin, “Entanglement entropy, conformal invariance and extrinsic geometry”, *Phys. Lett. B* **665**, 305–309 (2008), `arXiv:0802.3117`.

[21] D. V. Fursaev, “Entanglement Rényi entropies in conformal field theories and holography”, *JHEP* **05**, 080 (2012), `arXiv:1201.1702`.

[22] J. Lee, L. McGough and B. R. Safdi, “Rényi entropy and geometry”, *Phys. Rev. D* **89** (12), 125016 (2014), `arXiv:1403.1580`.

[23] R. Lohmayer, H. Neuberger, A. Schwimmer and S. Theisen, “Numerical determination of entanglement entropy for a sphere”, *Phys. Lett. B* **685**, 222–227 (2010), `arXiv:0911.4283`.

[24] H. Casini and M. Huerta, “Entanglement entropy for the n-sphere”, *Phys. Lett. B* **694**, 167–171 (2011), `arXiv:1007.1813`.

[25] H. Liu and M. Mezei, “A Refinement of entanglement entropy and the number of degrees of freedom”, *JHEP* **04**, 162 (2013), `arXiv:1202.2070`.

[26] S. N. Solodukhin, “Entanglement entropy of round spheres”, *Phys. Lett. B* **693**, 605–608 (2010), `arXiv:1008.4314`.

[27] W. Witczak-Krempa, L. E. Hayward Sierens and R. G. Melko, “Cornering gapless quantum states via their torus entanglement”, *Phys. Rev. Lett.* **118**, 077202 (2017), `arXiv:1603.02684`.

[28] J. Helmes, L. E. Hayward Sierens, A. Chandran, W. Witczak-Krempa and R. G. Melko, “Universal corner entanglement of Dirac fermions and gapless bosons from the continuum to the lattice”, *Phys. Rev. B* **94**, 125142 (2016), `arXiv:1606.03096`.

[29] L. Chojnacki, C. Q. Cook, D. Dalidovich, L. E. Hayward Sierens, E. Lantagne-Hurtubise, R. G. Melko and T. J. Vlaar, “Shape dependence of two-cylinder Renyi entropies for free bosons on a lattice”, *Phys. Rev. B* **94**, 165136 (2016), `arXiv:1607.05311`.

[30] L. E. Hayward Sierens, P. Bueno, R. R. P. Singh, R. C. Myers and R. G. Melko, “Cubic trihedral corner entanglement for a free scalar”, (2017), `arXiv:1703.03413`.

[31] S. Sahoo, E. M. Stoudenmire, J.-M. Stéphan, T. Devakul, R. R. P. Singh and R. G. Melko, “Unusual Corrections to Scaling and Convergence of Universal Renyi Properties at Quantum Critical Points”, *Phys. Rev. B* **93**, 085120 (2016), `arXiv:1509.00468`.

[32] H. Casini and M. Huerta, “Entanglement entropy in free quantum field theory”, *J. Phys. A* **42**, 504007 (2009), `arXiv:0905.2562`.

[33] A. Chandran, private communication (2016).

[34] I. Peschel, “Calculation of reduced density matrices from correlation functions”, *J. Phys. A: Math. Gen.* **36**, L205 (2003).

[35] X. Chen, G. Y. Cho, T. Faulkner and E. Fradkin, “Scaling of entanglement in $2+1$-dimensional scale-invariant field theories”, *J. Stat. Mech.* **1502**, P02010 (2015), `arXiv:1412.3546`.

[36] X. Chen, private communication (2016).

[37] X. Chen, W. Witczak-Krempa, T. Faulkner and E. Fradkin, “Two-cylinder entanglement entropy under a twist”, *J. Stat. Mech.* **1704**, 043104 (2017), `arXiv:1611.01847`.

[38] M. Rigol, T. Bryant and R. R. P. Singh, “Numerical linked-cluster approach to quantum lattice models”, *Phys. Rev. Lett.* **97**, 187202 (2006), `arXiv:cond-mat/0611102`.

[39] M. Rigol, T. Bryant and R. R. P. Singh, “Numerical linked-cluster algorithms. I. Spin systems on square, triangular, and kagomé lattices”, *Phys. Rev. E* **75**, 061118 (2007), `arXiv:0706.3254`.

[40] M. Rigol, T. Bryant and R. R. P. Singh, “Numerical linked-cluster algorithms. II. t-J models on the square lattice”, *Phys. Rev. E* **75**, 061119 (2007), `arXiv:0706.3255`.

[41] B. Tang, E. Khatami and M. Rigol, “A short introduction to numerical linked-cluster expansions”, *Computer Physics Communications* **184** (3), 557 – 564 (2013), `arXiv:1207.3366`.

[42] A. B. Kallin, K. Hyatt, R. R. P. Singh and R. G. Melko, “Entanglement at a two-dimensional quantum critical point: A numerical linked-cluster expansion study”, *Phys. Rev. Lett.* **110**, 135702 (2013), `arXiv:1212.5269`.

[43] A. B. Kallin, E. M. Stoudenmire, P. Fendley, R. R. P. Singh and R. G. Melko, “Corner contribution to the entanglement entropy of an $O(3)$ quantum critical point in 2+1 dimensions”, *J. Stat. Mech.* **1406**, P06009 (2014), `arXiv:1401.3504`.

[44] E. M. Stoudenmire, P. Gustainis, R. Johal, S. Wessel and R. G. Melko, “Corner contribution to the entanglement entropy of strongly interacting $O(2)$ quantum critical systems in 2+1 dimensions”, *Phys. Rev. B* **90**, 235106 (2014), `arXiv:1409.6327`.

[45] J. Cardy and P. Calabrese, “Unusual corrections to scaling in entanglement entropy”, *J. Stat. Mech.* **1004**, P04023 (2010), `arXiv:1002.4353`.

[46] L. Bianchi, M. Meineri, R. C. Myers and M. Smolkin, “Rényi entropy and conformal defects”, *JHEP* **07**, 076 (2016), `arXiv:1511.06713`.

[47] T. Devakul and R. R. P. Singh, “Entanglement across a cubic interface in $3+1$ dimensions”, *Phys. Rev. B* **90**, 054415 (2014), `arXiv:1407.0084`.

[48] N. Shiba, “The Aharonov-Bohm effect on entanglement entropy in conformal field theory”, (2017), `arXiv:1701.00688`.

[49] H. Ju, A. B. Kallin, P. Fendley, M. B. Hastings and R. G. Melko, “Entanglement scaling in two-dimensional gapless systems”, *Phys. Rev. B* **85**, 165121 (2012), `arXiv:1112.4474`.

[50] J.-M. Stéphan, H. Ju, P. Fendley and R. G. Melko, “Entanglement in gapless resonating-valence-bond states”, *New Journal of Physics* **15** (1), 015004 (2013), `arXiv:1207.3820`.

[51] H. Casini, C. D. Fosco and M. Huerta, “Entanglement and alpha entropies for a massive Dirac field in two dimensions”, *J. Stat. Mech.* **0507**, P07007 (2005), `arXiv:cond-mat/0505563`.

[52] H. Casini and M. Huerta, “Remarks on the entanglement entropy for disconnected regions”, *JHEP* **03**, 048 (2009), `arXiv:0812.1773`.

[53] P. Bueno, R. C. Myers and W. Witczak-Krempa, “Universality of corner entanglement in conformal field theories”, *Phys. Rev. Lett.* **115**, 021602 (2015), `arXiv:1505.04804`.

[54] P. Bueno, R. C. Myers and W. Witczak-Krempa, “Universal corner entanglement from twist operators”, *JHEP* **09**, 091 (2015), `arXiv:1507.06997`.

[55] A. Milsted, private communication (2017).

[56] N. Metropolis, A. W. Rosenbluth, M. N. Rosenbluth, A. H. Teller and E. Teller, “Equation of state calculations by fast computing machines”, *J. Chem. Phys.* **21**, 1087–1092 (1953).

[57] W. K. Hastings, “Monte Carlo sampling methods using Markov chains and their applications”, *Biometrika* **57**, 97–109 (1970).

[58] R. H. Swendsen and J.-S. Wang, “Nonuniversal critical dynamics in Monte Carlo simulations”, *Phys. Rev. Lett.* **58**, 86–88 (1987).

[59] U. Wolff, “Collective Monte Carlo updating for spin systems”, *Phys. Rev. Lett.* **62**, 361 (1989).

[60] L. E. Hayward, D. G. Hawthorn, R. G. Melko and S. Sachdev, “Angular fluctuations of a multi-component order describe the pseudogap regime of the cuprate superconductors”, *Science* **343**, 1336 (2014), `arXiv:1309.6639`.

[61] J. M. Cook, "Rational formulae for the production of a spherically symmetric probability distribution", *Math. Comp.* **11**, 81–82 (1957).

[62] J. S. Hicks and R. F. Wheeling, "An efficient method for generating uniformly distributed points on the surface of an n-dimensional sphere", *Commun. ACM* **2** (4), 17–19 (1959).

[63] M. E. Muller, "A note on a method for generating points uniformly on N-dimensional spheres", *Commun. ACM* **2** (4), 19–20 (1959).

[64] M. Sibuya, "A method for generating uniformly distributed points on N-dimensional spheres", *Ann. Inst. Statist. Math.* **14** (1), 81–85 (1962).

[65] G. Marsaglia, "Choosing a point from the surface of a sphere", *Ann. Math. Statist.* **43** (2), 645–646 (1972).

[66] Y. Tashiro, "On methods for generating uniform random points on the surface of a sphere", *Ann. Inst. Statist. Math.* **29** (1), 295–300 (1977).

[67] G. E. P. Box and M. E. Muller, "A note on the generation of random normal deviates", *Ann. Math. Statist.* **29** (2), 610–611 (1958).

[68] H. G. Ballesteros, L. A. Fernández, V. Martín-Mayor and A. Muñoz Sudupe, "Finite size effects on measures of critical exponents in $d = 3$ $O(N)$ models", *Phys. Lett. B* **387**, 125–131 (1996), `arXiv:cond-mat/9606203`.

[69] K. Kanaya and S. Kaya, "Critical exponents of a three-dimensional O(4) spin model", *Phys. Rev. D* **51**, 2404–2410 (1995), `arXiv:hep-lat/9409001`.

[70] L. E. Hayward, A. J. Achkar, D. G. Hawthorn, R. G. Melko and S. Sachdev, "Diamagnetism and density-wave order in the pseudogap regime of $YBa_2Cu_3O_{6+x}$", *Phys. Rev. B* **90**, 094515 (2014), `arXiv:1406.2694`.

[71] L. Nie, L. E. Hayward Sierens, R. G. Melko, S. Sachdev and S. A. Kivelson, "Fluctuating orders and quenched randomness in the cuprates", *Phys. Rev. B* **92**, 174505 (2015), `arXiv:1505.06206`.

[72] J. Bardeen, L. N. Cooper and J. R. Schrieffer, "Microscopic theory of superconductivity", *Phys. Rev.* **106**, 162–164 (1957).

[73] J. Bardeen, L. N. Cooper and J. R. Schrieffer, "Theory of superconductivity", *Phys. Rev.* **108**, 1175–1204 (1957), URL `http://link.aps.org/doi/10.1103/PhysRev.108.1175`.

[74] J. G. Bednorz and K. A. Müller, "Possible high T_c superconductivity in the Ba-La-Cu-O system", *Z. Phys.* **B64**, 189–193 (1986).

[75] J. Chang, E. Blackburn, A. T. Holmes, N. B. Christensen, J. Larsen, J. Mesot, R. Liang, D. A. Bonn, W. N. Hardy, A. Watenphul, M. v. Zimmermann, E. M. Forgan and S. M. Hayden, "Direct observation of competition between superconductivity and charge density wave order in $YBa_2Cu_3O_{6.67}$", *Nature Physics* **8**, 871–876, `arXiv:1206.4333`.

[76] G. Ghiringhelli, M. Le Tacon, M. Minola, S. Blanco-Canosa, C. Mazzoli, N. B. Brookes, G. M. De Luca, A. Frano, D. G. Hawthorn, F. He, T. Loew, M. M. Sala, D. C. Peets, M. Salluzzo, E. Schierle, R. Sutarto, G. A. Sawatzky, E. Weschke, B. Keimer and L. Braicovich, "Long-range incommensurate charge fluctuations in $(Y,Nd)Ba_2Cu_3O_{6+x}$", *Science* **337** (6096), 821–825 (2012), `arXiv:1207.0915`.

[77] A. J. Achkar, R. Sutarto, X. Mao, F. He, A. Frano, S. Blanco-Canosa, M. Le Tacon, G. Ghiringhelli, L. Braicovich, M. Minola, M. Moretti Sala, C. Mazzoli, R. Liang, D. A. Bonn, W. N. Hardy, B. Keimer, G. A. Sawatzky and D. G. Hawthorn, "Distinct charge orders in the planes and chains of ortho-III-ordered $YBa_2Cu_3\mathbf{O}_{6+\delta}$ superconductors identified by resonant elastic x-ray scattering", *Phys. Rev. Lett.* **109**, 167001 (2012), `arXiv:1207.3667`.

[78] A. Polyakov, "Interaction of goldstone particles in two dimensions. applications to ferromagnets and massive Yang-Mills fields", *Physics Letters B* **59** (1), 79 – 81 (1975), ISSN 0370-2693.

[79] S. Chakravarty, B. I. Halperin and D. R. Nelson, "Low-temperature behavior of two-dimensional quantum antiferromagnets", *Phys. Rev. Lett.* **60**, 1057–1060 (1988).

[80] B. Keimer, N. Belk, R. J. Birgeneau, A. Cassanho, C. Y. Chen, M. Greven, M. A. Kastner, A. Aharony, Y. Endoh, R. W. Erwin and G. Shirane, "Magnetic excitations in pure, lightly doped, and weakly metallic la_2cuo_4", *Phys. Rev. B* **46**, 14034–14053 (1992).

[81] A. J. Achkar, X. Mao, C. McMahon, R. Sutarto, F. He, R. Liang, D. A. Bonn, W. N. Hardy and D. G. Hawthorn, "Impact of quenched oxygen disorder on charge

density wave order in $\mathrm{YBa_2Cu_3O_{6+x}}$", *Phys. Rev. Lett.* **113**, 107002 (2014), `arXiv:1312.6630`.

[82] V. L. Berezinskii, "Destruction of long-range order in one-dimensional and two-dimensional systems having a continuous symmetry group I. Classical systems", *Soviet Journal of Experimental and Theoretical Physics* **32** (3), 493 (1971).

[83] V. L. Berezinskii, "Destruction of long-range order in one-dimensional and two-dimensional systems possessing a continuous symmetry group. II. Quantum systems", *Soviet Journal of Experimental and Theoretical Physics* **34** (3), 610 (1972).

[84] J. M. Kosterlitz and D. J. Thouless, "Long range order and metastability in two dimensional solids and superfluids. (Application of dislocation theory)", *Journal of Physics C: Solid State Physics* **5**, L124 (1972).

[85] J. M. Kosterlitz and D. J. Thouless, "Ordering, metastability and phase transitions in two-dimensional systems", *Journal of Physics C: Solid State Physics* **6**, 1181–1203 (1973).

[86] J. M. Kosterlitz, "The critical properties of the two-dimensional xy model", *Journal of Physics C: Solid State Physics* **7**, 1046–1060 (1974).

[87] D. R. Nelson and J. M. Kosterlitz, "Universal jump in the superfluid density of two-dimensional superfluids", *Phys. Rev. Lett.* **39**, 1201–1205 (1977).

[88] S. Teitel and C. Jayaprakash, "Phase transtions in frustrated two-dimensional XY models", *Phys. Rev. B* **27**, 598–601 (1983).

[89] M. Hasenbusch, "The Binder cumulant at the Kosterlitz-Thouless transition", *Journal of Statistical Mechanics: Theory and Experiment* **0808**, P08003 (2008), `arXiv:0804.1880`.

[90] A. W. Sandvik, "Computational studies of quantum spin systems", *AIP Conf. Proc.* **1297**, 135 (2010), `arXiv:1101.3281`.

[91] N. V. Prokof'ev and B. V. Svistunov, "Two definitions of superfluid density", *Phys. Rev. B* **61**, 11282–11284 (2000), `arXiv:cond-mat/9907203`.

[92] R. G. Melko, A. W. Sandvik and D. J. Scalapino, "Aspect-ratio dependence of the spin stiffness of a two-dimensional XY model", *Phys. Rev. B* **69**, 014509 (2004), `arXiv:cond-mat/0302591`.

[93] H. Weber and P. Minnhagen, "Monte Carlo determination of the critical temperature for the two-dimensional XY model", *Phys. Rev. B* **37**, 5986–5989 (1988).

[94] M. Hasenbusch, "The two-dimensional XY model at the transition temperature: a high-precision Monte Carlo study", *Journal of Physics A: Mathematical and General* **38** (26), 5869 (2005), `arXiv:cond-mat/0502556`.

[95] Y.-D. Hsieh, Y.-J. Kao and A. W. Sandvik, "Finite-size scaling method for the Berezinskii-Kosterlitz-Thouless transition", *Journal of Statistical Mechanics: Theory and Experiment* **1309**, P09001 (2013), `arXiv:1302.2900`.

[96] S. Sachdev and E. Demler, "Competing orders in thermally fluctuating superconductors in two dimensions", *Phys. Rev. B* **69**, 144504 (2004), `arXiv:cond-mat/0308024`.

[97] E. Blackburn, J. Chang, M. Hücker, A. T. Holmes, N. B. Christensen, R. Liang, D. A. Bonn, W. N. Hardy, U. Rütt, O. Gutowski, M. v. Zimmermann, E. M. Forgan and S. M. Hayden, "X-ray diffraction observations of a charge-density-wave order in superconducting ortho-II $YBa_2Cu_3\mathbf{O}_{6.54}$ single crystals in zero magnetic field", *Phys. Rev. Lett.* **110**, 137004 (2013), `arXiv:1212.3836`.

[98] M. Hücker, N. B. Christensen, A. T. Holmes, E. Blackburn, E. M. Forgan, R. Liang, D. A. Bonn, W. N. Hardy, O. Gutowski, M. v. Zimmermann, S. M. Hayden and J. Chang, "Competing charge, spin, and superconducting orders in underdoped $YBa_2Cu_3O_y$", *Phys. Rev. B* **90**, 054514 (2014), `arXiv:1405.7001`.

[99] Y. Wang, L. Li, M. J. Naughton, G. D. Gu, S. Uchida and N. P. Ong, "Field-enhanced diamagnetism in the pseudogap state of the cuprate $Bi_2Sr_2CaCu_2O_{8+\delta}$ superconductor in an intense magnetic field", *Phys. Rev. Lett.* **95**, 247002 (2005), `arXiv:cond-mat/0503190`.

[100] L. Li, J. G. Checkelsky, S. Komiya, Y. Ando and N. P. Ong, "Low-temperature vortex liquid in $La_{2-x}Sr_xCuO_4$", *Nature Physics* **3**, 311–314 (2007), `arXiv:cond-mat/0702121`.

[101] L. Li, Y. Wang, S. Komiya, S. Ono, Y. Ando, G. D. Gu and N. P. Ong, "Diamagnetism and cooper pairing above T_c in cuprates", *Phys. Rev. B* **81**, 054510 (2010), `arXiv:0906.1823`.

[102] I. Kokanović, D. J. Hills, M. L. Sutherland, R. Liang and J. R. Cooper, "Diamagnetism of $YBa_2Cu_3O_{6+x}$ crystals above T_c: Evidence for Gaussian fluctuations", *Phys. Rev. B* **88**, 060505 (2013), `arXiv:1303.6860`.

[103] R. Comin, A. Frano, M. M. Yee, Y. Yoshida, H. Eisaki, E. Schierle, E. Weschke, R. Sutarto, F. He, A. Soumyanarayanan, Y. He, M. Le Tacon, I. S. Elfimov, J. E. Hoffman, G. A. Sawatzky, B. Keimer and A. Damascelli, "Charge order driven by Fermi-arc instability in $\mathrm{Bi_2Sr_{2-x}La_xCuO_{6+\delta}}$", *Science* **343** (6169), 390–392 (2014), `arXiv:1312.1343`.

[104] E. H. da Silva Neto, P. Aynajian, A. Frano, R. Comin, E. Schierle, E. Weschke, A. Gyenis, J. Wen, J. Schneeloch, Z. Xu, S. Ono, G. Gu, M. Le Tacon and A. Yazdani, "Ubiquitous interplay between charge ordering and high-temperature superconductivity in cuprates", *Science* **343** (6169), 393–396 (2014), `arXiv:1312.1347`.

[105] R. Comin, R. Sutarto, F. He, E. H. da Silva Neto, L. Chauviere, A. Frano, R. Liang, W. N. Hardy, D. A. Bonn, Y. Yoshida, H. Eisaki, A. J. Achkar, D. G. Hawthorn, B. Keimer, G. A. Sawatzky and A. Damascelli, "Symmetry of charge order in cuprates", *Nature Materials* **14**, 796–800 (2015), `arXiv:1402.5415`.

[106] C. Ebner and D. Stroud, "Diamagnetic susceptibility of superconducting clusters: Spin-glass behavior", *Phys. Rev. B* **31**, 165–171 (1985).

[107] D. Podolsky, S. Raghu and A. Vishwanath, "Nernst effect and diamagnetism in phase fluctuating superconductors", *Phys. Rev. Lett.* **99**, 117004 (2007), `arXiv:cond-mat/0612096`.

[108] K. Sarkar, S. Banerjee, S. Mukerjee and T. Ramakrishnan, "Doping dependence of fluctuation diamagnetism in high T_c superconductors", *Annals of Physics* **365**, 7–23 (2016), `arXiv:1309.3776`.

[109] J. R. Cooper, private communication (2013).

[110] A. Del Maestro, private communication (2015).

[111] B. Kulchytskyy and R. G. Melko, work in progress.

[112] A. B. Zamolodchikov, "Irreversibility of the flux of the renormalization group in a 2D field theory", *JETP Lett.* **43**, 730–732 (1986), [Pisma Zh. Eksp. Teor. Fiz.43,565 (1986)].

[113] R. C. Myers and A. Sinha, "Seeing a c-theorem with holography", *Phys. Rev. D* **82**, 046006 (2010), `arXiv:1006.1263`.

[114] R. C. Myers and A. Sinha, "Holographic c-theorems in arbitrary dimensions", *JHEP* **01**, 125 (2011), `arXiv:1011.5819`.

[115] D. L. Jafferis, I. R. Klebanov, S. S. Pufu and B. R. Safdi, “Towards the F-theorem: N=2 field theories on the three-sphere”, *JHEP* **06**, 102 (2011), `arXiv:1103.1181`.

[116] I. R. Klebanov, S. S. Pufu and B. R. Safdi, “F-theorem without supersymmetry”, *JHEP* **10**, 038 (2011), `arXiv:1105.4598`.

[117] H. Casini and M. Huerta, “On the RG running of the entanglement entropy of a circle”, *Phys. Rev. D* **85**, 125016 (2012), `1202.5650`.

[118] J. L. Cardy, “Is there a c theorem in four dimensions?”, *Phys. Lett.* **B215**, 749–752 (1988).

[119] Z. Komargodski and A. Schwimmer, “On renormalization group flows in four dimensions”, *JHEP* **12**, 099 (2011), `arXiv:1107.3987`.

[120] Z. Komargodski, “The constraints of conformal symmetry on RG flows”, *JHEP* **07**, 069 (2012), `arXiv:1112.4538`.

[121] L. Nie, A. V. Maharaj, E. Fradkin and S. A. Kivelson, “Vestigial nematicity from spin and/or charge order in the cuprates”, (2017), `arXiv:1701.02751`.